The role of magnetospheric plasma instabilities in auroral and substorm dynamics

Nadine Mathilde Esi Kalmoni

A thesis submitted to UCL for the degree of

Doctor of Philosophy

Mullard Space Science Laboratory

Department of Space and Climate Physics

University College London

March 24, 2017

I, Nadine Kalmoni, confirm that the work presented in this thesis is my own. Where information has been derived from other sources, I confirm that this has been indicated in the thesis.

_____

_____

For Grandma Thildy and Grandpa Tony,
and my little Elly

Abstract

The auroral substorm is the manifestation of explosive energy release from the rapid and global reconfiguration of the magnetotail. The auroral substorm is marked by a sudden brightening and poleward expansion of the most equatorward auroral arc in the midnight sector of the ionosphere. The temporal sequence of magnetospheric processes which lead to the dynamic auroral substorm display remain disputed to this day.

This thesis contains original research on the development and exploitation of novel data analysis techniques in order to analyse ground-based all sky imager data of the aurora, enabling the study of substorm processes in remarkable detail. Fourier analysis techniques are used to find the spatial scales of wave-like signatures (otherwise known as auroral beads/rays), which form along substorm onset arcs. Growth rates of ~ 0.05 s^{-1} are found from the exponential growth of the power spectral density of individual spatial scales. By analysing the dataset in this way, comparisons are made between observations and theoretical predictions of plasma instabilities at the near-Earth edge of the plasma-sheet which have been proposed to play a critical part in the substorm onset process.

Auroral arc tracking techniques are developed to automate and increase the size of the database of events analysed. The vast majority of independently identified substorm onsets are preceded by azimuthal structuring along the onset arc with median wavelengths of ~ 80 km. These beads grow and develop into a magnetospheric instability around 2 minutes prior to auroral substorm onset. Showing that beads are a common feature along the substorm onset arc provides unprecedented quantitative evidence that a near-Earth instability is a fundamental component of the substorm onset process.

Finally, analysis techniques are extended to state-of-the-art high resolution multi-spectral auroral data to investigate the processes driving auroral beads. Beads can be resolved in the green-, blue- and red-line aurora with spatial scales as small as 30 km, which later develop into larger structures of $\sim$ 80 km. These observations are consistent with Alfvén wave accelerated auroral particle precipitation and therefore imply that the substorm onset arc and auroral beads are driven unstable by waves.

Acknowledgements

The journey through my PhD can probably be described as both the best and the worst years of my life. The best for the excitement when you finally feel like you've uncovered an interesting result, that other people may want to hear about. The adrenaline when presenting your work at conferences to people you don't know, and when they seem as excited as you are, makes it all worthwhile. The worst because of the feeling of having taken on a vast, never-ending task. Without a doubt, the hardest part was not giving up!

There are many people I would like to thank, who have helped me throughout my PhD.

First and foremost I would like to thank my supervisor Jonny. When I first met with you to discuss your proposed PhD project, I knew I wanted you to be my supervisor, because I felt comfortable asking you questions without feeling stupid. Thank you for giving me so much of your time and effort, which is undoubtedly why its been such a productive 3.5 years. We have had many interesting discussions throughout my PhD, and I enjoyed most of them! Thank you for all your guidance and support, and for simplifying the problem when I haven't been able to see the aurora through the clouds. You have been a great teacher and mentor. Thank you for introducing me to so many other scientists, and encouraging me to travel around the world to meet them. I am very grateful to you for proposing such an interesting PhD project, I think we're onto something good!

I would also like to thank Clare and Marilia for being such incredible female role-models. Clare, your kindness, enthusiasm, encouragement and meticulous eye for detail is second-to-none. It has been such a pleasure to be able to work closely with you. Marilia, working with you and Robert at

Goddard was definitely one of the highlights of my PhD. Your passion, energy and enthusiasm was infectious, at a time where my own enthusiasm was waning (probably the end-of-PhD-blues). It was so lovely to get to know you and your beautiful family. Thank you for all of your support and encouragement!

A special thank you Kyle, who looked after me during both my trips to Goddard. Thank you for your guidance, for listening to my frustrations and offering solutions. Out of all the people I have worked with, I always felt like you knew exactly what I was talking about!

I would also like to thank the plasma group at MSSL, old and new, in particular Chris, Andrew, Colin and Rob for always asking really tough questions, and making sure I was prepared for any eventuality. A huge thank you to my office mates, including Georgie, Ali, Allan, Zhonghua, Louise and Licia (honorary office mate) who it has been great to have a good laugh with, drinking buckets of tea and coffee over the years and eating our way through never-ending supplies of cakes, biscuits and sweets. A special mention to Lloyd, for calmly and repeatedly explaining Fourier transforms in my moments of panic. And a very special thank you to Kirthika for keeping me sane, all our entirely-space-unrelated chats, taking me dancing, all your wise words and insights, and for generously allowing me to use your thesis template.

A very special thank you to Magnus, for your unwavering belief in me. Thank you for picking me up when I've been down, buying all those necessary tubs of Ben and Jerry's and joining me on some of my adventures which took us from strolling along the white chalk cliffs of the Isle of Wight to gallivanting among the bears of the green peaks of the Smoky Mountains. Thank you for listening to me when I've need someone to talk to, for taking me ceilidh dancing and climbing when I've needed a welcome distraction, and for keeping me sane throughout. Writing this thesis would've taken me a lot longer and been a lot more painful without your support.

Finally I would like to thank all my friends and family for their support, without which this PhD definitely wouldn't have been possible. Thank you all for putting up with my PhD-focussed mind, and lack of time.

In particular, I would like to thank my beautiful friends; Marina, for

the amazing summers at Goddard, our weekends exploring together, and our (occasional) afternoon breaks to chase pokemon; And Lois, for your energy and enthusiasm, for some amazing adventures and hopefully many more!

A very special thank you to Grandma Thildy, the most inspirational woman I know. You have supported me in every way possible, throughout my entire life. Talking to you always inspires me to right the wrongs of the world. And Grandpa Tony, you always encouraged me to further my academic studies and achieve my full potential. You bought me a maths textbook when I was about 15 years old. Without that book, I would've probably given up on maths! A big thanks to my brother Felix for being a good laugh. Thank you for taking me at face-value. You are one of very few people who has not continually asked '*How's the thesis going?*', and for that, I am incredibly grateful! And my cousin Joe, thank you for being there in my moments of crisis and being my Sunday roast buddy!

And of course Elly, thank you for your ability to always put a smile on my face, under any circumstance. I'm sad that I was never able to fully explain my thesis to you in detail, in the same way that I taught you GCSE history all those years ago, but I'm sure you caught some snippets along the way, and you probably don't mind!

And finally I would like to thank my parents; Mum for everything you have done and continue to do for me, your boundless encouragement and your words of wisdom and for helping me see when things are important, and more importantly, when things are not; And Ton, thank you for encouraging and enabling my obsession with space from a very young age. I remember you explaining that each star in the sky probably had some planets orbiting it, like in our very own solar system, and it made me feel a bit bewildered (which is probably why I have stuck a bit closer to home in my research). Thank you for frequently driving out of your way to pick me up and whisk me away from it all for a few days. And thank you for your sound advice on careers, cars and bikes, not to mention spotting that gas leak in my old flat!

Contents

List of Figures

List of Tables

Chapter 1

Background to Space Plasma Physics and the Earth's Magnetosphere

1.1 The Solar System

The vast majority ($\sim 99.9\%$) of the mass of the solar system is contained within the Sun. The Sun dominates the solar system, with all planets and small rocky bodies bound into orbit by its gravitational field. The Sun is predominantly composed of Hydrogen ($\sim 71\%$ by mass), Helium ($\sim 27\%$ by mass) and trace amounts of heavier elements of the periodic table (up to Iron). At its surface (photosphere) the Sun has an effective temperature of $\sim$5000 K. This temperature remains roughly constant through the lower atmosphere (chromosphere) but rises sharply through the transition region, reaching temperatures of up to 2×10^6 K in the outermost layer of the atmosphere, which is called the corona. Due to the exceedingly high temperature in all regions of the Sun, the elements of which it is composed are ionised. This ionised gas is known as plasma.

The outward thermal pressure of the corona exceeds the inward gravitational pressure of the Sun causing the coronal plasma to stream outwards, dragging the frozen-in coronal magnetic field with it (see Section 1.2.2.4). This combination of plasma and magnetic field is called the solar wind, and was first postulated by *Parker* [1958]. The solar wind is accelerated up to supersonic speeds and fills the entirety of interplanetary space. The region of

space dominated solar wind plasma is called the heliosphere, which extends into interplanetary space up until the point of pressure balance between the solar wind and the interstellar medium, which is called the heliopause.

The solar wind particles and magnetic field interact with solar system bodies to varying degrees. Objects which have an intrinsic magnetic field, such as the Earth, deflect the solar wind plasma around them, forming magnetospheres.

In this thesis we investigate the energy deposition between the solar wind and the Earth's magnetosphere, and the processes leading to the quasi-periodic explosive release of energy. To do this we first describe the basic properties and forces which act on charged particles in a plasma. These will subsequently allow us to understand how plasmas can become unstable on large and small scales, resulting in a global rearrangement of the magnetic field topology, depositing $\sim 10^{15}$ J of energy into the upper atmosphere in the form of auroral particle precipitation over approximately 5 hours [*Østgaard et al.*, 2002].

1.2 Basic Plasma Physics

In some ways a space plasma is very similar to an ordinary gas: it contains particles which are free to move. However an important difference is that some, if not all, of the constituents are electrically charged i.e., the ions and electrons are separated and move freely from one another. Individually charged particles feel forces from both electric and magnetic fields, whereas neutral particles do not. Plasmas can be understood by investigating the effects of electric and magnetic fields on individual particles. However if there many particles influenced by electric and magnetic fields, their motions can result in the modification of the fields. In this case, in order to describe the plasma accurately, the large scale plasma must considered as a whole: this is known as magnetohydrodynamics (MHD).

In this chapter we will first outline how individual charged particles react to electric and magnetic fields. Following this, we will consider the large scale properties of the plasma.

1.2.1 Electromagnetic Fields and Forces on Individual Charged Particles

Charged particles feel forces due to electric and magnetic fields.

Charged particles are accelerated along electric fields. A positively charged particle will move in the direction of the electric field, and a negatively charged particle will move in the opposite direction. The force on a charged particle due to an electric field is called the Coulomb force and is given by:

$$\mathbf{F} = q\mathbf{E} \tag{1.1}$$

where **F** is the force on the particle, q is the charge of the particle and **E** is the electric field. Charged particles themselves are the source of an electric field: for electrons the electric field points inward, and for protons it points outwards. This causes like charges to repel, and opposite charges to attract each other.

When moving, charged particles are also accelerated by magnetic fields. However in this case, unlike the Coulomb force, the acceleration acts perpendicular to both direction of motion particle motion and the magnetic field, hence no work is done. This causes the particle to gyrate around magnetic field lines and is known as the Lorentz force:

$$\mathbf{F} = q(\mathbf{v} \times \mathbf{B}) \tag{1.2}$$

where, **v** is the velocity of the particle and **B** is the magnetic field. The Lorentz force depends on the charge of the particle, hence resulting in the clockwise gyration of positive ions, and the anti-clockwise gyration of electrons. This can be written as:

$$qv_{\perp}B = m\frac{v_{\perp}^2}{r_L} (= m\omega v_{\perp}) \tag{1.3}$$

where $v_{\perp}$ is the velocity of the particle perpendicular to the background magnetic, m is the mass of the particle, r_L is the radius of circular motion and ω is

the angular frequency of the particle. This gives the particle gyro-frequency:

$$\omega = q\frac{B}{m} \tag{1.4}$$

and Larmor radius:

$$r_L = \frac{v_\perp}{\omega} = \frac{mv_\perp}{qB} \tag{1.5}$$

A particle traveling completely parallel to $\mathbf{B}$ will not feel the Lorentz force. In the case where the particle has a velocity component parallel and perpendicular to the magnetic field, the motion is along a helical path. The centre of gyration is called the guiding centre. Electrons and ions gyrate in the opposite direction.

The equation of motion of a charged particle in both a uniform electric and magnetic field is called the Lorentz equation, and is the sum of both the Coulomb and Lorentz forces.

$$m\frac{\partial \mathbf{v}}{\partial t} = q(\mathbf{E} + \mathbf{v} \times \mathbf{B}) \tag{1.6}$$

In the presence of uniform electric and magnetic fields the Lorentz equation shows that the charged particles drift. The guiding centre drift velocity, $\mathbf{v_{E\times B}}$ of a particle is given by:

$$\mathbf{v_{E\times B}} = \frac{\mathbf{E} \times \mathbf{B}}{B^2} \tag{1.7}$$

This is referred to as $\mathbf{E} \times \mathbf{B}$ drift and results in the drift of electrons and positive ions together, in the same direction.

Inhomogeneities in the magnetic field such as a magnetic gradient or curvature can also introduce drifts to particle motion.

A gradient in the magnetic field leads to a drift perpendicular to both the magnetic field and its gradient. The drift velocity $\mathbf{v}_\nabla$ due to a magnetic field gradient is given by:

$$\mathbf{v}_\nabla = \frac{mv_\perp^2}{2qB^3}(\mathbf{B} \times \nabla\mathbf{B}) \tag{1.8}$$

where m is the mass of the particle, q is the charge of the particle, B is the

magnetic field strength, $v_\perp$ is the particle velocity perpendicular to B, and ∇B is the gradient in the magnetic field. The magnetic gradient drift depends on q, and hence acts in opposite directions for electrons and positive ions.

When magnetic field lines are curved, particles which have a velocity component parallel to the field feel a centrifugal force. The drift velocity $\mathbf{v_R}$ due to the curvature of magnetic field lines is given by:

$$\mathbf{v_R} = \frac{mv_\parallel^2}{q}\frac{\mathbf{R_C} \times \mathbf{B}}{R_C^2 B^2} \tag{1.9}$$

where $v_\parallel$ is the particle velocity parallel to B and R_C is the local radius of curvature of the field line. The magnetic curvature drift is also dependent on q, resulting in a drift in opposite directions for electrons and positive ions.

1.2.2 Magnetohydrodynamics

Magnetohydrodynamics (MHD) describes the large-scale properties and behaviour of a plasma, without considering individual particle trajectories. The definition of a plasma is a quasi-neutral ionised gas which exhibits collective behaviour. MHD is applicable when considering a large number of particles over large spatial scales, larger than the ion gyroradius, and timescales, longer than an ion gyroperiod. In ideal MHD the plasma is treated as a single magnetised fluid which describes macroscopic parameters such as density, pressure and flow. There is no distinction between different particle species.

1.2.2.1 Quasi-neutrality, Debye Shielding and the Plasma Frequency

Before we cover the MHD description of plasmas, we will address the large-scale plasma properties which allow us to understand the time and length scales where an MHD description is valid.

A plasma is an quasi-neutral ionised gas; a collection electrons and ions (and neutrals) that exhibits collective behaviour. Quasi-neutrality means that on average the plasma is neutral, and hence contains approximately the same number of positive ions and negative electrons in any given region (exceeding a certain size). On small scales, charge concentrations may arise due to random

particle motion, which set up electric fields to 'neutralise' the plasma. When considering a single charged particle, the electric potential is given by the Coulomb potential, ϕ_C:

$$\phi_C = \frac{q}{4\pi\epsilon_0 r} \tag{1.10}$$

where ϵ_0 is the permittivity of free space, and r is the distance from the particle.

However in a plasma, this potential disturbs the surrounding charged plasma particles. Particles with the same charge are repelled away, whereas the opposite charge is attracted. This causes a 'shielding' effect of the test charge, reducing the effect of the Coulomb potential in the plasma. The overall electrostatic potential in the plasma is the sum of the unshielded Coulomb potential ϕ_C and the potential due to the particles which have been displaced as a result of the Coulomb potential. This results in the Debye potential, ϕ_D:

$$\phi_D = \frac{q}{4\pi\epsilon_0 r} e^{-\frac{r}{\lambda_D}} \tag{1.11}$$

where λ_D is the Debye length which is given by:

$$\lambda_D = \left(\frac{\epsilon_0 k_B T_e}{n q_e^2}\right)^{\frac{1}{2}} \tag{1.12}$$

where k_B is the Boltzmann constant, n is the number density of shielding particles, T_e is the electron temperature and q_e is the charge of an electron. The electron temperature and charge are considered as they have much higher mobility than ions due to their much lower mass. The Debye length, λ_D, is the distance over which the thermal particle energy and electrostatic potential energy in a plasma are balanced.

In order for a plasma to be considered to be quasi-neutral, the size of the system needs to be much larger than λ_D, so that collective shielding can occur.

The plasma parameter, N_D, is the number of electrons in the Debye sphere, and is a measure of how 'good' the plasma is. If there are not enough particles in the Debye sphere, collective behaviour and charge shielding is inhibited. If $N_D >> 1$ then the plasma is well (fully) ionised, which means that

the typical thermal energy of electrons exceeds the electrostatic potential between adjacent electrons and ions. For $N_D < 1$ the plasma is strongly coupled: the electron thermal energy is low, meaning that they are likely to recombine with ions.

$$N_D = \frac{4\pi}{3}\lambda_D^3 n_e \tag{1.13}$$

where n_e is the electron number density.

If an external force disturbs the quasineutrality of a plasma, the electrons start to move to restore charge neutrality. Due to their inertia, the electrons oscillate around their equilibrium position. The frequency of these oscillations is called the electron plasma frequency, ω_{pe}:

$$\omega_{pe} = \left(\frac{n_e e^2}{m_e \epsilon_0}\right)^{1/2} \tag{1.14}$$

where e is the electron charge, and m_e the electron mass.

If the time between electron-neutral collisions is less than the time for an electron to complete a full oscillation around their equilibrium position, then the electrons are forced into equilibrium with the neutrals, and the medium cannot behave as a plasma. Hence, in a plasma:

$$\omega_{col} \ll \omega_{pe} \tag{1.15}$$

where ω_{col} is the electron-neutral collision frequency.

Magnetohydrodynamics, and hence quasi-neutrality, is valid on spatial scales greater than the ion gyroradius and the Debye length, and on timescales longer than the ion gyroperiod. If these requirements hold, then the plasma can exhibit collective behaviour. This means that plasma particles can interact simultaneously via electromagnetic forces. The equations which govern the collective motion of plasma 'fluid elements' is discussed below.

1.2.2.2 Maxwell's Equations

Maxwell's equations describe how electric and magnetic fields and charges and currents are generated and influenced by each other. Hence Maxwell's

equations show how charged particles react to electric and magnetic fields, and how their motion can also generate currents and hence magnetic fields, and thus modify the behaviour of the plasma.

- **Gauss' law**: an electric charge generates an electric field

$$\nabla \cdot \mathbf{E} = \frac{\rho}{\epsilon_0} \tag{1.16}$$

  where ρ is the electric charge density. Equation 1.16 means that if there is an electric charge at any point, then the divergence of $\mathbf{E}$ at that point is non-zero: there will always be a net flux into, or out of a volume surrounding the charge. Gauss' Law describes that electric charge acts as a source (for positive charge) and sink (for negative charge) of electric fields.

- **Gauss' law for magnetism**: there are no magnetic monopoles in nature.

$$\nabla \cdot \mathbf{B} = 0 \tag{1.17}$$

  The divergence of a magnetic field is always zero through a volume: there is always the same amount of flux going out, and coming into, the volume.

- **Faraday's induction law**: a time varying magnetic field induces an electric field.

$$\nabla \times \mathbf{E} = -\frac{\partial \mathbf{B}}{\partial t} \tag{1.18}$$

  A time-varying magnetic field generates an electric field circulating around it, and a circulating electric field induces a time-varying magnetic field.

- **Ampère's law**: a current, or a time varying electric field, induces a magnetic field.

$$\nabla \times \mathbf{B} = \mu_0 \left(\mathbf{j} + \epsilon_0 \frac{\partial \mathbf{E}}{\partial t} \right) \tag{1.19}$$

  where $\mathbf{j}$ is the current density and ϵ_0 and μ_0 are the permittivity and permeability of free space. Ampère's law shows that a flowing electric current induces a magnetic field which circles the current. And that a

time-varying electric field gives rise to a magnetic field that circles the electric field, known as the displacement current.

In an ideal MHD plasma, these equations become:

$$\nabla \cdot \mathbf{B} = 0 \tag{1.20}$$

$$\nabla \cdot \mathbf{E} = 0 \tag{1.21}$$

$$\nabla \times \mathbf{B} = \mu_0 \mathbf{j} \tag{1.22}$$

$$\nabla \times \mathbf{E} = -\partial \mathbf{B}/\partial t \tag{1.23}$$

as the plasma is approximately neutral ($\rho \approx 0$) at scales greater than the ion gygrodius, and $|\partial \mathbf{E}/\partial t| << |\nabla \times \mathbf{B}|$ for slow changes and non-relativistic flows required in MHD.

1.2.2.3 Fluid Description of a Plasma

Instead of studying the motion of individual particles, the average properties of a plasma are governed by the basic conservation laws for mass, momentum and energy. For a neutral fluid, these equations are the equations of hydrodynamics. However in a plasma, where electric and magnetic fields and currents have important effects on charged particles, the equations of magnetohydrodynamics are used. These equations incorporate traditional mechanics, as well as electromagnetic properties of the fluid.

MHD is the combination of the equations of fluid dynamics and Maxwell's equations of electromagnetism.

The equations of magnetohydrodynamics are as follows:

- Continuity Equation

$$\frac{\partial \rho}{\partial t} + \nabla \cdot (\rho \mathbf{v}) = 0 \tag{1.24}$$

The particle number density is constant if there are no source or loss processes. This is true in many space plasmas, however is not a good approximation for the ionosphere.

- Equation of Motion

  Momentum is conserved:

$$\rho\left(\frac{\partial \mathbf{v}}{\partial t}+\mathbf{v}\cdot\nabla\mathbf{v}\right)=-\nabla P+\mathbf{j}\times\mathbf{B} \tag{1.25}$$

  where P is the thermal pressure. In this equation the Lorentz force ($\mathbf{j}\times\mathbf{B}$) is included.

- Equation of State

  The equation of state assumes that there is no change in the entropy the fluid within the system. This gives:

$$P\rho^{-\gamma}=\text{constant} \tag{1.26}$$

  where γ is a constant and in three-dimensional adiabatic cases $\gamma = 5/3$.

- Ohm's Law

  Generalised Ohm's Law states that

$$\mathbf{E}+\mathbf{v}\times\mathbf{B}=\underbrace{\frac{\mathbf{j}}{\sigma}}_{\text{resistivity}}+\underbrace{\frac{\mathbf{j}\times\mathbf{B}}{n_e}}_{\text{Hall term}}-\underbrace{\frac{\nabla\cdot\mathbf{P_e}}{n_e}}_{\text{electron pressure}}+\underbrace{\frac{m_e}{n_e e^2}\frac{\partial\mathbf{j}}{\partial t}}_{\text{current variation}} \tag{1.27}$$

  where σ is the plasma conductivity, m_e is the electron mass, n_e is the electron number density and $\mathbf{P_e}$ is the electron pressure.

1.2.2.4 The Magnetic Reynolds Number and Ideal Ohm's Law

In a space plasma, Ohm's Law can be simplified to:

$$\mathbf{j}=\sigma(\mathbf{E}+\mathbf{v}\times\mathbf{B}) \tag{1.28}$$

where conductivity $\sigma = 1/\eta$. This form of generalised Ohm's Law is valid in fully ionised plasmas where the collision frequency is extremely low.

By substituting this into Faraday's law to eliminate the electric field term

and applying Ampère's Law in the MHD limit gives the induction equation:

$$\frac{\partial \mathbf{B}}{\partial t} = \underbrace{\nabla \times (\mathbf{v} \times \mathbf{B})}_{\text{convection}} + \underbrace{\frac{1}{\mu_0 \sigma} \nabla^2 \mathbf{B}}_{\text{diffusion}} \tag{1.29}$$

where μ_0 is the permeability of free space. The first term on the right describes how the magnetic field is affected by convection and the second term describes the effect of magnetic field diffusion. In an MHD plasma, the plasma conductivity can be taken as near-inifinite. In this case the diffusion term becomes very small, and the convection term dominates. Hence, the magnetic field is frozen-into the plasma, or vice versa.

Hence, when considering a near-infinite conductivity we get ideal Ohm's Law:

$$\mathbf{E} + \mathbf{v} \times \mathbf{B} = 0 \tag{1.30}$$

which, as demonstrated using the induction equation above, is the frozen-in condition.

From Equation 1.29 we also define the magnetic Reynolds number, which is the ratio of the convection term over the diffusion term:

$$R_m = \frac{\text{convection}}{\text{diffusion}} \tag{1.31}$$

When considering L as the typical plasma length scale, this becomes:

$$R_m = \mu_0 \sigma L v \tag{1.32}$$

If $R_m \gg 1$ magnetic field convection dominates and the field is frozen into the plasma, thus MHD is an appropriate assumption. The diffusion term in the induction equation can be neglected under these conditions. However, when $R_m \approx 1$ diffusion cannot be neglected. In a diffusion dominated region the plasma can move across a magnetic field, and have very little effect on it. The quantities which are most likely to affect the magnetic Reynolds number, and hence the frozen in approximation are the plasma conductivity and length scales.

1.2.2.5 Magnetic Tension and Magnetic Pressure

As a result of ideal MHD, the concepts of magnetic tension and pressure can be introduced. From Ampère's law in the MHD limit:

$$\nabla \times \mathbf{B} = \mu_0 \mathbf{j} \tag{1.33}$$

Using this we can understand the magnetic force $\mathbf{j} \times \mathbf{B}$ by substituting in Ampère's law for $\mathbf{j}$:

$$\mathbf{j} \times \mathbf{B} = \frac{1}{\mu_0}(\nabla \times \mathbf{B}) \times \mathbf{B} = -\nabla \frac{B^2}{2\mu_0} + \frac{1}{\mu_0}(\mathbf{B} \cdot \nabla)\mathbf{B} \tag{1.34}$$

The first term $B^2/2\mu_0$ is the force due to a gradient in magnetic flux density, and is dimensionally a pressure, and is known as the magnetic pressure.

The plasma beta is defined as the ratio of plasma pressure, nk_BT, to magnetic pressure, $B^2/2\mu_0$:

$$\beta = \frac{2\mu_0 n k_B T}{B^2} \tag{1.35}$$

When $\beta > 1$ the plasma pressure dominates over the magnetic pressure, whereas if $\beta < 1$ the magnetic field pressure dominates.

The second term reduces to $(\hat{\mathbf{n}}B^2/\mu_0)/R_c$ (after *Kivelson and Russell*, 1995, p. 50) and gives the magnetic tension force, where R_c is the radius of curvature and $\hat{\mathbf{n}}$ is the outward normal to the magnetic field. The magnetic tension force, otherwise known as the curvature force, acts antiparallel to the radius of curvature of field lines, and is analogous to the perpendicular force exerted by tension in a curved string.

1.2.3 MHD Waves

MHD waves are the solutions of the MHD equations for continuity, state, momentum conservation and Maxwell's equations. These can be solved for both a cold plasma, where the particle thermal pressure can be assumed to be zero, and for a warm plasma. In this section we derive the MHD waves for a warm plasma only.

To derive the MHD wave equations, we assume stationary plasma (initially at rest), which means that there are no flows and electric fields. A perturbation to the system will introduce perturbations to the following parameters:

$$\mathbf{B} \rightarrow \quad \mathbf{B_0} + \mathbf{B_1} \tag{1.36}$$

$$\rho \rightarrow \quad \rho_0 + \rho_1 \tag{1.37}$$

$$P \rightarrow \quad P_0 + P_1 \tag{1.38}$$

and introduce small fluctuations in the electric field, plasma velocity and current density such that:

$$\mathbf{E} \rightarrow \quad \mathbf{E_1} \tag{1.39}$$

$$\mathbf{v} \rightarrow \quad \mathbf{v_1} \tag{1.40}$$

$$\mathbf{j} \rightarrow \quad \mathbf{j_1} \tag{1.41}$$

Using a linear wave approximation we assume that perturbations to the system are small enough so that only linear terms in the equations need to be retained. By substituting these linear approximations into Maxwell's equations, assuming that B_0 is uniform and stationary (no spatial or temporal gradients) and P_0 cannot be neglected (as this is the warm plasma case) the warm plasma dispersion relation can be derived as (after *Kivelson and Russell*, 1995, p. 340):

$$(\omega^2 - cos^2\theta k^2 v_A^2)[\omega^4 - \omega^2 k^2 (c_s^2 + v_A^2) + cos^2\theta k^4 v_A^2 c_s^2] = 0 \tag{1.42}$$

where θ is the angle between the wave vector, k and the background magnetic field B_0, ω is the angular frequency ($\omega = 2\pi f$), v_A is the Alfvén velocity ($v_A = \sqrt{B^2/\mu_0\rho}$) and c_s is the speed of sound.

The warm plasma dispersion relation has three solutions: the Alfvén mode (Equation 1.43), the slow mode and the fast mode (given by the two roots of Equation 1.44):

$$\omega^2/k^2 = v_A^2 cos^2\theta \tag{1.43}$$

$$\omega^2/k^2 = \frac{1}{2}\left[c_s^2 + v_A^2 \pm \sqrt{(c_s^2 + v_A^2)^2 - 4c_s^2 v_A^2 cos^2\theta}\right] \tag{1.44}$$

The shear Alfvén wave (Equation 1.43) is a purely transverse wave which does not compress the plasma. This means that wave propagation is parallel to the background magnetic field, at the Alfvén speed. The velocity vector is perpendicular to the wave vector. The Alfvén wave does not cause perturbations to the background plasma density or pressure.

The fast and slow waves are magnetosonic waves (two roots of Equation 1.44), which are analogous to an ordinary sound wave. The fast and slow mode waves are compressional, and therefore cause the plasma density, pressure and the magnitude of the magnetic field to fluctuate. These waves can be polarised so that they have a both transverse and longitudinal propagation component.

For the fast mode wave, the perturbations to plasma pressure and magnetic pressure are in phase, whereas for the slow mode wave they are out of phase. As the name suggests, the fast mode has a higher phase speed than the slow mode.

1.2.4 Magnetic Reconnection

Figure 1.1 shows a schematic for magnetic reconnection. Under ideal MHD plasmas originating from different sources with their own particle populations cannot mix. However when the assumptions of ideal MHD break down at small spatial scales and when diffusion dominates over convection, i.e., $R_m \ll 1$ an ion diffusion region can form (indicated by light blue box in Figure 1.1). When there is a sharp gradient in magnetic field topology, such as an antiparallel magnetic field lines, a thin current sheet forms in-between two plasma populations, as given by Ampère's law.

The magnetic Reynolds number shows that at small spatial scales the frozen-in principle breaks down and plasma is able to move separately from the field. These spatial scales are comparable or smaller than the ion gyroradius. This allows plasmas from different populations on either side of a thin

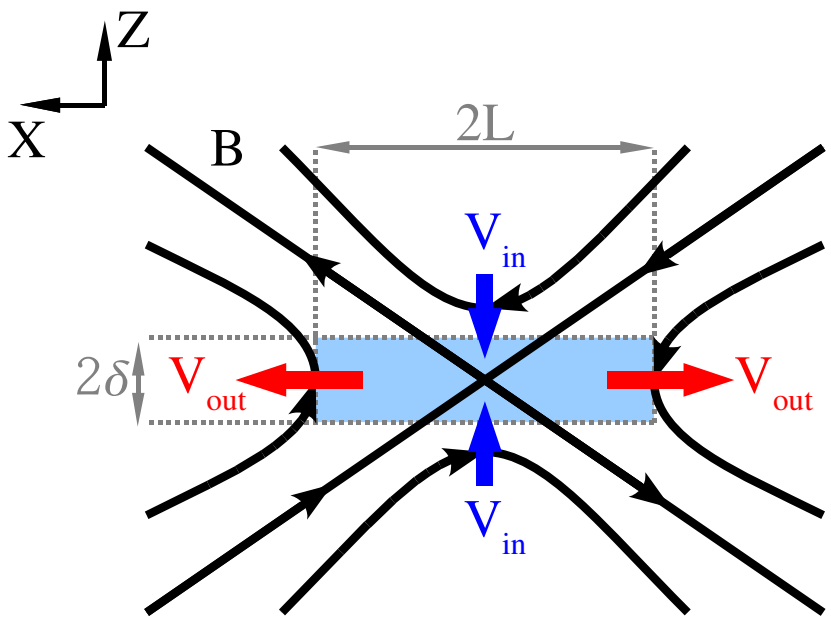

Figure 1.1: Schematic for Sweet-Parker reconnection. Plasma inflow from the top and bottom, V_{in} pushes magnetic fields together. On small scales and at sharp magnetic gradients, an ion diffusion region forms (light blue box). Here the magnetic field becomes very low, and particles are able to move independently from the magnetic field. This causes the original magnetic field lines to break apart, and reconnect in a different orientation. The newly reconnected field lines are expelled from the diffusion region with velocity V_{out}. Figure taken from *Walsh* [2009].

current sheet to mix. Outside the diffusion region, the frozen-in condition still holds. An inward flow (V_{in}) pushes the oppositely aligned magnetic fields together, and the particles are no longer frozen onto the magnetic fields and the fields can diffuse through the plasma. Inside the diffusion region, the original magnetic field vanishes and the magnetic neutral point, where the magnetic field strength tends to zero, is formed. This allows the old field lines to break and reconnect forming new, highly bent field lines. Magnetic tension forces straightens out the field lines, causing them to be expelled away (V_{out}) from the neutral point, transferring magnetic energy to the plasma particles, accelerating the particles which become frozen back onto the field lines outside the diffusion region along the field lines. This is the cause of high speed plasma exhausts which travel in both regions away from the reconnection site at, or near, the Alfvén velocity. Magnetic reconnection therefore allows separate plasma populations to mix when they otherwise would not.

1.3 The Earth's Magnetosphere

The Earth's intrinsic magnetic field, which is well represented by a magnetic dipole to a first order approximation, excludes external magnetic fields such as the interplanetary magnetic field (IMF). A static magnetosphere forms due to the pressure balance between the solar wind particle pressure, and the internal magnetic and particle pressure. The separation between the solar wind and magnetospheric plasma populations confines the Earth's intrinsic field to a region called the magnetosphere. The dipole shape becomes distorted due to solar wind pressure causing compression on the sunward side and frictional interaction between the solar wind and the boundary layer stretches the field into a tail on the night side. The region of space where the Earth's own magnetic field dominates is referred to as the magnetosphere. The magnetosphere separates the Earth's plasma population from the solar wind plasma. In a closed configuration, the magnetosphere is impermeable to solar wind plasma due to the magnetic field frozen in condition. Figure 1.2 shows a schematic of the closed magnetosphere configuration.

1.3.1 The Bow Shock and Magnetosheath

The solar wind propagates at highly supersonic radial velocities. When it encounters the stationary magnetosphere, which is an impenetrable object, the solar wind has to slow down. The supersonic nature of the solar wind, means that it travels faster than any pressure wave which could divert the flow around the magnetosphere. This causes the formation of a bow shock, a fast magnetosonic shock front, upstream of the magnetosphere where the particles are slowed down and heated.

Behind the bow shock, is the magnetosheath. The magnetosheath is the region of turbulent, subsonic, dense, hot plasma, with a higher magnetic field than in the solar wind. The subsonic nature of the magnetosheath plasma allows it to be diverted around the magnetosphere. The locations of the bow shock and magnetosheath relative to the magnetosphere are shown in Figure 1.2.

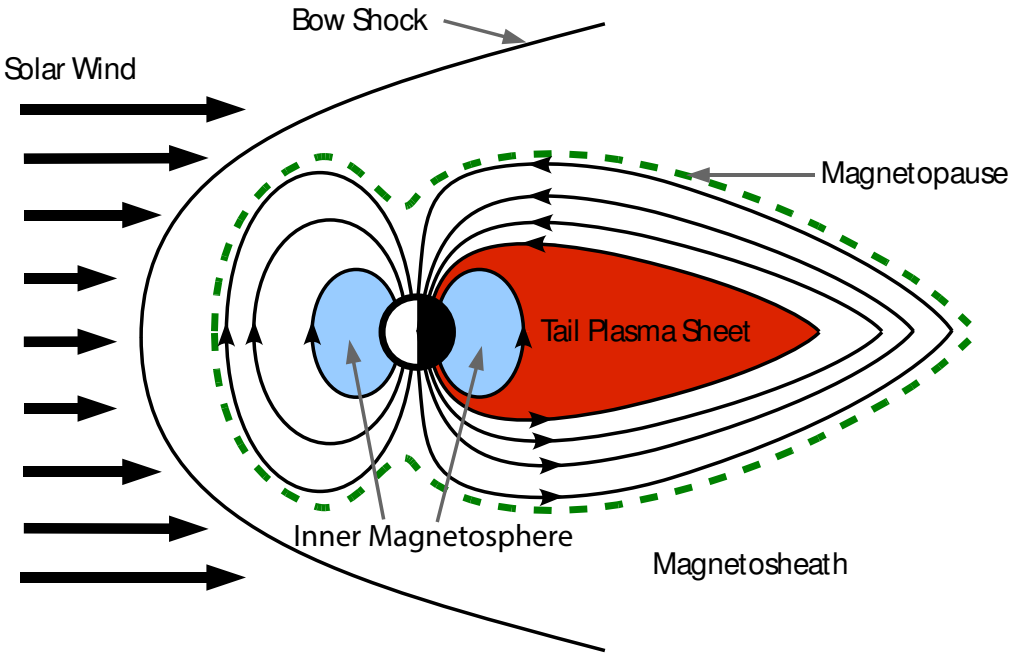

Figure 1.2: Cross-section in the noon-midnight meridian, of the Earth's magnetosphere formed due to the compression of the dipole field on the dayside, and the stretching of the tail on the nightside. Some of the separate plasma populations and boundaries are indicated. Figure taken from *Walsh* [2009] (not to scale).

1.3.2 The Magnetopause

Due to the frozen-in condition holding across the vast majority of the magnetosphere, the magnetosheath (solar wind plasma) and magnetospheric plasma populations do not mix. This means that there is a discontinuity, or gradient, between the magnetic fields frozen into these separate populations. Ampère's Law states that a thin current sheet arises due to gradient in magnetic field. In this case, a current sheet is formed in between the magnetosheath and magnetospheric plasma populations. This current is called the magnetopause, and is otherwise known as the Chapman-Ferraro current [*Chapman and Ferraro*, 1931], and is shown by the green-dashed line in Figure 1.2. The direction of the magnetopause currents on the dayside magnetosphere and the flanks are shown in Figure 1.3.

1.3.3 The Magnetotail

In a closed magnetosphere model, the solar wind compresses the dayside magnetosphere due to the solar wind pressure, and stretches the nightside magnetosphere due to viscous interactions. This effect is enhanced by dayside magnetic reconnection opening up the magnetosphere to solar wind plasma, as will be described in Section 1.4.1. The magnetotail acts as a reservoir of plasma and the storage of energy. At the centre of the magnetosphere is a region of hot, dense plasma, with a low magnetic field strength called the plasma sheet. The plasma sheet is magnetically conjugate to the nightside auroral oval in the ionosphere. On either side of the plasma sheet are the tail lobes. These are regions of open magnetic field which are tied into the Northern and Southern polar cap. The lobes have a higher magnetic field strength than the plasma sheet, but are made up of cold, sparse plasma.

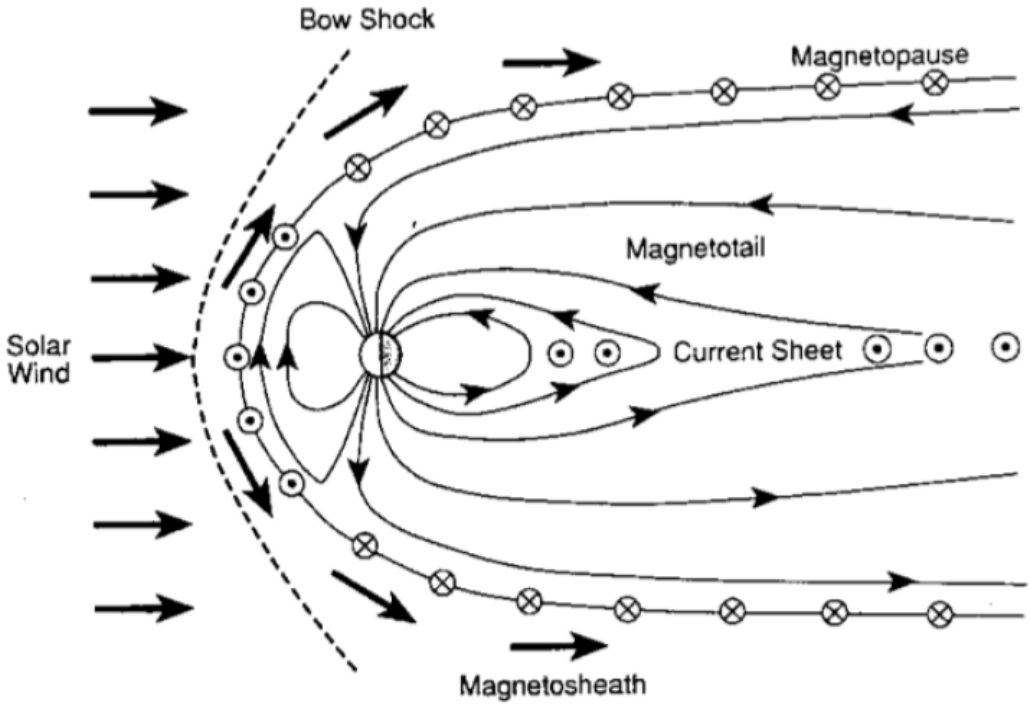

Figure 1.3: Cross-section of the magnetosphere in the noon-midnight meridian, with the Chapman-Ferraro magnetopause currents and the cross-tail current indicated. Figure taken from *Kivelson and Russell* [1995].

The gradient, or change in magnetic field direction in the magnetotail

induces another current sheet: the cross-tail current. The cross-tail current is located at the centre of the plasma sheet and closes through the magnetopause currents in the flanks of the tail. Figure 1.3 shows a schematic of the cross-tail current in the plasma sheet. The cross-tail current closes through the Chapman-Ferraro magnetopause current described in Section 1.3.2.

1.3.4 The Inner Magnetosphere

The inner magnetosphere is typically the name given to the region of the magnetosphere within geosynchronous orbit, $6.6\mathrm{R}_E$, where R_E is an Earth radius, $6,371$ km.

The plasmasphere extends closest to Earth and consists of dense, cold plasma of ionospheric origin and co-rotates with the Earth. The plasmasphere terminates at a radial distance of $3-5\mathrm{R}_E$ and its edge is called the plasmapause. The plasmasphere primarily consists of Hydrogen ions, as well as Helium, Oxygen and Nitrogen ions as a result of ionospheric ion outflow.

The Van Allen radiation belts spatially overlap with the plasmasphere, and extend out to $\sim 6\mathrm{R}_E$. The radiation belts consist of electrons and ions which are trapped on dipolar magnetic field lines and bounce between the Northern and Southern hemispheres. The radiation belts are split into two belts which are located at $\sim 0.1-1.5\mathrm{R}_E$ and $\sim 3-6\mathrm{R}_E$. The inner radiation belt consists mostly of a stable population of protons with typical energies of $\sim 3-300$ keV, however some protons have energies up to 1 MeV [*Fennell et al.*, 2015], and lower energy $<$ 600 keV electrons [*Li et al.*, 2015]. The outer radiation belt is highly dynamic and is dominated by electrons injected by substorm injections which are accelerated up to relativistic energies of $1-10$ MeV.

The particles in the radiation belts also drift azimuthally due to magnetic field gradient and curvature drift as described in Section 1.2.1. These drifts are energy-dependent, and hence the oppositely directed magnetic drifts dominate at energies $>$ few keV, causing electrons to drift eastward and ions to drift westward. The opposite drift directions generates the ring current. The bulk (90%) of the ring current is contained by ions of $15-250$ keV [*Williams*, 1980].

1.3.5 The Ionosphere and Aurora

The ionosphere is a collisional plasma at the top of the atmosphere and at the base of the magnetosphere. The particles in the atmosphere are neutral, whereas the plasma in the magnetosphere is considered to be fully ionised. The ionosphere is the transition region between these neutral and ionised particle populations, and hence is partially ionised. The ionosphere is formed by the ionisation of neutral particles due to solar UV radiation (photoionisation) and energetic magnetospheric particle precipitation (particle-impact ionisation), which dominates at high magnetic latitudes in the auroral zones. The ionosphere is a mixture between ionised and neutral gas up to ~ 500 km altitude. At around 110 km there is a peak in electron density due to electron precipitation [*Baumjohann and Treumann*, 1996].

At high latitudes magnetic field lines in the night-side ionosphere map to the central plasma sheet in the magnetotail. Precipitating energetic electrons originating in the plasma sheet collide with particles in the ionosphere to create the aurora. The brightest and most dynamic aurora are located within the auroral oval at $\sim 60 - 71^o$ geomagnetic latitude [*Frey et al.*, 2004]. Within the auroral oval, the aurora is organised into thin concentric bands called auroral arcs [*Davis*, 1978]. The magnetospheric processes which generate auroral arcs are currently not well understood.

Electrons with higher energies are able to travel further along magnetic field lines and penetrate to lower altitudes in the ionosphere. Hence, variations in ionospheric density and composition at different altitudes means that electrons precipitating with different energies result in the different types of auroral emissions. Figure 1.4 shows computation results of the altitude profiles of electrons with different energies in a model atmosphere [*Rees*, 1963]. For example, the primary auroral electrons have energies of $1 - 10$ keV, allowing them to penetrate to altitudes of $100 - 150$ km. Lower energy electrons $\sim 0.4 - 0.5$ keV can penetrate to ~ 200 km, below which the red-line aurora is quenched, showing that these low energy electrons are primarily responsible for the red-line aurora.

The prominent auroral emissions are the green-, red- and blue-line au-

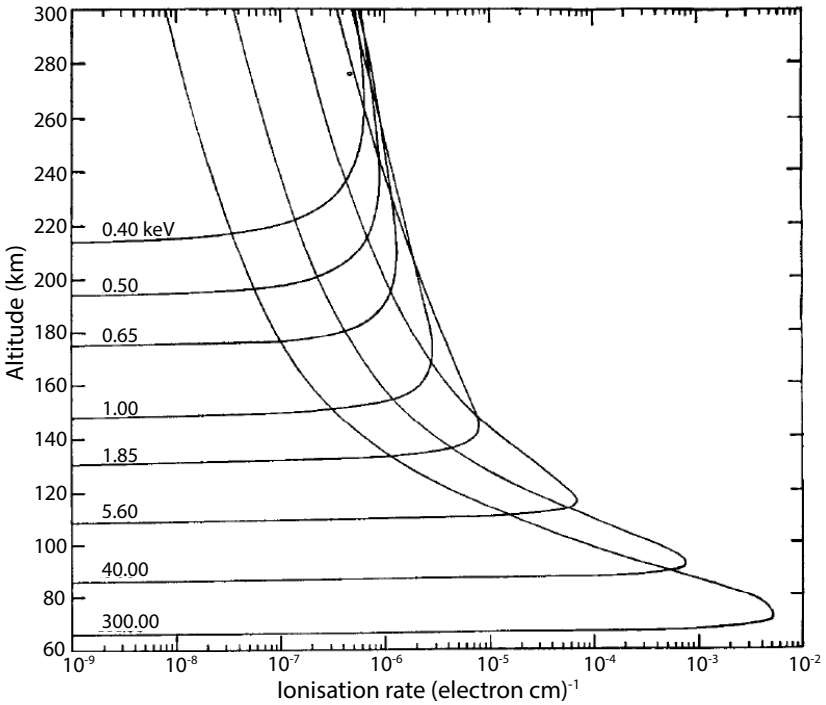

Figure 1.4: Ionisation rate per unit volume per unit of incident electron flux as a function of altitude in the ionosphere caused by precipitating mono-energetic electrons with energies of $0.4 - 300$ keV. Figure taken from *Rees* [1963].

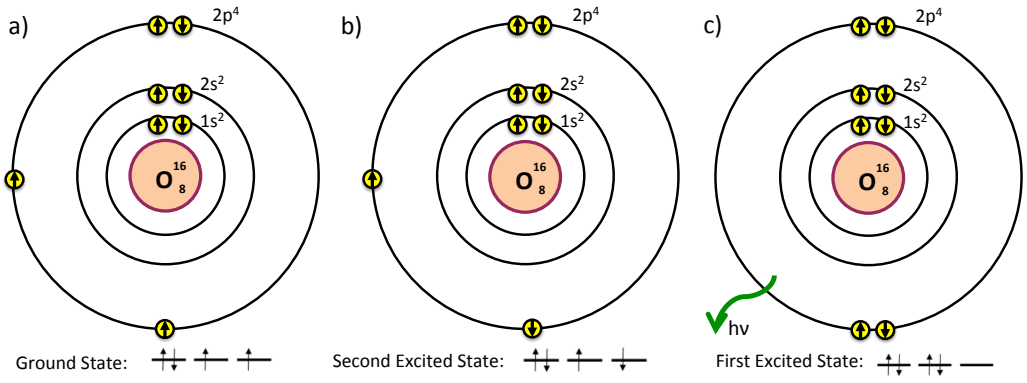

Figure 1.5: The electron transitions leading to the emission of a photon (wavelength 557.7 nm) responsible for the green aurora. a) the ground state of atomic Oxygen (^{3}P). b) The collision of an electron with energy > 10 keV excited the Oxygen atom into the second excited state (^{1}S). c) The Oxygen drops down into the first excited state (^{1}D) after ~ 0.7 seconds and emits a green photon.

rora. Figure 1.5 shows the Oxygen atom electron transitions that produce the green-line auroral emission. When an energetic electrons ($>$ 10 keV) collide with atomic Oxygen, the Oxygen is excited to the second excited state (^{1}S). When the electrons in the atom drop down to the first excited state (^{1}D), a photon with energy corresponding to a green-wavelength photon (557.7 nm) is released. As described above, the green-line aurora is generated due to the emission of a 557.7 nm wavelength photon by atomic Oxygen. The emission lifetime for this green photon is $\sim$ 0.7 seconds, and is typically observed at 110 km altitude. Typical electron precipitation energies of $>$ 10 keV are required for this emission [*Rees*, 1963].

Red-line aurora is caused by a 630.0 nm photons emitted by atomic Oxygen. The emission lifetime for this photon is $\sim$ 110 seconds, and is typically observed around $\sim$ 200 km altitude. The red-line aurora is caused by low energy electron precipitation with typical energies of $<$ 1 keV [*Rees*, 1963]. Both the green- and red-line aurora are caused by forbidden Oxygen atom electron transitions, which are defined by the selection rules between quantum states. In this case, the quantum selection rules for electric and magnetic dipole transitions are not met, resulting in a low emission rate. These forbidden transitions are still possible at altitudes above $\sim$ 100 km as the density, and hence collision frequency, of the excited atoms is low.

Finally, the blue-line auroral emission at 427.8 nm is much fainter than the red- and green-line. This is a prompt emission of $\sim 10^{-7}$ seconds from molecular Nitrogen and is typically observed around 90 km altitude. The intensity of the blue-line emission has been shown to be proportional to the total incident energy flux from precipitating electrons, and hence is not reliant on a single population [*Dalgarno et al.*, 1965].

Rees and Luckey [1974] showed that ratios between the different auroral emission lines, together with the absolute emission of 427.8 nm can provide a good estimate of the characteristic energy of the precipitating electrons.

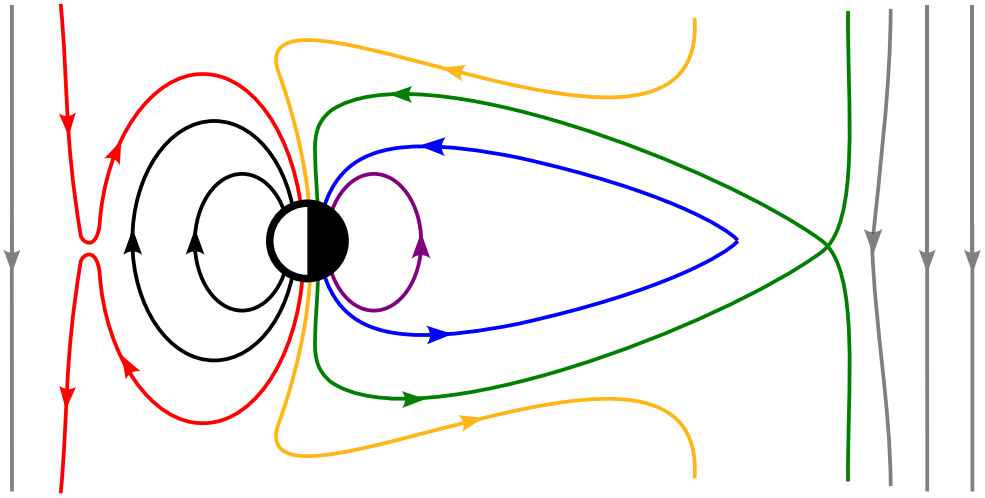

Figure 1.6: A schematic of the magnetic field line reconfiguration during the Dungey cycle. Reconnection on the dayside magnetopause opens up magnetic field lines (red) to solar wind magnetic field (grey). They are dragged anti-sunward into the magnetotail where they become part of the lobes (yellow). Another reconnection site at the distant neutral line in the tail closes the open flux (green) and allows dipolarisation of the stretched field (purple). The field convects back round to the dayside (black) to complete the cycle. Figure adapted from *Walsh* [2009] (not to scale).

1.4 Magnetospheric Dynamics

1.4.1 The Dungey Cycle

The "*Dungey cycle*" was postulated by *Dungey* [1961] and describes the coupling between the magnetosphere and the solar wind during southward IMF. A schematic of the magnetic field line configuration and motion described by the Dungey cycle is shown in Figure 1.6. During southward IMF, the magnetic field carried by the solar wind (grey) and the Earth's dipole field are anti-aligned at the dayside magnetopause. Magnetic reconnection at this location opens up the magnetosphere allowing solar wind plasma to enter the Earth's magnetosphere. The newly opened magnetic field lines (red) are tied to the magnetic poles at one end, and are connected to the solar-wind at the other end. Through magnetic tension and solar wind flow, the field lines are pulled anti-sunward over the northern and southern poles, into the magnetotail. Here they become part of the magnetotail lobes (yellow) The addition of newly opened field lines into the lobes increases the magnetic pressure,

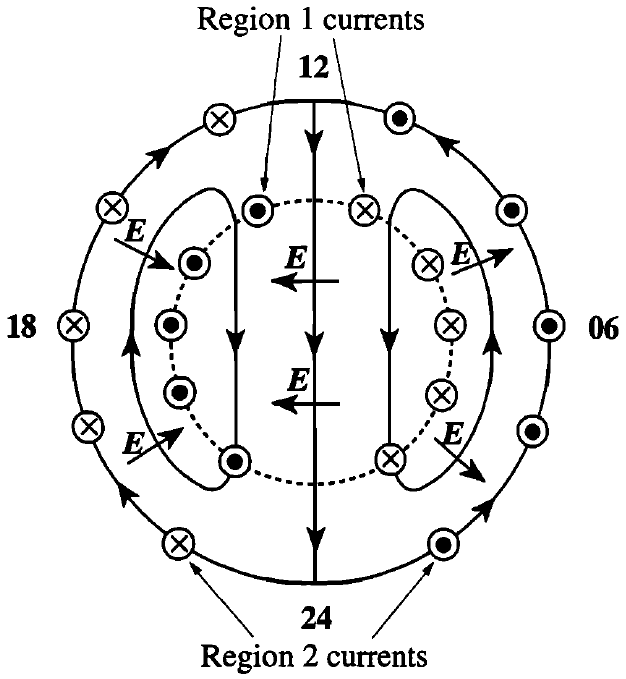

Figure 1.7: Ionospheric two-cell convection pattern due to the Dungey cycle mapped into the ionosphere. The arrowed solid lines are the plasma streamlines, the short arrows show the direction of the electric field. The Hall current flows opposite to the plasma streamlines. The upward and downward field aligned currents associated with the Region 1 and Region 2 current system are also indicated. Figure taken from *Cowley* [2000].

and pushes the oppositely aligned field lines together, forming a reconnection point in the tail (green). The reconnected magnetic field line then relaxes and moves Earthward due to the magnetic tension force and convection carrying the plasma tied to the field line with it (purple). These magnetic field lines then convect round the Earth and back to the dayside where the cycle repeats itself (black).

The motion of the magnetic field lines over the poles at high latitudes and back round to the dayside at low latitude produces a two-cell plasma convection pattern in the ionosphere, shown in Figure 1.7. The plasma tied to the magnetic field lines follows the same pattern. An electric field arises due to the plasma drift from $\mathbf{E} = -\mathbf{v} \times \mathbf{B}$, resulting in a duskward electric field over the polar cap, and a dawnward electric field at lower latitudes where the ionospheric plasma returns to the dayside. At high altitudes (> 125 km) both electrons and ions drift in the same direction under $\mathbf{E} \times \mathbf{B}$ drift, however ions move slower than electrons due to collisions in the ionosphere. This causes

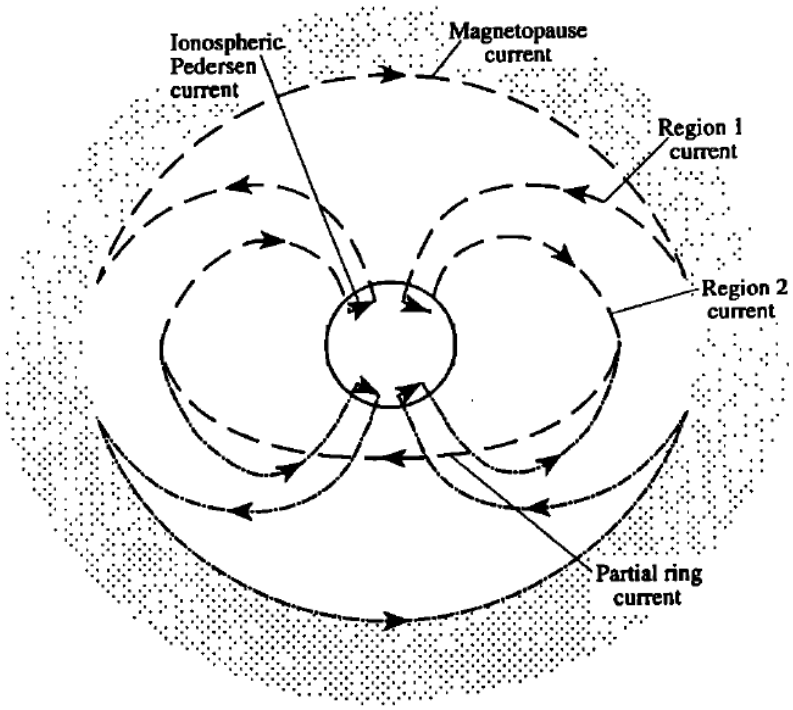

Figure 1.8: Schematic of the magnetosphere-ionosphere coupling between the ionospheric Region 1 and Region 2 current systems, and the magnetopause and ring current. The northern hemisphere (dashed) and southern hemisphere (solid) current circuits are shown as observed from the tail. Figure taken from *Cowley* [2000].

a Hall current, which consists of the eastward current (electrojet) in the pre-midnight sector, and the westward current (electrojet) in the post-midnight sector.

At lower altitudes (< 125 km) the Pedersen currents, which flow in the same direction as the convection electric field, dominate the ionospheric current system. The Pedersen currents connect the high latitude (Region 1) and lower latitude (Region 2) field aligned current regions which are marked in Figure 1.7. The Region 1 and Region 2 currents are magnetosphere-ionosphere coupling currents, connecting the ionosphere with different regions of the magnetosphere. The low latitude Region 2 currents couple to the ring current. On the nightside the high latitude Region 1 currents couple to the near-Earth plasma sheet, whereas on the dayside they connect to the magnetopause. The coupling between these different regions of the magnetosphere by field aligned currents is shown in Figure 1.8.

1.4.2 Substorms

In the Dungey cycle [*Dungey*, 1961] the rates of reconnection at the dayside and nightside are assumed to be balanced and hence the magnetosphere is in a 'steady-state'. However this is not often the case. During Southward IMF the rate of reconnection on the dayside exceeds the rate of reconnection on the night side. This allows magnetic flux to build up and be stored in the magnetotail lobes [*Axford*, 1969], and is called the substorm growth phase [*McPherron*, 1970].

At some subsequent point, the magnetic flux in the lobes builds up sufficiently to trigger explosive reconnection at the Near-Earth Neutral Line (NENL), around $20 - 25\mathrm{R}_E$ [*Hones*, 1976]. At this stage, the rate of reconnection at the NENL generally exceeds reconnection on the dayside. The explosive release of energy stored in the magnetotail is called the substorm expansion phase [*Akasofu*, 1964]. The substorm expansion phase is typically associated with the dynamic substorm aurora, and the dipolarisation of the stretched tail magnetic field. During a substorm energetic particles are injected from the tail into the inner magnetosphere and contribute towards the radiation belts population and the ring current. Reconnection in the tail causes the expulsion of a plasmoid, a closed bundle of magnetic flux not tied to the Earth or the solar wind. During the substorm expansion phase there is also a reduction of the cross-tail current at the near-Earth edge of the plasma sheet, $\sim 9 - 10\mathrm{R}_E$ [*McPherron et al.*, 1973]. The current is diverted along magnetic field lines in the post-midnight sector, through the auroral ionosphere in the westward direction, forming an additional contribution to the westward electrojet, and back out into the plasma sheet in the pre-midnight sector. This substorm current system is known as the Substorm Current Wedge (SCW), shown in Figure 1.9.

Within substorm research, the exact sequence of events regarding the onset of reconnection in the magnetotail, the diversion of the cross-tail current, and auroral breakup are hotly debated (e.g., *Angelopoulos*, 2008; *Lui*, 2009; *Angelopoulos et al.*, 2009). Substorms are very difficult to predict, as the physical processes which lead to substorm onset are currently not well understood.

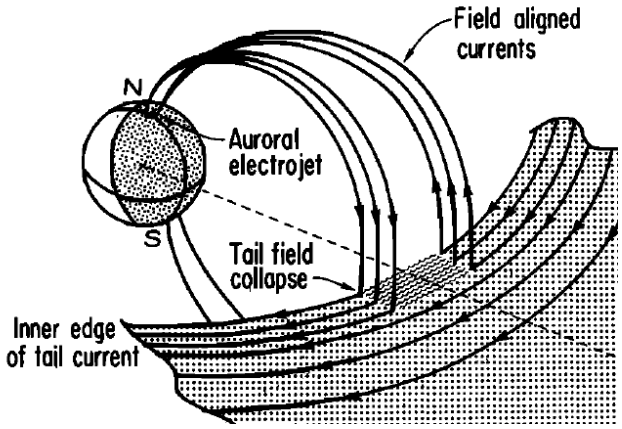

Figure 1.9: The diversion of the cross-tail current along magnetic field lines and into the post-midnight ionosphere. The current flows through the ionosphere and back out along magnetic field lines in the pre-midnight sector into the central current sheet. The ionospheric component of the substorm current wedge constitutes the auroral electrojet. Figure taken from *McPherron et al.* [1973].

1.4.3 Magnetosphere-Ionosphere Coupling

It is possible to improve understanding of the intricacies of the magnetosphere by studying its conjugate ionospheric processes such as the aurora. The key element in coupling the magnetosphere with the ionosphere are the field-aligned currents which flow between these separate regions, such as those shown in Figures 1.7-1.9.

A schematic of a scenario resulting in magnetosphere-ionosphere coupling is shown in Figure 1.10. Currents in the magnetosphere are caused due to the relative drift of ions and electrons. However inhomogeneities such as plasma boundaries can lead to currents not being divergence free: e.g., violating Gauss' law. For example, this can be due to irregularities in the plasma sheet. Sunward convection of plasma sheet particles, means that there is a significantly higher current in the westward direction at the edge of this region, than there is outside, as is shown in Figure 1.10. This current is not equal across the boundary as there are simply not enough particles to support it outside the plasma sheet, which means that field-aligned currents (FACs) are necessary to close the the extra current through the ionosphere. The ionospheric signatures produced by FACs can allow us to study the magnetospheric processes which lead to magnetosphere-ionosphere (M-I) coupling in

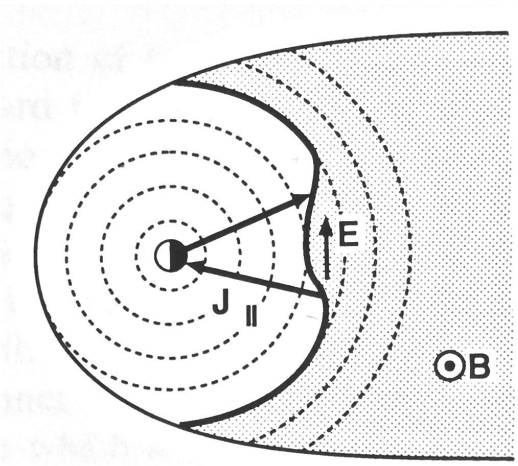

Figure 1.10: Field-aligned currents and electric fields due to a 'bump' in the plasma sheet, resulting in extra current in this region. The extra current is closed through through currents in the ionosphere. The dotted curves are lines of constant equatorial magnetic field. Gradient-curvature current flows westward along these curves. Figure taken from *Kivelson and Russell* [1995].

higher detail from the ground, than possible from single-point measurements in space.

In this thesis, we use auroral data to quantify small-scale structures in the aurora in order to understand their magnetospheric counterpart. This allows us to investigate the disturbance in the near-Earth plasma sheet during the substorm expansion phase and inform us about the physical processes leading to the substorm expansion phase onset

Chapter 2

The Auroral and Magnetospheric Substorm

2.1 A Global Picture of the Auroral Substorm

The idea of the auroral counterpart of the magnetospheric substorm was first mentioned by *Akasofu* [1964]. Akasofu's auroral substorm was the culmination of auroral observations from all-sky imagers across Siberia, Alaska and Canada. Even though no two auroral displays are alike, Akasofu recognised several common features. The identification of these common features lead to the discovery and definition of two (of the three now known) substorm phases, the expansive phase and the recovery phase. Figure 2.1 shows Akasofu's schematic diagram of the common features of global auroral substorm, and the main features of the expansive and recovery phases.

The auroral morphology before substorm onset, the '*quiet phase*', is one with quiet homogenous auroral arcs in the midnight sector of the auroral oval, closely aligned with geomagnetic latitude. In the polar cap, at higher geomagnetic latitudes, auroral arcs lie along the Sun-Earth line [*Davis*, 1962]. This is shown in Figure 2.1*A*.

As the name suggests, in the expansive phase a quiet auroral arc, often the most equatorward arc, rapidly brightens (Figure 2.1*B*) [*Akasofu*, 1977], breaks up and expands poleward (Figure 2.1*C*, *D*). The first signature of a substorm is '*a sudden increase in the brightness of the part of a quiet arc*'

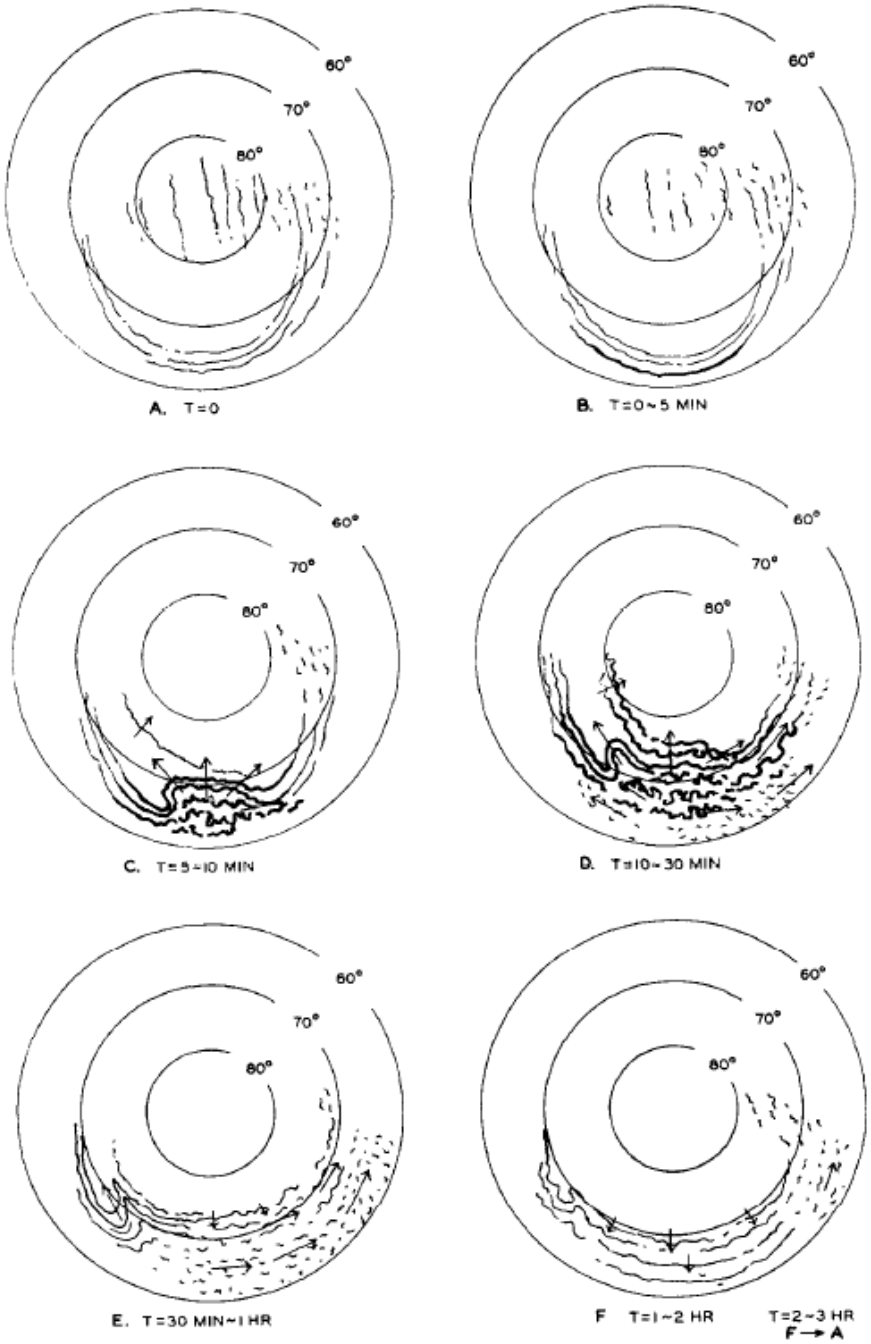

Figure 2.1: Schematic drawing of key signatures observed during the Akasofu's auroral substorm expansive and recovery phase. The centre of the circles is the geomagnetic north pole, with the Sun towards the top of the diagram. Figure from *Akasofu* [1964].

in the midnight sector of the auroral oval [*Akasofu*, 1964]. Often, it is the most equatorward arc that brightens, however in some cases an arc which is barely visible prior to the substorm is the one that brightens, as if there is a sudden formation of an arc. *Akasofu* [1964] also reported that the '*brightening is usually accompanied by the development of a distinct ray structure*', which, as will be explained later, is the topic of research revisited and explored in this thesis some 53 years later. As the expansive phase develops, the arc which initially brightened rapidly expands poleward, resulting in the development of a bulge. The bulge then also expands eastward and westward (Figure 2.1*C*). At the western edge of the auroral bulge, folds in the auroral arc are formed. These folds continue to move westward and are called a '*westward travelling surge*' (Figure 2.1*C, D*).

Once the auroral bulge has reached its highest latitude, it may remain at this point for 10-30 minutes, or return equatorward. The end of auroral expansion and the start of auroral retreat is the start of the recovery phase. The westward surge continues to propagate westward, however at a reduced speed. Often the surge develops into loops. In the morning sector, equatorward of the former bulge, any arc structure disappears to form patches which slowly drift eastward (Figure 2.1*E*). The remaining arcs slowly propagate equatorward, back into the initial '*quiet phase*' configuration. This entire cycle varies in length depending on the activity level, however for isolated events last $\sim 1-3$ hours.

Prior to Akasofu's substorm, *Heppner* [1954, 1958] made the first link that dynamic auroral displays were accompanied by a sharp decrease in the north-south (H) magnetic field component. Akasofu's expansion and recovery phases, as we now know them, are the second and third substorm phases. The first phase, the growth phase, was named by *McPherron* [1970], following the proposition by *Axford* [1969] that prior to a substorm the total magnetic flux in the tail of the magnetosphere increases due to an imbalance between the dayside and nightside reconnection rates. *McPherron* [1970] reported significant deviations to the horizontal component of the ground-based magnetic field measured in the auroral region, in the hour prior to the substorm expan-

Substorm Phase	Ionospheric Processes	Magnetospheric Processes
Growth Phase ~30-60 mins	• Expansion of the polar cap • Enhancement of the electrojets	• Build up of open magnetic flux in the lobes due to dayside reconnection, increasing the cross-section of the tail • Gradual plasma sheet thinning
Onset	• Sudden brightening of an arc at the equatorward edge of the auroral oval	
Expansion Phase ~30-60 mins		
Substorm	• Poleward expansion of the aurora. • Auroral breakup	• Near-Earth instability/ tail reconnection • Closure of open flux, decreasing the tail cross-section
Pseudo Breakup	• Brightening of the arc, but no significant poleward motion • Does not result in auroral breakup	• Particle injections into the inner magnetosphere • Dipolarisation of the tail magnetic field • Transient Earthward plasma flows
Recovery Phase ~60-120 mins	• Reduction in auroral brightness	• Magnetospheric topology reordering into a quiet state

Table 2.1: A summary of the key, large-scale phenomena constituting the auroral and magnetospheric substorm (after *Lui*, 1991).

sion phase. However *McPherron* [1970] also linked geomagnetic bays to the previous studies by *Heppner* [1954, 1958]; *Akasofu* [1964, 1977]; *Axford* [1969] to conclude that these deviations are linked to enhanced magnetospheric convection, and the storage of energy in the magnetotail during the growth phase, prior to the explosive release of stored energy during the expansion phase.

The equatorward motion of auroral arcs, initially reported by [*Akasofu*, 1964] at the end of the recovery phase, are now also considered to be a growth phase phenomenon. An imbalance between reconnection rates on the dayside and nightside magnetosphere causes a build up of open magnetic flux in the magnetotail lobes. These open magnetic field lines are tied to the polar cap and result in the expansion of the polar cap during the substorm growth phase [*Cowley and Lockwood*, 1992]. The poleward edge of the auroral oval is located at the boundary between open and closed magnetic field topology, and hence the size of the auroral oval can by used to estimate the amount of open magnetic flux in the system [*Milan et al.*, 2003]. The build up of flux in the tail during the substorm growth phase is consistent with the the equatorward motion of auroral arcs in the midnight sector of the auroral oval.

Table 2.1 highlights the large-scale, key processes that occur during the

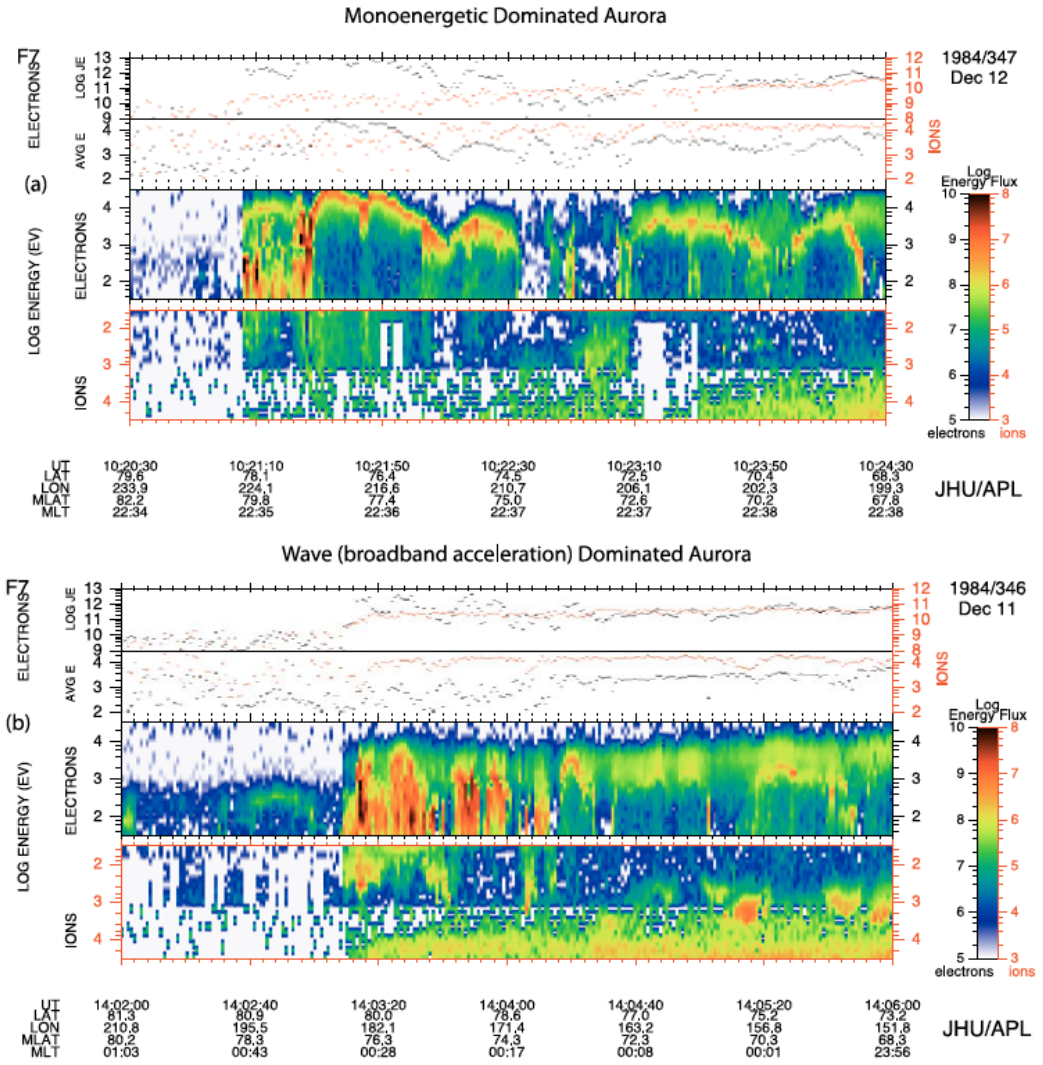

Figure 2.2: *a*) DMSP particle data showing monoengergetic precipitation auroral electrons. *b*) An interval where broadband energy precipitating electrons are dominant. Figure from *Newell et al.* [2009].

substorm phases in the ionosphere and magnetosphere, based on *Lui* [1991].

2.2 Auroral Processes

The aurora are produced when electrons and protons incident on the Earth's ionosphere excite the constituent atoms and molecules. The typical energies of precipitating electrons which cause auroral emissions are 1-10 keV, which are able to penetrate to $100 - 150$ km altitudes [*Rees*, 1963]. However lower energy electrons of < 1 keV can result in red emissions above 200 km altitude [*Rees*, 1963]. Typical electrons in the magnetosphere are much lower than the

energies of the order of 1 keV necessary for the common auroral emissions. Hence these electrons must undergo acceleration processes before they reach the ionosphere in order to generate the aurora.

There are two processes which accelerate electrons up to high enough energies in order to generate the discrete aurora. The discrete aurora can be split into two distinct categories: monoenergetic and broadband.

The most common type of discrete aurora is monoenergetic [*Newell et al.*, 2009], which is associated with electron acceleration by quasi-static, field-aligned electric fields. A potential drop will accelerate all electrons by the amount of the potential drop, this results in electrons accelerated to a single energy, hence the name monoenergetic. Figure 2.2*a* shows a typical electron energy spectrogram (third panel) of a low altitude DMSP satellite overpass of monoenergetic aurora. The data shows a peak of energy flux at a narrow range of energies, however the peak energy rises and then drops as the satellite crosses the arc, e.g., between ∼10:21:25 − 10:22:00 UT. This is also known as an 'inverted-V' arc, due to this shape of the precipitating energy flux in the energy spectrogram. In the ionosphere electron transitions in Oxygen or Nitrogen atom/molecules require a precipitating electron with a specific energy. Hence, electrons with different energies can result in a range of atomic/ molecular transitions. As a potential-drop accelerates electrons to a narrow range in energies, this manifests itself in auroral signatures which can only be observed in a single emission line, see Section 1.3.5).

At small scales resulting from finite ion gyroradius or electron inertial effects, Alfvén waves can become dispersive, resulting in parallel electric fields. These electric fields can efficiently accelerate electrons over long distances parallel to the magnetic field. Electrons are accelerated to a range of energies dependent on the length of their interaction with the wave, thus an enhancement in electron energy flux can be observed across a wide range of energies. When incident with ionospheric molecules, multiple electron transitions can be excited resulting in the emission of multiple auroral spectral lines.

Broadband aurora, are caused by electrons accelerated to a wide range of energies [*Johnstone and Winningham*, 1982; *Lotko*, 1986], and are caused by

dispersive Alfvén waves [*Ergun et al.*, 1998; *Chaston et al.*, 2003], which have field-aligned electric field components. Figure 2.2*b* shows a typical electron energy spectrogram signature when the precipitating electrons have been accelerated by Alfvén waves. The electron energy flux is enhanced over a much wider range of energies when the satellite crosses an Alfvénic arc, e.g., between ∼14:03:25 − 14:03:40 UT.

At quiet times, Alfvén wave-accelerated aurora only contributes 6% of the hemispheric energy budget [*Newell et al.*, 2009]. However the auroral precipitating power of broadband aurora increases by 182% during substorms, in comparison to a 79% increase for monoenergetic auroral precipitation [*Newell et al.*, 2010], suggesting that Alfvén waves may play an important role in the substorm onset process.

2.3 Auroral Beads at Substorm Onset

Even though the definition of a substorm has been established for over fifty years, the exact processes which lead to the onset of the substorm expansion phase are still actively disputed. The onset of a substorm is seen as the global brightening and poleward expansion of the most equatorward arc in the midnight sector of the auroral oval. However the continuous improvement of space- and ground-based observations of the substorm aurora has lead to more detailed observations and analysis of the '*distinct ray structure*' along the substorm onset arc [*Akasofu*, 1964]. Similar rayed structures were reported previously, e.g., *Heppner* [1954]; *Davis* [1962], prior to the substorm terminology was developed. However, mentions that auroral rays were observed during '*aurora displays*' which were coincident with the formation of geomagnetic bays, suggest that rays were likely observed during intervals which we now recognise as substorms.

For the remainder of this thesis, will will refer to the rayed structure of auroral arcs, or azimuthal auroral forms/structures as auroral beads. It is entirely conceivable that the auroral beads observed from space discussed next, are synonymous to the rays perviously observed by *Heppner* [1954];

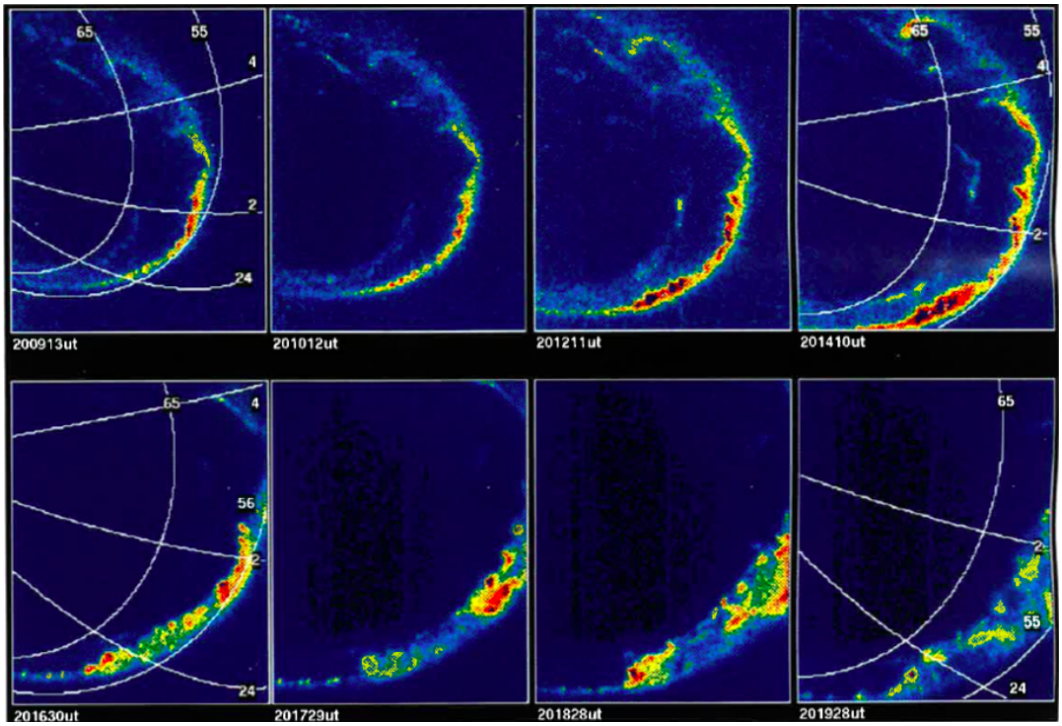

Figure 2.3: Auroral observations of a substorm from the UVI experiment on the Viking satellite. Auroral beads are visible in the earlier frames. Figure from *Henderson* [1994].

Davis [1962]; *Akasofu* [1964].

The first published images of auroral beads which were reported by *Henderson* [1994] are shown in Figure 2.3. These are the first accounts of beads observed from the space-based imagery upon the Swedish Viking mission [*Anger et al.*, 1987]. Regular azimuthal structuring of the brightest auroral arc are observable, especially in the earlier images taken at 20:09:13 UT and 20:10:12 UT. The relatively slow temporal cadence of subsequent space-based imagers (e.g., the Far UltraViolet/ Wideband Imaging Camera (FUV/WIC) on the Imager for Magnetopause-to-Aurora Global Exploration (IMAGE) satellite, *Burch*, 2000) are most-probably the reason why observations of auroral beads from space have only been reported rarely since, e.g., *Henderson* [2009]. From the original observations by *Henderson* [1994], it was concluded that the likely explanation for auroral beads was a ballooning instability in the near-Earth magnetosphere, as the beads were observed at the equatorward edge of the auroral oval: the location that maps to the transition region from dipolar to stretched magnetic field topology [*Samson et al.*, 1992a], where large-scale

pressure gradients exist.

Henderson [2009] observed auroral beads using the IMAGE FUV/WIC imager during a substorm on 21 November 2002. The auroral beads were observed over at least 4 minutes, however with an image cadence of 2 minutes it is difficult to tell how long they persisted. The growth in auroral intensity was calculated from the peak count rate in the onset region of 3 consecutive images, spanning 4 minutes in time during which the auroral beads were observed, was calculated as 0.00533 s^{-1}. However this does not correspond to the growth of the beads, rather the growth in the total intensity of the aurora. It is also possible that this growth rate is an underestimation due to the low temporal cadence of the imager, meaning that some of the growth in auroral intensity was missed.

Auroral beads have been reported more frequently by data from ground based auroral imagers, in particular the THEMIS all-sky imagers [*Mende et al.*, 2008]. *Donovan et al.* [2006] observed the formation beads using the THEMIS ASIs with azimuthal wavelengths of $\sim$ 100 km along the breakup arc during a pseudo-breakup. *Sakaguchi et al.* [2009] observed four substorm events with auroral beads using 30 Hz all-sky TV cameras. In a couple of events, the beads observed had longitudinal wavelengths of $\sim 30-60$ km, however the remaining two events had wavelengths of $\sim 100-200$ km. When mapped to ~ 10 R_E in the plasma sheet using a Tsyganenko 89 magnetic field model [*Tsyganenko*, 1989], the beads with spatial scales of $30-60$ km in the ionosphere, mapped to scale sizes of $600-1200$ km in the equatorial magnetosphere. These scales are similar to the ion gyroradius of 1-10 keV protons in a 12 nT magnetic field, of $\sim 500-1400$ km, resulting in the conclusion by *Sakaguchi et al.* [2009] that beads of this scale size are not caused by an MHD instability.

Motoba et al. [2012] observed auroral beads along the substorm onset arc at magnetically conjugate stations in Iceland and Antarctica with wavelength $\sim 30-50$ km. Figure 2.4*a* shows the beads observed from both stations at 23:09:40 UT. Figure 2.4*b* shows the beads mapped into the Northern hemisphere at 110 km altitude along T96 [*Tsyganenko*, 1995] magnetic field model. The beads almost have a one-to-one correspondence with each other, between

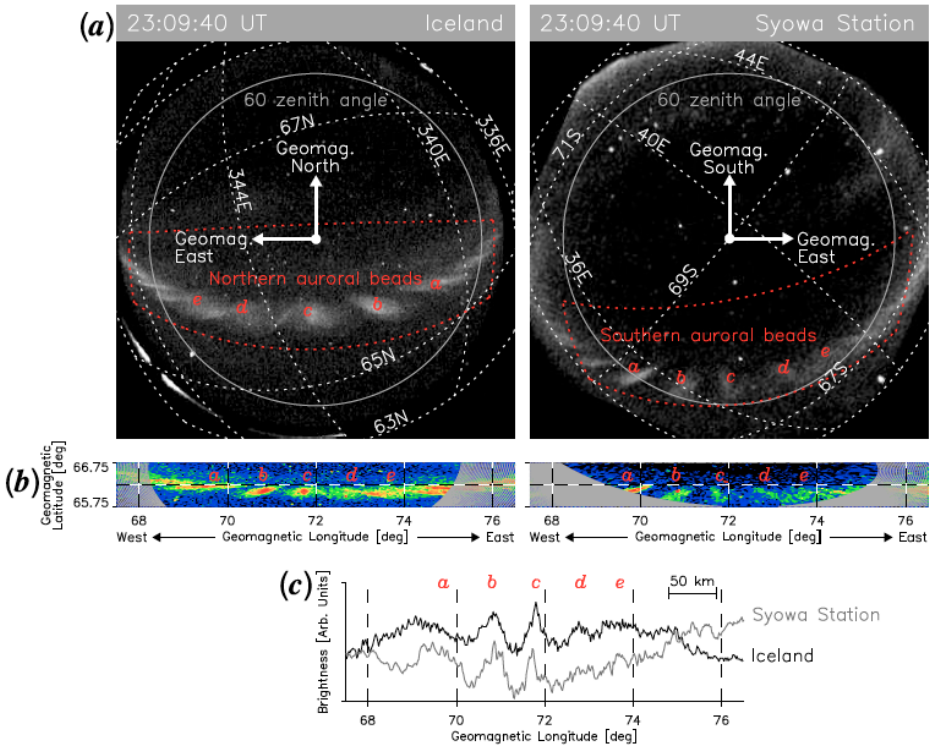

Figure 2.4: *a*) Images taken simultaneously of auroral beads in Iceland and Syowa at 23:09:40 UT on 30 September 2011, with the top of the Figures being the Northern and Southern pole respectively. Some geomagnetic latitudes and longitudes are indicated by grey dotted lines. The conjugate auroral beads are labelled with *a*-*e* in each of the images. *b*) Auroral beads projected to 110 km in the northern hemisphere using T96 magnetic field model. *c*) Longitudinal arc intensity of average auroral brightness between 65.9^o and 66.25^o geomagnetic latitude with the Iceland trace in black, and Syowa trace in grey. Figure from *Motoba et al.* [2012].

the two hemispheres. When mapped along T96 model into the equatorial magnetosphere, the beads map to -7.75 to -8.25 R_E, with azimuthal wavelength of $1500 - 1800$ km, which is similar to the gyroradius of 1-10 keV ions as found by *Sakaguchi et al.* [2009]. The remarkable similarities between observations in the northern and southern hemispheres suggest that the beads have a common driver in the equatorial region of the magnetosphere, such as an instability.

A detailed Fourier analysis of auroral beads by *Rae et al.* [2010] allowed the determination of exponential growth rates as a function of spatial scale to be determined. The beads observed had wavelengths of ~ 60 km mapping to ~ 2100 km at a radial distance of $5.6 - 6.3 R_E$ in the equatorial magnetosphere along a T96 magnetic field model, which is much closer than found by *Sakaguchi et al.* [2009]. The in-situ magnetic field strength at geosynchronous orbit measured by the approximately conjugate GOES east satellite was ~ 90 nT. By assuming a typical ion temperature of 10 keV, this results in an estimated ion gyroradius of ~ 160 km, which is more than 10 times smaller than the estimated bead scale at this location in the magnetosphere. *Rae et al.* [2010] use this information to conclude that the range of spatial scales and growth rates are most consistent with a Shear-Flow Ballooning Instability [*Voronkov et al.*, 1997], or a Cross-Field Current Instability (e.g., *Lui et al.*, 1991). Thus, based on magnetic field line mapping to estimate the bead spatial scale in the magnetosphere, it is difficult to determine an accurate estimate at this highly dynamic time prior to substorm onset. Together with uncertainty about the magnetic field strength at the location of the beads, this can result in a wide range of ion-gyroradii, making it impossible to definitively determine whether beads are caused by a kinetic or MHD instability phenomenon.

Hosokawa et al. [2013] used conjugate observation of auroral beads and an all-sky TV camera and SuperDARN radar to detect large velocity shears around the auroral beads. This is consistent with the proposed Shear-Flow Ballooning Instability [*Voronkov et al.*, 1997], where velocity shear and pressure gradients couple together to excited the instability and produce auroral vortices. *Friedrich et al.* [2001] used meridian scanning photometer data, to-

gether with all-sky imager data to show that large-scale vortex structures in the ionosphere form 1-5 minutes prior to the beginning of enhanced magnetic reconnection in the tail, as determined by the poleward motion of the poleward border of the 640.0 nm emission line.

2.4 Mapping the Substorm Onset Arc to the Magnetosphere

An important part of understanding the auroral beads, the processes which cause them and why they are frequently observed in the minutes prior to substorm onset, is knowing the region of the magnetosphere to which they map. As we have seen, equilibrium magnetic field models are likely to underestimate tail stretching at highly dynamic substorm times. Instead, the relative regions of the magnetosphere to which the aurora map can be estimated by comparing different auroral emissions.

It is possible to determine the relative location of the substorm onset arc in relation to plasma boundaries, e.g., the inner edge of the plasma sheet and the open-closed field line boundary, with use of multi-spectral auroral data. *Samson et al.* [1992a] used ground-based data form the Canadian Auroral Network for the Origin of Plasmas in the Earth's Neighbourhood (OPEN) Program Unified Study (CANOPUS) array of meridian scanning photometers [*Rostoker et al.*, 1995], in conjunction with a Defense Meteorological Satellite Program (DMSP) satellite to approximate the location of the substorm onset arc in the magnetotail. Firstly, the diffuse signature of the Hydrogen Balmer, Hβ, emission at 486.1 nm was found to be consistent with the precipitation of protons from the edge of the plasma sheet with energies $>$ 20 keV using DMSP observations, originating from the transition region in the magnetosphere between stretched and dipolar magnetic field lines. By studying 33 auroral substorms using ASIs and meridian-scanning photometers, *Deehr and Lummerzheim* [2001] found that the substorm onset arc was located 10-300 km poleward of the location of peak proton precipitation. This was confirmed by observations of auroral vortices which appeared slightly poleward of the peak

in proton aurora [*Voronkov et al.*, 2000].

Hence, the substorm onset arc can be observed in the 557.7 nm emission line, which is embedded within the proton precipitation region. This is equatorward of the poleward edge of the 630.0 nm emission which marks the open-closed field line boundary [*Blanchard et al.*, 1995], as determined by conjugate DMSP data [*Samson et al.*, 1992a], hence the substorm onset location cannot be attributed to tail reconnection. This means that the substorm onset arc maps very closely to the inner edge of the plasma sheet, on closed magnetic field lines, which is a region in the magnetosphere where there are strong pressure gradients.

2.5 Prevalent Substorm Models

The sequence of events leading to substorm onset remains highly disputed. In particular, whether the substorm expansion phase starts with reconnection at the Near-Earth Neutral Line (NENL) at $20 - 25\mathrm{R}_E$, rather than Current Disruption (CD) at $9 - 10\mathrm{R}_E$ in the near-Earth plasma sheet, and the initial trigger of these processes. The NENL and CD models are the most prominent and hotly debated substorm models, although there are many others. Here we describe the NENL and CD models in detail, and briefly outline some of the variations on these models.

2.5.1 Near-Earth Neutral Line Model

The NENL model of substorms began with *Hones* [1976]; *Hones et al.* [1986b], who proposed that reconnection in the magnetotail was the initiating process during substorms. [*Hones et al.*, 1986b] postulated that the reconnection site initially formed at a near-Earth location in the plasma sheet, and causes the brightening and poleward expansion of the aurora. Figure 2.5 shows the initial reconnection site in the near-Earth magnetosphere, located at $\sim 20 - 30\mathrm{R}_E$, *N'* in panels 2-9. Reconnection at this near-Earth location was thought to be the cause of the bright substorm aurora, and results in the tailward ejection of a plasmoid (panels 2-8) . At the final stage of the substorm, the near-Earth

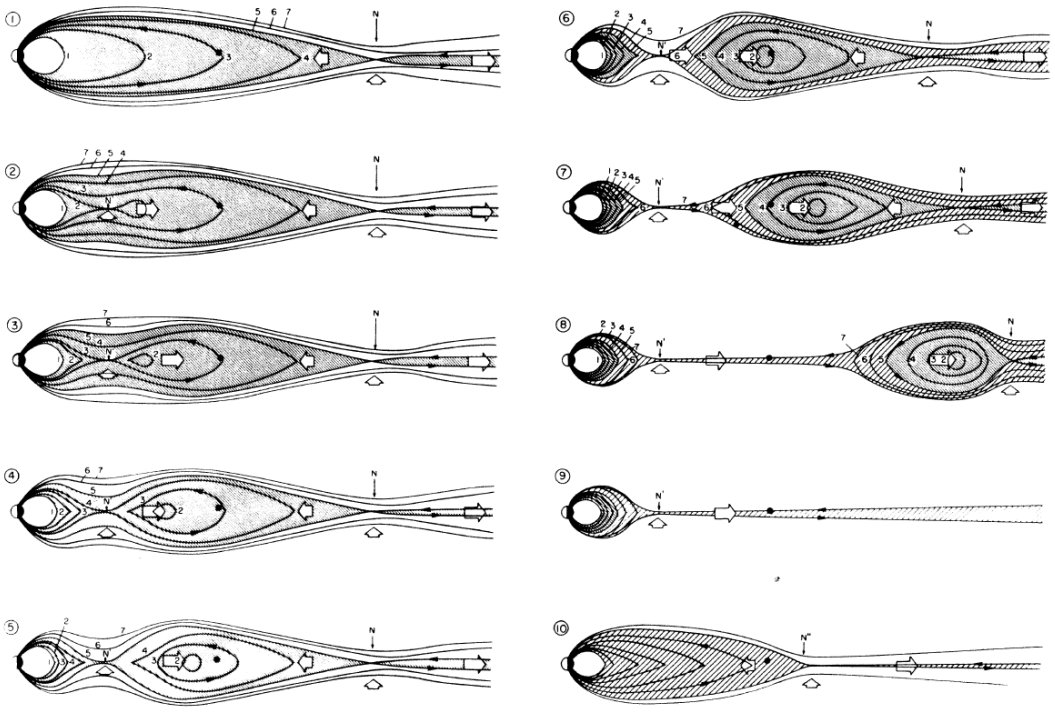

Figure 2.5: Plasma sheet configuration during the early NENL reconnection substorm model. N is the pre-substorm distant neutral line, N' is the near-Earth substorm neutral line and N" is the retreat of the neutral line during the recovery phase. Figure from *Hones et al.* [1986a].

reconnection location was thought to retract tailwards, causing the poleward expansion of the aurora (panel 10 of Figure 2.5).

This initial formulation of the NENL model was later revised by *Baker et al.* [1996], as the tail reconnection site was rarely measured within 20 R_E [*Baumjohann et al.*, 1990; *Angelopoulos et al.*, 1993] and the location of the substorm onset arc rarely mapped beyond 10-15 R_E. Even during very stretched magnetic field configurations, the original NENL model [*Hones*, 1976; *Hones et al.*, 1986b] is unable to explain the initial brightening of the most equatorward auroral arc using tail reconnection alone. Moreover, reconnection in the tail is not expected to directly drive field aligned currents (FACs). *Baker et al.* [1996] suggested instead that reconnection causes earthward and tailward outflows within the plasma sheet, which were subsequently observed and named Bursty Bulk Flows (BBFs) [*Angelopoulos et al.*, 1992]. As BBFs propagate earthward, the increasing plasma pressure and magnetic field strength causes the flows to slow down ('*break*') in the CD region at 8-

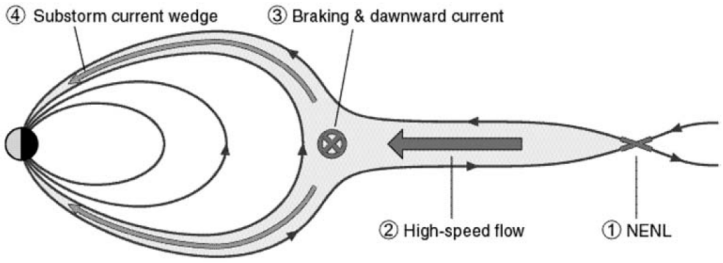

Figure 2.6: A schematic to demonstrate the revised NENL substorm model. magnetic reconnection initiates the substorm (1), generating high speed earthward plasma flows (2). The flows are broken in the near-Earth region (3), triggering the substorm instability at the near-Earth edge of the plasma sheet which results in the substorm current wedge (4). Figure from *Lui* [2004].

10 R_E. Here the flows drive field aligned currents, which are observed in the ionosphere by auroral brightening, constituting the substorm current wedge.

Angelopoulos et al. [2008] reported evidence of reconnection at least 1.5 minutes prior to auroral intensification using multi-point space-based measurements at different radial distances in the tail using satellites from the THEMIS mission, thus supporting the NENL model. However the timing of the events reported were disputed when re-evaluated by *Lui* [2009], who claimed that the '*unconventional*' reconnection signatures observed by *Angelopoulos* [2008] could also be interpreted as plasma sheet thinning. *Lui* [2009] found that, when considering '*conventional*' signatures of reconnection, the event studied was consistent with the Current-Disruption model of substorms based on the sequence of events observed.

2.5.2 Current Disruption Model

In the Current Disruption Model of substorms, the substorm is initiated by a reduction and diversion of the cross tail current into the ionosphere, forming the substorm current wedge (e.g., *Lui*, 1991; *Roux et al.*, 1991). The expansion phase onset starts with the sudden reduction of the cross tail current due to an instability at the inner-edge of the plasma sheet. This causes part of the cross-tail current to be diverted along magnetic field lines and through the auroral ionosphere. The enhancement of electron precipitation, causes the brightening of the auroral arc in this region. The diversion of the current

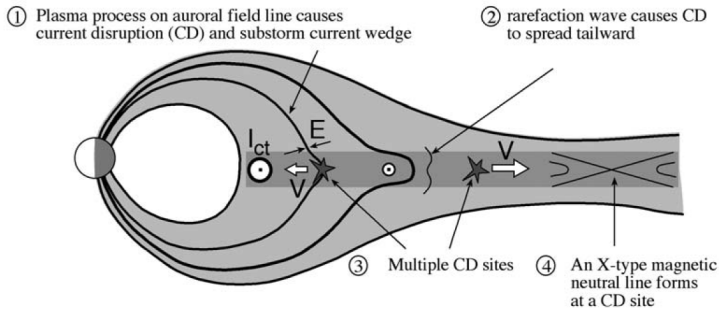

Figure 2.7: A schematic to show the substorm Current Disruption model. The substorm plasma instability is excited in the near-Earth tail, disrupting the cross tail current and setting up the substorm current wedge (1). This causes field dipolarisation and hence a tailward propagating rarefaction wave (2). Current disruption can occur in multiple regions of the tail (3), which eventually triggers reconnection at the NENL (4). Figure from *Lui* [2004].

also causes a sudden relaxation of the stretched magnetic field, resulting in poleward expansion of the aurora. Due to the dipolarisation of the previously stretched magnetic field, the region tailward of the CD region is left depleted of plasma, resulting in a rarefaction wave which propagates down tail. The rarefaction wave thins the midtail plasma sheet, and triggers reconnection at the NENL.

Hence the NENL and CD disagree on the sequence of the events which constitute a substorm. However, whether or not the substorm is initiated by reconnection in the tail, or current disruption is initiated locally in the near-Earth plasma sheet, these models do agree that a plasma instability at the inner-edge of the plasma sheet disrupts the cross-tail current, resulting in the formation of the substorm current wedge (SCW).

2.5.3 Other Models

Various modifications to the NENL and the CD models have been proposed to lead to the onset of a substorm. A couple of examples are given below.

- The **Near-Earth Geophysical Onset Model** [*Maynard et al.*, 1996] This model provides a new perspective on the CD model (e.g., *Lui*, 1991; *Roux et al.*, 1991) by highlighting the importance of communication between the ionosphere and magnetosphere through bouncing Alfvén waves. The current disruption process launches an Alfvén wave towards

the ionosphere, which is reflected back into the magnetosphere. Whether Alfvén waves bouncing between the northern and southern hemispheres interact constructively or destructively, is hypothesised to result in a full substorm or a pseudo-breakup respectively.

- **Plasma Intrusion Model** [*Nishimura et al.*, 2010]
  Nishimura et al. [2010] observed, on the basis of 249 self-selected events, that the substorm process was initiated by a poleward boundary intensification of the auroral oval. This was followed by the equatorward propagation of an auroral streamer, an approximately North-South aligned auroral arc, towards the substorm onset arc. This streamer was proposed to be the ionospheric projection of a magnetotail flow ejected from the reconnection site at the NENL. This enhanced earthward plasma flow excited a near-Earth instability, resulting in auroral breakup. However not all substorm onsets are accompanied by the appearance of auroral streamers [*Rae et al.*, 2009a; *Mende et al.*, 2011].

2.6 Plasma Sheet Evolution During a Substorm

As we have seen in the previous section, the different substorm onset models disagree over the temporal sequence of the magnetospheric events which constitute a substorm. However, the vast majority of models agree that an instability (whether locally or externally driven) at the inner-edge of the plasma sheet is responsible for current disruption and the formation of the substorm current wedge. Identifying and understanding the instability which causes this process will fundamentally allow the trigger of the substorm to be identified, e.g., whether the instability is excited due to earthward plasma flows (from reconnection) or due pressure perturbations in the near-Earth magnetosphere, independent of the processes in the tail.

The substorm is usually thought of as a release of magnetic energy only, and the state of the plasma sheet is often ignored during substorm studies. However understanding plasma sheet response to substorm activity (and vice versa) is the only way which will allow the substorm trigger to be identified.

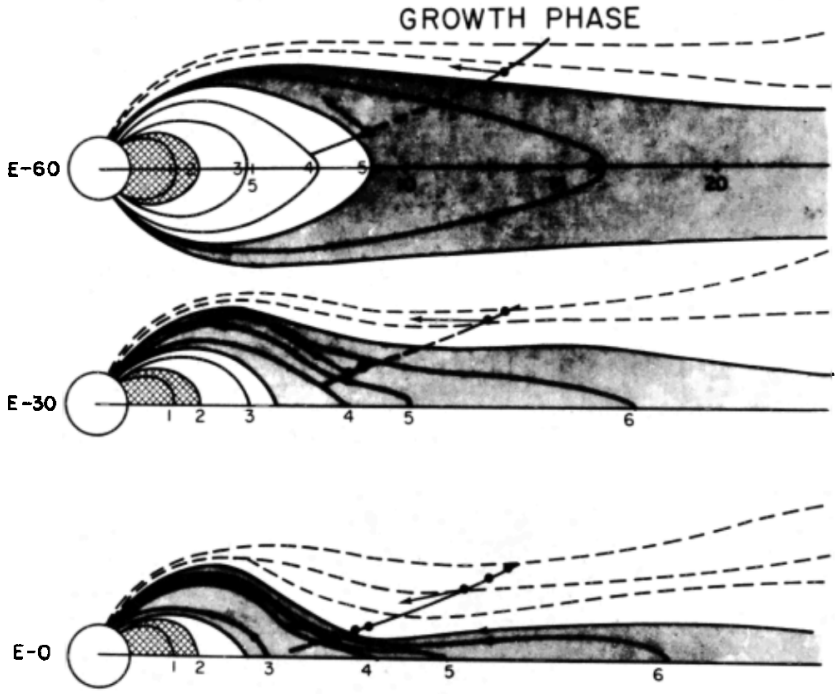

Figure 2.8: Schematic illustration of thinning the the plasma sheet observed during a substorm on 15 August 1968 by the Ogo 5 satellite. Figure from *McPherron et al.* [1973].

Plasma sheet parameters such as pressure gradients and magnetic and electric fields affect communication between the magnetosphere and ionosphere, as well as communication between different regions of the magnetotail such as the Near-Earth Neutral Line and Current Disruption region. Understanding the communication between these regions is vital, as substorms always constitute auroral breakup in the ionosphere, current disruption in the near-Earth magnetosphere and reconnection in the tail, showing that there is a fundamental link between these processes.

During times of high solar wind driving, when the solar wind couples with the magnetosphere due to magnetopause reconnection on the dayside, magnetic flux builds up in the magnetotail lobes, the substorm growth phase. The built up flux in the lobes, exerts a higher pressure on the central plasma sheet as the total pressure in the plasma sheet balances the lobe pressure. Using 9 years observations of the plasma sheet by the of Cluster satellites, *Forsyth et al.* [2014] showed that the plasma sheet is thermodynamically adiabatic during the growth phase: the pressure and temperature increase during times of high solar wind driving, however the plasma density remain approx-

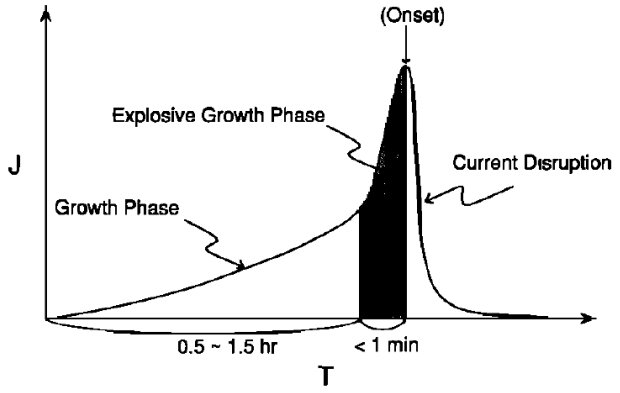

Figure 2.9: The explosive growth in tail current intensity at the end of the substorm growth phase, followed by a sudden disruption of the current. Figure from *Ohtani et al.* [1992].

imately constant. This indicates that plasma sheet instabilities at the end of the growth phase are likely to be dependent on variations in plasma pressure and temperature, and not plasma density.

The cross-tail current also increases during the substorm growth phase [*Fairfield and Ness*, 1970; *Aubry and McPherron*, 1971], due to the stretching of the magnetotail due to the accumulation of open magnetic flux (e.g., *Axford*, 1969; *McPherron*, 1970; *McPherron*, 1972). This is accompanied by the thinning and earthward motion of the plasma sheet [*Hones et al.*, 1971; *McPherron*, 1972; *McPherron et al.*, 1973]. Figure 2.8 shows the way in which the plasma sheet thins during the growth phase. In the top panel, ~ 60 minutes prior to substorm onset, the plasma sheet is thick and extends to the fifth magnetic field line (labelled by 5). However in the middle panel, ~ 30 minutes prior to substorm onset and during the substorm growth phase, there is thinning of the plasma sheet, particularly close to earth. The magnetic field topology has become more tail-like and the inner-edge of the plasma sheet has moved earthward (from field line 5 to 4). In the final panel, at the end of the growth phase, the plasma sheet has thinned significantly, with the magnetic field lines stretching into a more tail-like configuration. The inner-edge of the plasma sheet has moved earthward beyond field line 3.

Using Active Magnetospheric Particle Tracer Explorer Charge Composition Explorer (AMPTE/CCE, *Dassoulas et al.*, 1985), *Ohtani et al.* [1992]

investigated the magnetic field and energetic ion flux within the current disruption region at the end of the growth phase when the plasma sheet is very thin. When the spacecraft was earthward of the current disruption region, a distinct interval lasting $\sim$ 1 minute was observed, which *Ohtani et al.* [1992] called the '*explosive growth phase*'. During this interval a sharp depression in the north-south (z) component of the magnetic field and an enhancement of ion flux tailward of the spacecraft was observed, suggesting that the cross-tail current was explosively enhanced during this time. This enhancement in current was attributed to the thinning of the plasma sheet. When the plasma sheet thickness reduces down to the scale of less than an ion gyroradius, the ions become unmagnetised. This allows them to move independently to the magnetic field, unlike the electrons, and thus briefly enhancing the intensity of the tail current sheet during the explosive growth phase and shortly prior to current disruption.

Changes in plasma sheet properties during the substorm growth phase, such as an enhancement in plasma sheet pressure, rapid plasma sheet thinning and an explosive enhancement of the cross-tail current can result in a wide range of MHD (large-scale) and kinetic (small-scale) instabilities. In the following section we discuss a few common instabilities which have been proposed to play a part in the substorm onset process in detail.

2.7 Common Plasma Sheet Instabilities

In order to understand the auroral beads that form azimuthally along the substorm onset arc in the minutes prior to substorm onset, we need to investigate and understand any plasma instabilities which may be capable of causing this periodic signature. We focus on instabilities that can explain azimuthal structuring in the near-Earth plasma sheet that are hypothesised to be projected into the ionosphere by field aligned currents to cause auroral beads.

2.7.1 The Ballooning Instability

The ballooning instability refers to a Rayleigh-Taylor type instability in the magnetotail. In a traditional fluid, the Rayleigh-Taylor instability describes the waves which grow on an interface between two fluids when a heavier fluid is balanced on top of a lighter fluid. A small perturbation to the interface causes the lighter fluid to be displaced upward, and the heavier fluid downward, decreasing the potential energy of the system. This results in the disturbance, or wave on the interface between the two media growing until a steady state is reached [*Rayleigh*, 1882].

In the following sections we describe the different types of ballooning instability proposed to occur at the near-Earth edge of the plasma sheet. The key differences are:

- In an ideal MHD ballooning instability, the entirety of the plasma sheet is ballooning unstable, with a very low instability threshold of $\beta \geq 1$ [*Cheng*, 2004].
- When taking into account kinetic effects, the instability threshold increases to $\beta \geq 50$ [*Cheng and Lui*, 1998].
- In the shear-flow ballooning instability [*Voronkov et al.*, 1997], the ballooning instability is initially driven by a Kelvin-Helmholtz vortex.

2.7.1.1 MHD Ballooning Instability

The classical Rayleigh-Taylor instability in a plasma is analogous to the Ballooning Instability at the inner-edge of the plasma sheet. A plasma configuration which is unstable to the Rayleigh-Taylor instability is shown in Figure 2.10, where a (heavier) plasma is balanced on top of a (lighter) vacuum. This configuration is supported by a magnetic field in the B_0 direction, acting out of the page parallel to the interface between the two fluids, which is counteracting the gravitational force pulling the plasma down. However a perturbation to the boundary allows the Rayleigh-Taylor instability to develop. The interchange mode is a special case of ballooning instability, where the instability does not perturb the background magnetic field [*Hameiri et al.*,

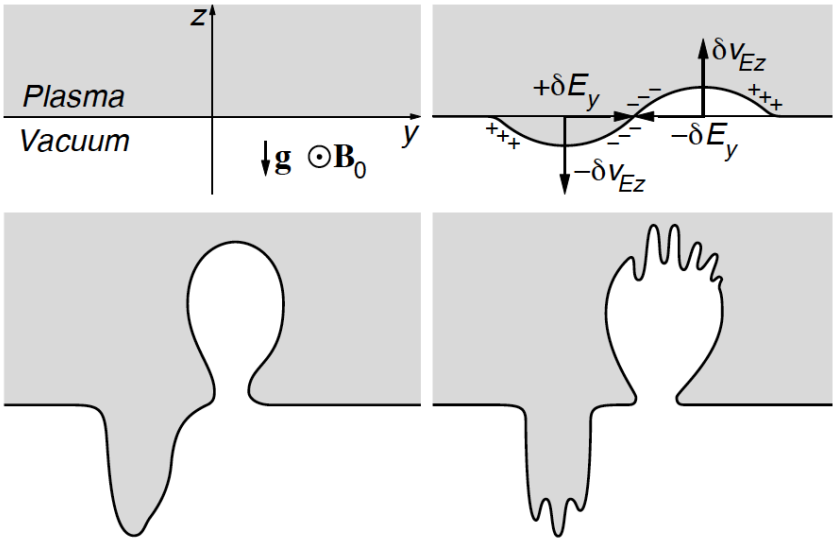

Figure 2.10: The plasma configuration unstable to the Rayleigh-Taylor Instability [*Treumann and Baumjohann*, 1997]

1991].

In the magnetotail, instead of a heavy fluid balanced on a light fluid, a pressure gradient develops in the transition region between dipolar-like and stretched magnetic field topology. Instead of the gravitational force acting on the heavier fluid in the traditional Rayleigh-Taylor instability, the near-Earth plasma sheet is in a delicate balance between the inward confinement force due to the magnetic field line curvature, and the outward plasma pressure [*Hameiri et al.*, 1991]. Figure 2.11*a* shows the schematic of the ballooning instability, with the higher density plasma confined to lower L-shells in a more dipolar magnetic field region. The magnetic field line curvature confines the higher density plasma, however a perturbation to the boundary between high and low plasma pressure can cause the ballooning instability to be initiated. A perturbation to the boundary induces an electric field perpendicular to the radial perturbation, (due to $\mathbf{E} = -\mathbf{v} \times \mathbf{B}$). This electric field causes alternate regions of predominantly positive and negative charge to form, as is shown in Figure 2.11*a*. In order to conserve quasi-neutrality, regions of negative charge accumulation must be dissipated. Charge accumulation usually happens at an interface between two mediums of different density. The less dense medium may not have enough charge carriers to carry the current across the interface.

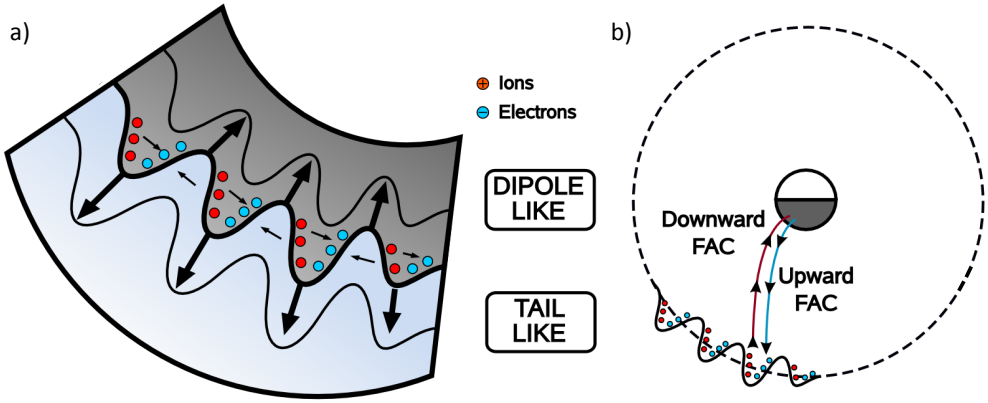

Figure 2.11: *a*) Schematic of a ballooning instability due to a pressure perturbation resulting in bunching of electrons and ions. *b*) This results in alternating upward and downward field aligned currents into the ionosphere, resulting in auroral beads. Figure adapted from *Henderson* [2009].

This can result in the current being diverted along magnetic field lines, causing the electrons to precipitate into the ionosphere as field-aligned currents (Figure 2.11*b*), producing the bright auroral beads observed in the minutes prior to substorm onset.

Ballooning modes are the manifestation of the coupling together of the Alfvén mode and slow mode MHD waves described in Section 1.2.3 [*Hameiri et al.*, 1991; *Liu*, 1997]. A higher β plasma sheet, where the plasma pressure dominates over the magnetic pressure, is more unstable to the ballooning instability [*Liu*, 1997].

Cheng and Zaharia [2004] investigated the stability of the MHD ballooning instability in the equatorial magnetosphere, and found that the tail is unstable to ballooning when $\beta \geq 1$, i.e., the entire plasma sheet. Figure 2.12 shows results from an ideal MHD model of the ballooning instability. The square of the ballooning mode frequency (mHz^2) in the equatorial plane are shown, where all the field lines beyond 6 R_E in the nightside tail are unstable (the negative frequencies indicate the regions which are ballooning unstable). Field lines which are most unstable to the ballooning instability, have the largest amount of free energy, in order for the instability to grow. Azimuthal current density contours are also shown, with the highest current densities overlapping with the most unstable region of the magnetotail plasma sheet. Neglecting kinetic effects of the instability, means that growth rates are overestimated,

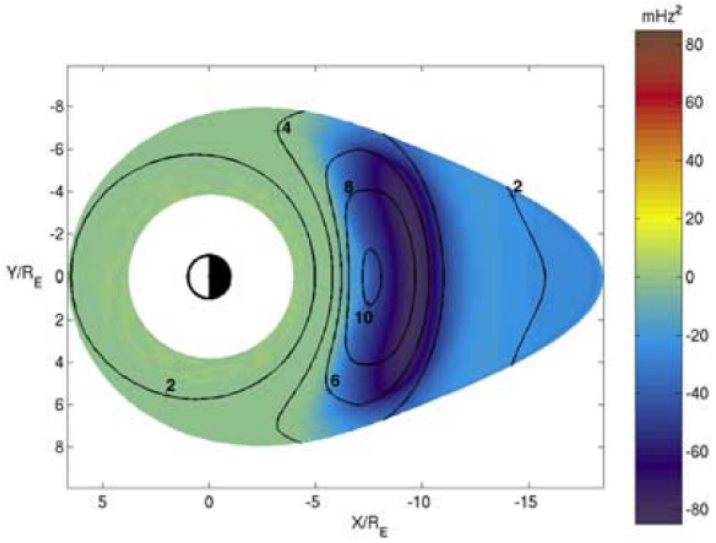

Figure 2.12: The square of the MHD ballooning mode frequency, showing that outside $\sim$ 6 R_E the whole tail is unstable to the ballooning instability. Contours of azimuthal current density (in nAm^{-2} are shown. Figure from *Cheng and Zaharia* [2004].

however it provides an indication of the region of the magnetotail where the most unstable ballooning modes are located.

2.7.1.2 Kinetic Ballooning Instability

Cheng and Lui [1998] used AMPTE/CCE observations to show that low frequency ballooning instability was only observed at the end of the growth phase in the enhanced cross-tail current region when $\beta \geq 50$. This is much higher than calculated by a purely MHD model of the Ballooning instability which showed that a plasma sheet with $\beta \geq 1$ is ballooning unstable [*Cheng and Zaharia*, 2004].

2.7.1.3 Shear-Flow Ballooning Instability

The Shear-Flow Ballooning Instability [*Voronkov et al.*, 1997], is a special type of MHD ballooning instability, which is initially excited, and subsequently enhanced, by a shear-flow vortex. *Voronkov et al.* [1997] suggested the coupling of the Kelvin-Helmholtz and Rayleigh-Taylor instabilities, to explain the destabilisation of the near-Earth plasma sheet due to a pressure gradient instability, even though previous analysis has shown that this region is stable, or only slightly unstable, to ballooning [*Ohtani and Tamao*, 1993].

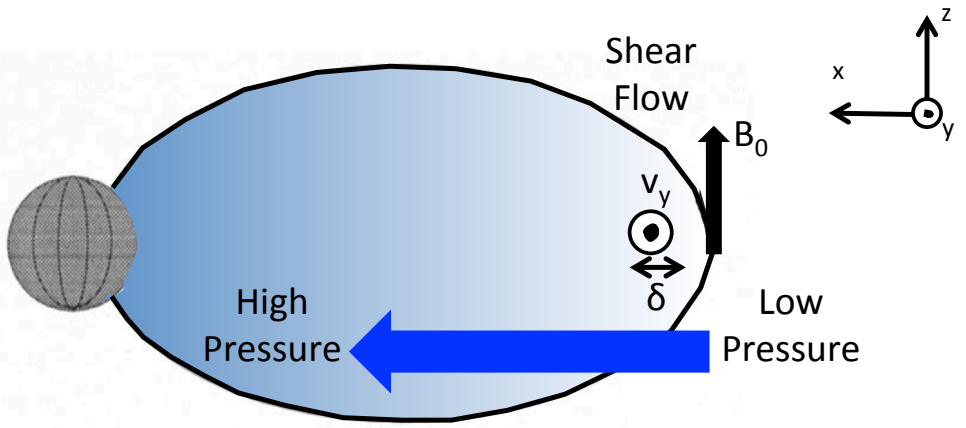

Figure 2.13: The geometry of the region where a Shear-Flow Ballooning Instability is initiated in the GSM $x-z$ plane. A small scale shear flow region flowing in the y direction of width δ is embedded within a region with a large-scale earthward pressure gradient, where the magnetic field topology is slightly stretched. Figure adapted from *Voronkov et al.* [1997].

The Shear-Flow Ballooning Instability is the culmination of large-scale pressure gradients present in the equatorial magnetosphere at the end of the growth phase, and strong shear flows observed in auroral arcs, which *Voronkov et al.* [1997] suggest correspond to a narrow magnetospheric shear-flow embedded within the pressure gradient region and stretched magnetic field. A schematic of this setup is shown in Figure 2.13 in the $x-z$ plane, with the large scale Earthward pressure gradient indicated by the large blue arrow and the narrow shear-flow region, v_y with width δ, flowing out of the page in the y direction.

Figure 2.14 shows a schematic in the GSM x-y plane demonstrating the constructive interaction of a narrow shear-flow region resulting in a shear-flow vortex which moves plasma from a high to a low pressure region. In the linear stage of the instability, a small-scale shear flow region develops into a Kelvin-Helmholtz instability which causes the formation of a vortex. This vortex drives radial plasma flows, causing plasma from a region of higher cross-tail velocity(V_{y1}) and higher pressure to move to a region of lower cross-tail velocity (V_{y2}) and lower pressure, hence disturbing the pressure equilibrium. These perturbations in pressure are unstable to the Rayleigh-Taylor instability, by initiating the flow of plasma 'parcels' against the pressure gradient. The veloc-

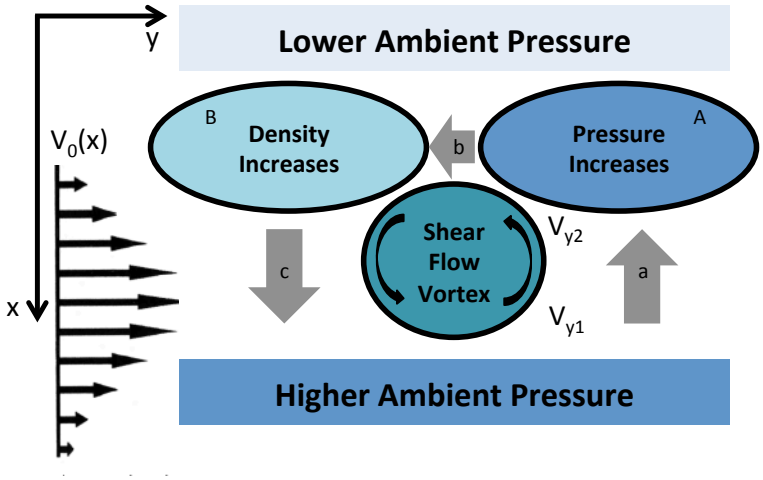

Figure 2.14: A gaussian shear flow causes the formation of a vortex. This causes radial motion of high pressure plasma, causing a pressure perturbation. The Rayleigh-Taylor cell constructively adds to the shear flow vortex. Figure adapted from *Voronkov et al.* [1997].

ity flows initiated by the shear-flow vortex in the radial ($-x$) direction (arrow a) cause plasma from a higher pressure region to move to a lower pressure region (cell A). This pressure imbalance allows the 'bubble' of higher pressure plasma to expand outwards in all directions, but most importantly initiates plasma motion in the $-y$ direction (arrow b) into cell B, i.e., in the same direction as the shear flow vortex. Hence, the density of plasma in cell B is enhanced. This results in an imbalance in the force equilibrium. Magnetic field line curvature in the equatorial plane results in effective centripetal acceleration in the earthward direction, proportional to the particle density, ρ. This is balanced by the tailward plasma pressure. The increase in density, ρ, caused by plasma flowing into cell B, results in an increase in the earthward effective centripetal force, causing plasma to move Earthward in the $+x$ direction (arrow c), out of cell B, towards the higher pressure region

This plasma motion, initiated by the velocity perturbation due to the shear flow vortex, results in constructive interference between the shear-flow vortex, and the Rayleigh-Taylor instability, resulting in the hybrid SFBI with enhanced growth rates, higher than the individual Rayleigh-Taylor and Kelvin-Helmholtz modes alone. In this scenario the shear-flow acts as a trigger for the explosive release of energy due to a pressure gradient. Figure 2.15 shows the growth rates, γ, for the hybrid mode (solid line), Kelvin-Helmholtz

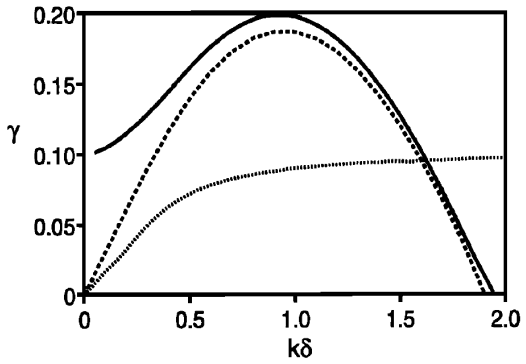

Figure 2.15: The growth rate of the hybrid Shear-Flow Ballooning Instability (solid line), Kelvin-Helmholtz instability (dashed line) and the Rayleigh-Taylor instability (dotted line) obtained from linear analysis of the ideal MHD equations. Figure from *Voronkov et al.* [1997].

mode (dashed line) and Rayleigh-Taylor mode (dotted line) as a function of wavenumber, k, where the x axis is normalised by the width of the shear-flow region, δ. This shows that the hybrid mode exhibits higher growth rates than both the Kelvin-Helmholtz and Rayleigh-Taylor mode for a wide range of wavenumbers. The maximum growth rate exhibited is 0.2 s^{-1} and the hybrid instability is suppressed above $k \geq 2/\delta$, as the Kelvin-Helmholtz vortex does not evolve above these scales. The constructive interaction of the shear flow vortex, with a large-scale pressure gradient which excites a Rayleigh-Taylor instability, results in the increased growth of the Kelvin-Helmholtz vortex.

2.7.2 Cross-Field Current Instability

The free energy source for the cross-field current instability is the relative drift between ions and electrons, i.e., the high current density of the cross-field current at the end of the substorm growth phase, which results in the disruption of the current in the magnetotail, resulting in its diversion into the ionosphere. The cross-field current instability is composed of the Modified Two Stream Instability (MTSI) model and the Ion-Weibel instability (IWI) mode. The MTSI is driven by an imposed current in a system where electrons are magnetised and ions are unmagnetised, resulting in a different drift velocity between the two species. This leads to wave-particle interactions if a wave has a phase velocity lower than the majority of the particles, resulting in energy

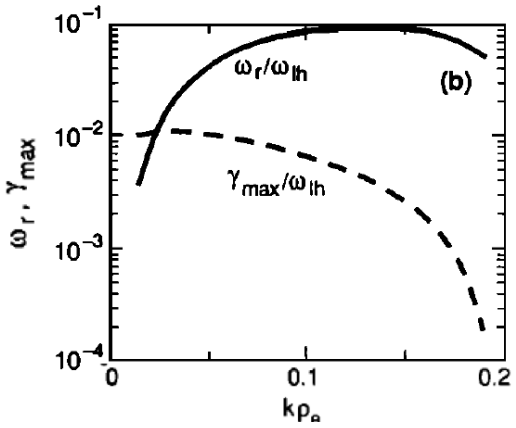

Figure 2.16: The growth rate,γ_{max}, and frequency, ω_r, of the cross-field current instability as a function of wavenumber, k at the inner edge of the plasma sheet with a relative ion drift speed of 1500 kms^{-1}.$n_e = n_i = 0.6$ cm^{-3}, $T_i = 12$ keV, $T_e = 3$ keV, and $B_z = 25$ nT. Figure from *Lui et al.* [1991].

being transferred from the particles to the waves, and the waves to grow. The waves excited by the MTSI are perpendicular to the magnetic field. The IWI instability is driven by a higher relative drift between ions and electrons than the MTSI, and results in waves parallel to the magnetic field. The waves grow due to ion bunching due to $\mathbf{v} \times \delta\mathbf{B}$ motion. This bunching enhances the original relative drift between the species, and the magnetic field component of the wave. Thus, the angle of the resultant excited waves of the CFCI is dependent on the relative ion drift velocity. Often, both instability modes are excited causing waves to propagate at the range of angles relative to the background magnetic field direction.

The cross-field current instability is excited when the plasma sheet thins to a thickness comparable to the ion gyroradius. At these scales the ions become demagnetised and are able to drift duskward at higher speeds, while the electrons are frozen to the magnetic field, resulting in an increase in the cross-field current.

Lui et al. [1991] investigated the cross-field current instability for a range of plasma sheet parameters found to be representative of the inner-edge of the plasma sheet, as observed by AMPTE/CCE. These values are: $n_e = n_i = 0.6$ cm^{-3}, $T_i = 12$ keV, $T_e = 3$ keV, and $B_z = 25$ nT [*Lui et al.*, 1992]. Figure 2.16 shows the resulting waves which are excited with a relative ion

drift speed of 1500 kms^{-1}. At this drift speed the modified two stream and ion-Weibel modes are substantially intermingled, with the highest growth rate occurring at $\theta = 57^o$, which means that the waves are dominated by the modified two stream instability. In this case the growth rate, γ, peaks at 0.4 s^{-1}, at $k = 7.0 \times 10^{-6}$ m^{-1}.

2.8 Wave Observations linked to the Substorm Instability

As we have already seen, auroral beads a frequently observed along the substorm onset arc in the minutes leading up to substorm onset. The exponential growth of auroral bead wave power as documented by [*Henderson*, 2009; *Rae et al.*, 2010] and conjugate observations at ground stations in the northern and southern hemisphere [*Motoba et al.*, 2012] is strong evidence that they are the ionospheric projection of a magnetospheric instability. It is clear that there are many processes at play during a substorm, however it is not clear how the aurora, plasma dynamics in the plasma sheet, and the elevated activity of MHD waves relate to each other. This restricts our understanding of the importance of each of these processes in the detonation of the substorm.

The following section highlights observations of waves from the ground and space, which are likely to be a direct consequence of the instability.

2.8.1 Ground-Based ULF Wave Observations

Substorms have long been linked with Ultra-Low Frequency (ULF) MHD waves (e.g., *Jacobs and Sinno*, 1960; *Saito*, 1969 and references therein), in particular waves in the Pi1-Pi2 frequency band. The ULF wave frequencies were classified by *Jacobs et al.* [1964], with '*Pi*' used for waves with an irregular pattern. Pi1-Pi2 pulsations have periods in the range 1-150 s. [*Jacobs et al.*, 1964]. ULF waves have been studied extensively in the period surrounding substorm onset, particularly using data from ground based magnetometers (e.g., *Olson and Rostoker*, 1975). Deflections in the ground-magnetic field during a substorm, such as the formation of the H-bay are accompanied by

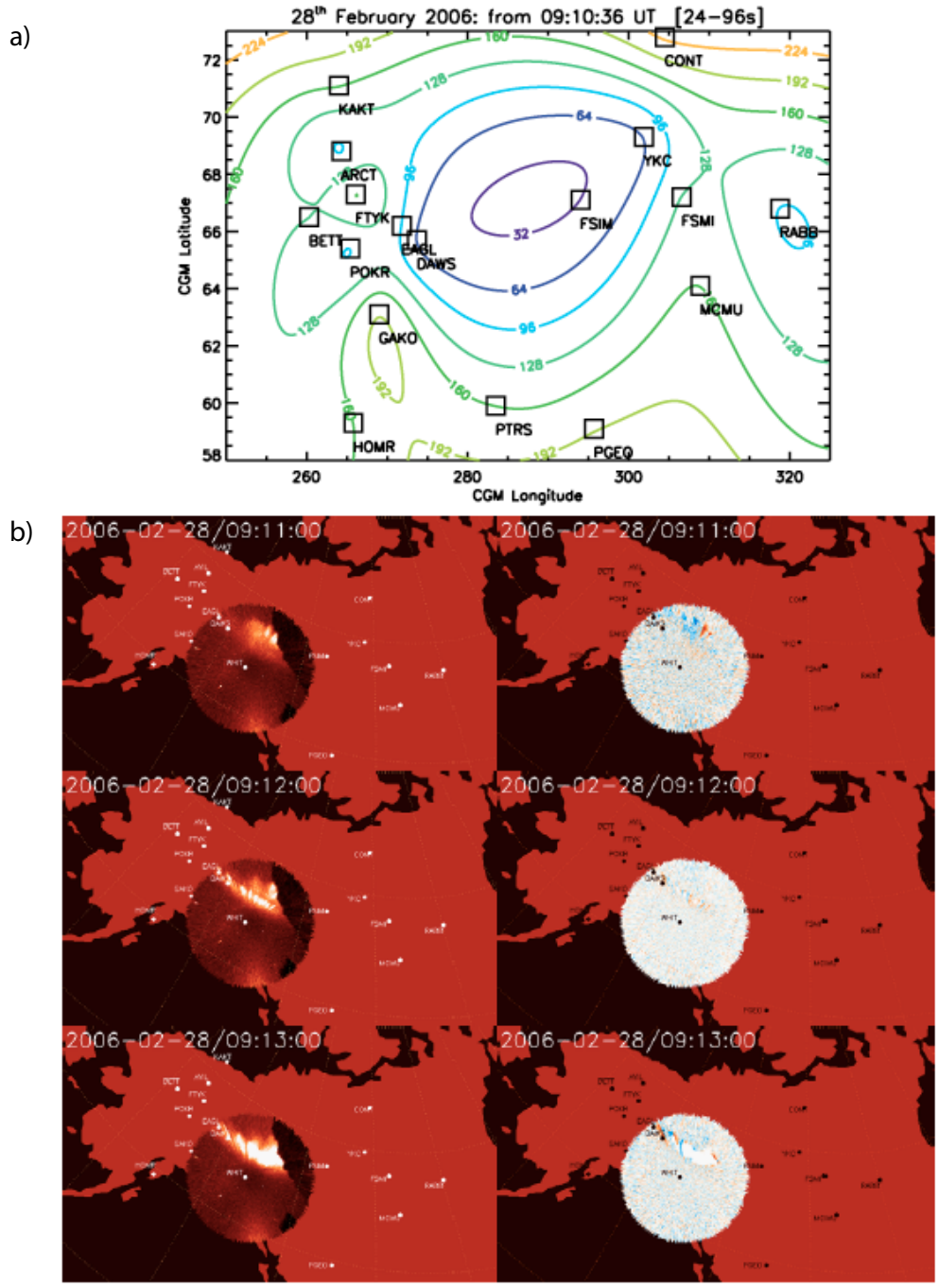

Figure 2.17: (*top*) ULF wave contours every 32 s for substorm on 28 February 2006. (*bottom*) Original THEMIS ASI data (*left*) and temporal difference images (*right*). Figure from *Rae et al.* [2009b].

low frequency oscillations in the magnetic field ('*geomagnetic micropulsations*' after *Jacobs and Sinno* [1960]). Studies have also shown that Pi2 waves (40-150 s period) can be used as an indicator of the location of the SCW [*Lester et al.*, 1983].

By using a wavelet analysis technique on data from ground based magnetometers from the Canadian Array for Realtime Investigations of Magnetic Activity (CARISMA) [*Mann et al.*, 2008] and THEMIS [*Russell et al.*, 2008] arrays, *Milling et al.* [2008] demonstrated that waves in the 12-48 s frequency band were the first to rise above a pre-determined threshold during a substorm onset. The growing waves were first observed at a single magnetometer station, and were subsequently observed at surrounding stations. Hence, the waves were initially localised in the ionosphere, however the onset of waves subsequently expanded away from their epicentre [*Milling et al.*, 2008]. The Automated Wavelet Estimation of Substorm Onset and Magnetic Events (AWESOME) technique was developed by *Murphy et al.* [2009], based on the work by *Milling et al.* [2008], to automate the determination of ULF wave epicentres. An example of such a ULF wave epicentre identified by AWESOME is shown in Figure 2.17*a*, showing a 2D minimum curvature fit to the first onset time of 24-96 period ULF waves reported by *Rae et al.* [2009b]. The onset region of the ULF waves was observed to be near the FSIM magnetometer station (dark blue contours). ULF waves were subsequently observed by the other magnetometers surrounding FSIM (light blue and green contours).

In conjunction with the ULF wave epicentre, *Rae et al.* [2009b] also observed auroral beads in WHIT ASI (located approximately between FSIM and GAKO magnetometer stations) 1-3 minutes prior to auroral breakup, shown in Figure 2.17*b*. The auroral beads were colocated in time and space with the ULF wave epicentre, suggesting that the two signatures are linked. However in the event studied by *Rae et al.* [2009b] there were multiple activations of ULF waves and auroral beads prior to substorm onset. This shows that not all localised magnetic and auroral activations necessarily lead to a substorm onset, and that other processes in the magnetosphere also play a vital role.

It is well documented that auroral intensities start growing exponentially

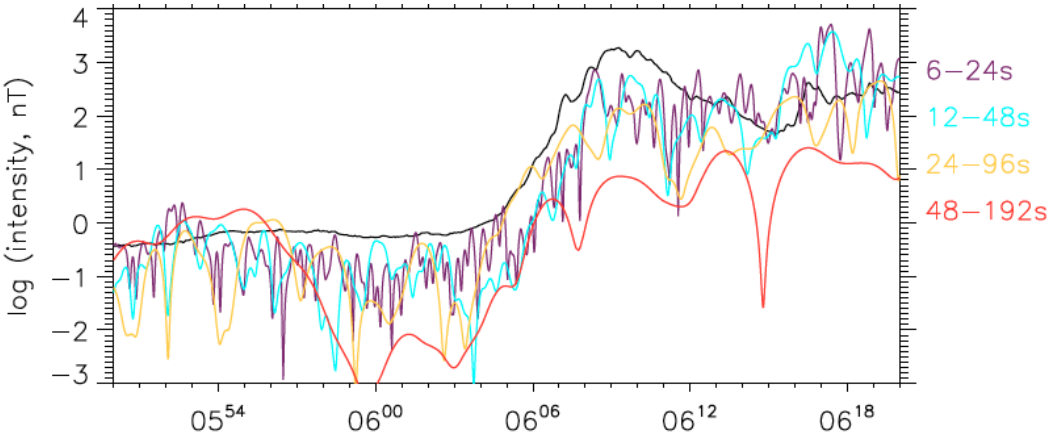

Figure 2.18: ULF wave frequencies in 6-24, 12-48, 24-96 and 48-192 s band on a logarithmic scale, together with the GILL ASI intensity (black). Figure taken from *Rae et al.* [2012].

at substorm onset, e.g., *Henderson* [2009]. *Rae et al.* [2011] showed in a superposed epoch analysis that ULF waves also exhibit exponential growth in the minutes surrounding substorm onset. So, how is the exponential growth of the aurora related to exponential growth in the ULF waves? A comparison between ULF wave growth and auroral intensity from the conjugate GILL ASI during a substorm is shown in Figure 2.18 [*Rae et al.*, 2012]. ULF wave amplitudes for different frequency bands are shown in colour and follow the same exponential increase as the auroral intensity, suggesting that ULF waves and the aurora are strongly linked, at least during substorm onset. This suggests that the waves, and precipitating particles have the same source.

2.8.2 In-Situ ULF Wave Observations

To confirm that ULF waves originate in space *Rae et al.* [2009a] report ULF waves from magnetometer stations on the ground, auroral beads in the ionosphere and conjugate ULF wave observations by GOES-12 at geosynchronous orbit. The measurements at geosynchronous orbit of the magnetic field component parallel to the Earth's spin axis, and the orientation of the magnetic field, show perturbations and a field rotation within $\sim$ 20 s of ULF wave onset on the ground. This is the first evidence that the ULF wave observed on the ground are linked to a waves in space.

The first attempt to quantitatively link ULF wave observations on the

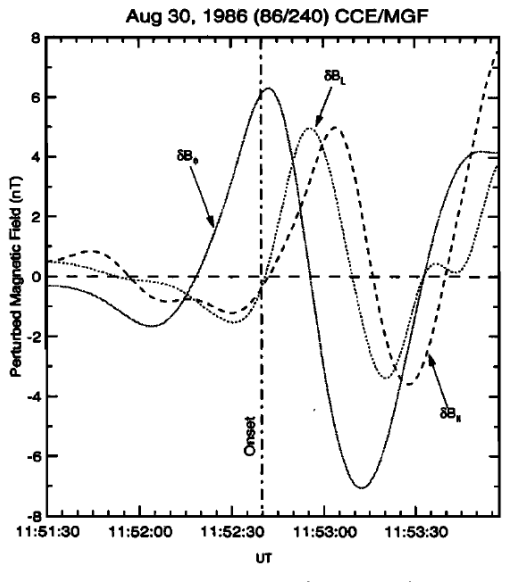

Figure 2.19: Three components of low frequency magnetic field perturbations prior to current disruption. Figure taken from *Cheng and Lui* [1998].

ground with ULF wave observations in near-Earth space was performed by [*Walsh et al.*, 2010], by extending the AWESOME algorithm [*Murphy et al.*, 2009] to detect ULF wave onset from spacecraft data. During a substorm on 1 October 2005 *Walsh et al.* [2010] show ULF wave growth observed by ground magnetometer and GOES-12 and Double Star TC-2 satellites located within the substorm current wedge. ULF wave onset was first observed on the ground, followed by ULF wave onset observed by the Double Star and GOES satellites in space around 4 minutes later. If a localised instability in the near-Earth plasma sheet is responsible for the growth of ULF waves during substorm onset, then it is possible that the spacecraft were slightly earthward of the current disruption region at the time of current disruption. This is consistent with observation the dipolarisation of the magnetic field several minutes later. Hence, the later observations of ULF waves in space can be attributed to a spatial effect as the spacecraft were not in the CD region at the start of the substorm.

Low frequency perturbations associated with substorm onset have also been observed at locations other than geosynchronous orbit of the magnetotail. *Cheng and Lui* [1998] report a low frequency perturbation in the magnetic field observed by AMPTE/CCE at 23.5 MLT at a radial distance of

$8R_E$ starting $\sim$ 1.5 minutes prior to substorm onset. Figure 2.19 shows the three components of the magnetic field perturbation, before which almost no magnetic field fluctuations were observed. The relative phases of the three magnetic field components are in agreement with the structure expected by a linear ballooning instability. The ion gyroradius was comparable to the perpendicular wavenumber measured, leading to the conclusion that the magnetic field perturbations were caused by a kinetic ballooning instability wave, with wave period 50-75 sec.

Saito et al. [2008] report multiple observations of ballooning mode waves around $10 - 12R_E$ in the magnetotail observed by Geotail prior to magnetic field dipolarisation during a substorm. The waves were identified by wavelet analysis of magnetic field fluctuations, with the dominant magnetic field perturbation in the B_x direction. The wavelengths of the ballooning mode were of the order of the ion Larmor radius, and the waves were observed during high plasma beta conditions, $\beta > 20$.

In summary, not only has ULF wave growth as measured from the ground been inextricably linked with the exponential growth of total auroral intensity at substorm onset, and observations of auroral beads, these observations have also been linked to space. There have been multiple observations of ULF wave growth in different regions of the magnetotail associated with substorm onset, showing that the ULF wave perturbations measured on the ground are likely to be a direct consequence of the substorm instability, and play an important part in the processes eventually leading to substorm onset.

2.9 Thesis Summary

As we have seen, there are multiple ionospheric and magnetospheric disturbances, which altogether constitute a substorm. However the various substorm models, and in particular the sequence of events leading to substorm onset remain hotly debated. It is widely agreed that the instability in the near-Earth magnetosphere results in the disruption and diversion of the cross-tail current into the ionosphere, where the bright substorm aurora are observed,

whereas the location where the instability is initiated, whether locally in the near-Earth plasma sheet, or remotely by flow bursts initiated by NENL reconnection is not. This process of current disruption is accompanied by wave-like fluctuations in the aurora (auroral beads), ULF waves observed using ground magnetometers, and infrequent observations of ULF waves in space.

In this thesis detailed analysis of auroral beads is performed to narrow down the substorm instability leading to the current disruption process. This is preferable to in-situ studies of ULF waves, as the THEMIS ASI array, allows waves to be studied with global coverage and at high spatial and temporal resolution. By understanding the signatures and associated physics of substorm onset on the ground, we can extrapolate this information by using conjugate ground- and space-based observations in the future to solve the half-century-old substorm debate and improve understanding of fundamental magnetospheric dynamics.

Chapter 3

Instrumentation and Methods

As we have already seen in previous chapters, the magnetospheric processes leading to the substorm, result in the deposition of $\sim 10^{15}$ J of energy in the form of auroral particle precipitation into the ionosphere over approximately 5 hours [*Østgaard et al.*, 2002]. This can be observed in the bright and dynamic substorm aurora, as was first recognised by *Akasofu* [1964]. Observations of the substorm aurora from space and the ground have since uncovered further detail of the auroral substorm sequence. As we saw in Section 1.4.3, magnetosphere dynamics can result in field-aligned currents into the ionosphere, providing an auroral counterpart to processes happening in space. In this thesis we explore ground-based auroral datasets and novel analysis techniques to uncover the physical magnetospheric processes in the minutes prior to substorm onset in unprecedented detail. In Chapters 4 and 5 we present statistical analysis of auroral data obtained from the THEMIS All-Sky Imagers between 2006-2014 (see Section 3.1). In Chapter 6 we present a case study of an auroral substorm observed using the MOOSE imagers at Poker Flat (see Section 3.2).

3.1 THEMIS All-Sky Imagers

The Time History of Events and Macroscale Interactions during Substorms (THEMIS) mission [*Angelopoulos*, 2008; *Sibeck and Angelopoulos*, 2008] consists of five magnetospheric satellites, launched in 2007, in highly elliptical orbits in the equatorial plane and originally ~ 20 ground-based All-Sky Im-

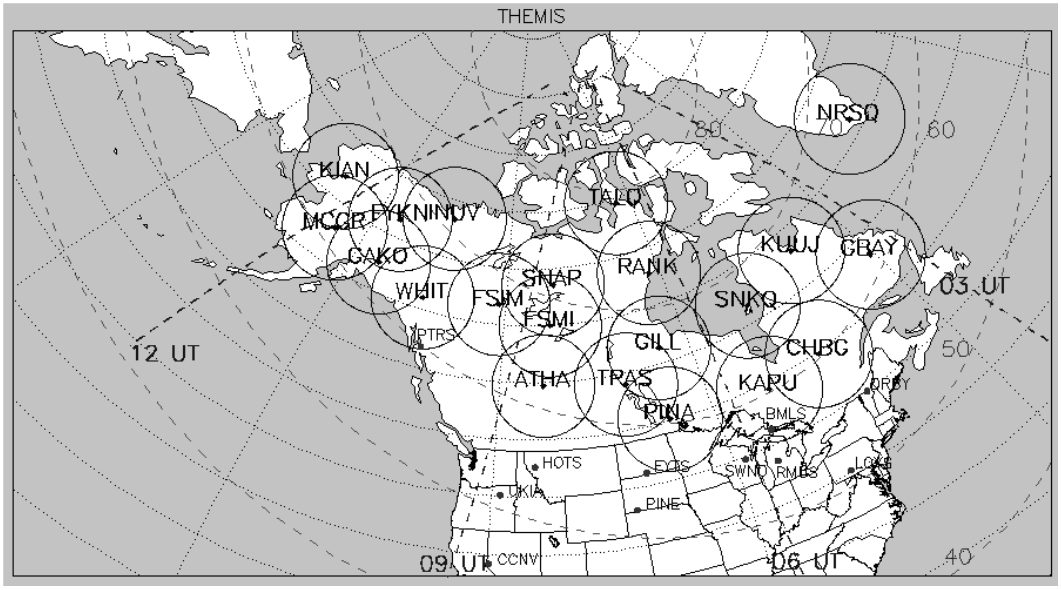

Figure 3.1: Map of North America with the All-Sky Imager's location and field-of view project to 110 km altitude. Lines of constant magnetic latitude are indicated by the dashed lines, and meridians of local magnetic midnight for a selection of UTs is also shown. The figure is valid from January 2009 - present and was taken from *http://themis.ssl.berkeley.edu/gbo/display.py*.

agers (ASIs *Mende et al.*, 2008) positioned in Northern Canada and Alaska (see Figure 3.1). The aim of the THEMIS mission is to uncover the causal sequence of events leading to substorm onset (e.g., reconnection, current disruption), including the macroscale plasma instability in the magnetosphere, and the location of auroral breakup when mapped to the magnetosphere.

The ASI array provides coverage extending over 8 hours of local time of the night-side magnetosphere as well as higher spatial and temporal resolution data than previous polar-orbiting spacecraft, such as the Imager for Magnetopause-to-Aurora Global Exploration (IMAGE) satellite [*Burch*, 2000], could provide. This elevated resolution, together with extended coverage of the ASI array allows auroral and magnetospheric processes to be investigated, without relying on point-measurements provided by few satellites in the vast volume of the magnetotail.

The ASIs consist of a combination of off-the-shelf white-light Starlight Express CCD cameras, mass produced fish-eye lenses, and purpose-built optics, providing scientific instruments at a low cost. The schematic cross-section of a THEMIS ASI is shown in Figure 3.2 and includes: a sunshade to protect the

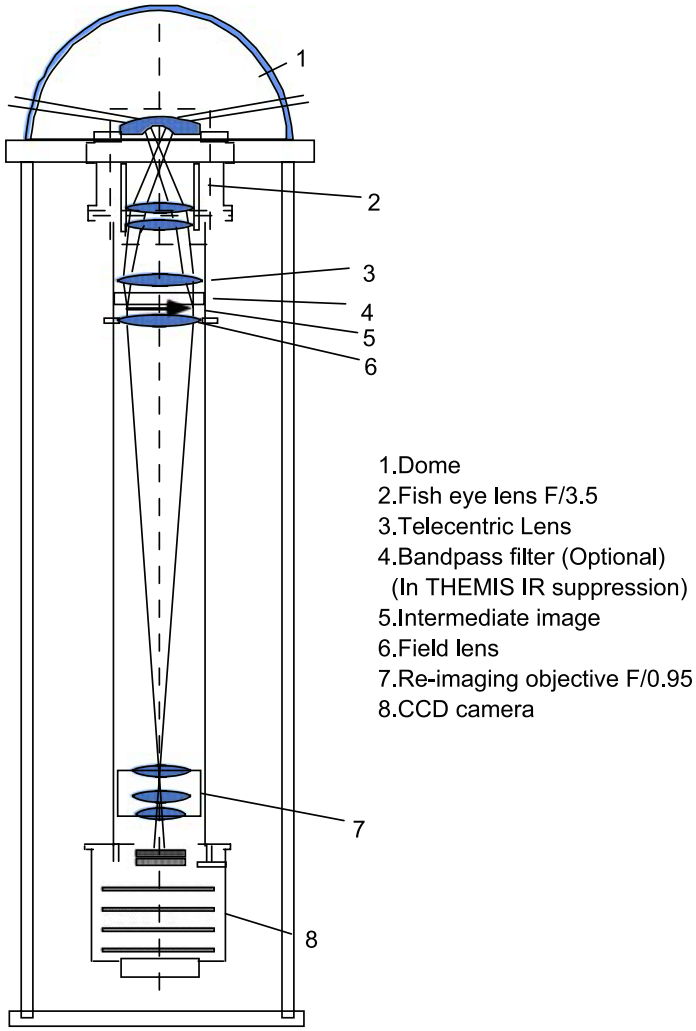

Figure 3.2: Schematic cross-section of a THEMIS All-Sky Imager. Figure taken from [*Mende et al.*, 2008].

instrument from direct sunlight (1), multiple lenses (e.g., 3, 6, 7), including a fish-eye lens (2) to observe the full sky, and the CCD sensor (8).

No spectral filters are required as the ASIs are white-light imagers. This means that image intensification is not necessary as the signal from the aurora is bright enough. Not using a spectral filter also allows numerous stars to be resolved, which are used for geometric and cross-imager intensity calibration. Modelling for this type of camera shows that the imager primarily responds to electron precipitation energies greater than 3 keV [*Mende et al.*, 2008]. This approximately corresponds to the 557.7 nm green auroral emission line.

The camera generates 752×580 pixel images which are binned (2×2)

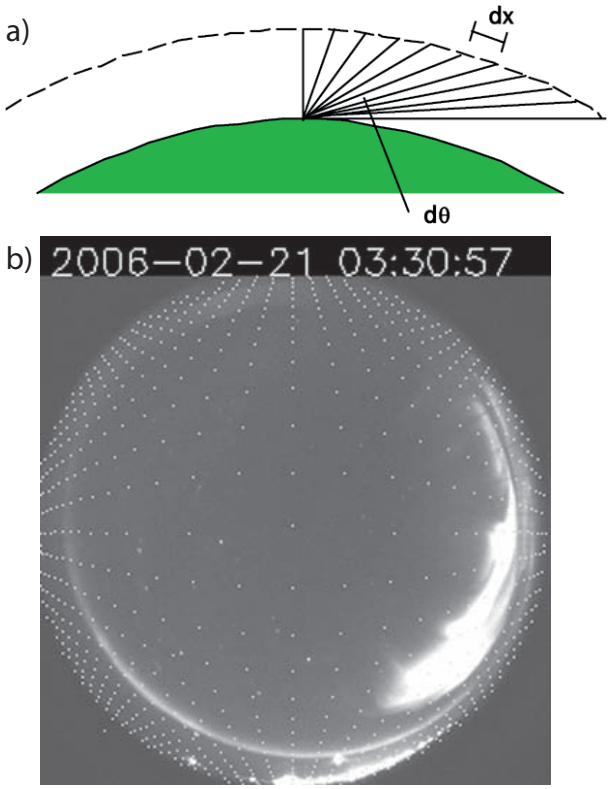

Figure 3.3: The distortion of the all-sky imager field-of-view due to the use of a fish-eye lens. (*a*) The cross-sectional field-of-view of an imager, which shows that an equal distance at auroral latitudes dx, corresponds to smaller angles $d\theta$ and this reducing the resolution at the edges. (*b*) uniform boxes of 30 km size over-plotted, to show fewer pixels correspond to the same amount of sky at the edge of the field of view [*Mende et al.*, 2008].

and cropped slightly, resulting in 256×256 image data products. At zenith, this corresponds to $\sim$ 1 km resolution, assuming 110 km emission altitude. A 1 s exposure time is used and, together with binning, cropping and data compression, the total time needed to generate one image is $\sim$ 2.5 s. This allows the all the imagers to run at a 3 s cadence (0.33 Hz), with simultaneous image timing across the array synchronised by GPS timing [*Donovan et al.*, 2006].

The fish-eye lens gives the cameras an approximate 160° panoramic view, corresponding to roughly 4.5 degrees of coverage in latitude and $16-20$ degrees in longitude, which is greater than 1 hour in local time per imager. However the fish-eye lens causes distortion and a reduces resolution at the edges of the centre of the field of view. This is illustrated in Figure 3.3*a*. An equal distance of sky, dx, corresponds to a smaller angular distance, $d\theta$, near the

horizon. This means that fewer pixels at the edge of the field of view cover the same distance in the ionosphere. Figure 3.3*b* shows an equally spaced 30 km grid over-plotted on the ASI field of view, which also demonstrates the reduced spatial resolution at the edge of the image.

For the studies presented in Chapters 4 and 5, we use data from the THEMIS ASIs.

3.2 MOOSE Auroral Imagers

The Multi-spectral Observatory Of Sensitive EM-CCDs (MOOSE) consists of five Andor Ixon DU-888 imagers with telecentric optics designed by Keo Scientifiic and funded by the National Science Foundation (*http://moose.space.swri.edu*). The MOOSE imagers are generally co-located at Poker Flat, Alaska, however depending on specific rocket or auroral campaigns they can be moved to different locations and set-up in a variety of configurations. The location of Poker Flat is 190 km South-West of Fort Yukon, a THEMIS ASI station, allowing the MOOSE ASIs to improve the Western edge of the THEMIS ASI array coverage. In comparison to THEMIS, MOOSE provides data at much higher cadence ($\times 10$) and enhanced spatial resolution ($\times 2$). Spectral filters are used to provide multi-spectral information allowing specific events to be studied in more detail than is possible using solely THEMIS ASI data.

For the study presented in Chapter 6, four of the MOOSE imagers were positioned at Poker Flat, Alaska, with the following filters and lenses:

- Three All-Sky lens modules (180° FOV), providing 512×512 pixel images at 3.3 Hz frame rate with filters to show the following auroral emissions:
  - Green at 557.7 nm
  - Red at 630.0 nm
  - Blue at 427.8 nm
- One narrow-field 210 mm lens module (19° FOV) providing 190×190 pixel images at a 40.7 Hz frame rate with a broadband Schott BG3 filter

which selects only prompt emissions [*Samara et al.*, 2012; *Michell et al.*, 2012]

At zenith the all-sky imagers have a spatial resolution of $\sim$ 500 m per pixel, assuming an emission altitude of 110 km, which is a reasonable estimate for the green-line emission. The narrow-field imager has a resolution of $\sim$ 126 m per pixel, assuming 100 km emission altitude, in comparision to the $\sim$ 1 km resolution of the THEMIS ASIs at zenith.

3.2.1 Calibration of the MOOSE Imagers

The multi-spectral MOOSE imagers at Poker Flat Alaska measure the intensities of the green-, red- and blue-line aurora. In order to make direct comparisons between the emission intensities in the different auroral spectra, and hence infer information about the auroral acceleration processes, the imagers must be cross-calibrated. The calibration of the data presented in Chapter 6 of this thesis were performed by *G. Grubbs* [*personal communication*], and are briefly described in the following section. Further information on the calibration techniques used can be found in *Grubbs* [2016]; *Grubbs et al.* [2016].

1. **Bias and Dark Subtraction**

   A '*dark current*' is a source for noise in a CCD detector. If the detector is not cooled sufficiently, thermal electrons can overcome the voltage across the CCD, creating a current, even when there are no photons incident on the detector. A structure in dark frames was noticed by *Hirsch et al.* [2013], showing that dark frame values can be estimated if the dark/bias signal level for at least one pixel in each row and column are known. In auroral imagers with a fish-eye lens, the dark border around the images (Figure 3.4*a*) can be used to estimate the dark/bias counts for the whole frame. The calculated dark Frame is shown in Figure 3.4*b* and accounts for approximately 10% of the raw counts at each pixel.

2. **Flat-Fielding**

   Flat-fielding is used to reduce systematic spatial non-uniformities of an imager. The response of the imager is measured using an image from

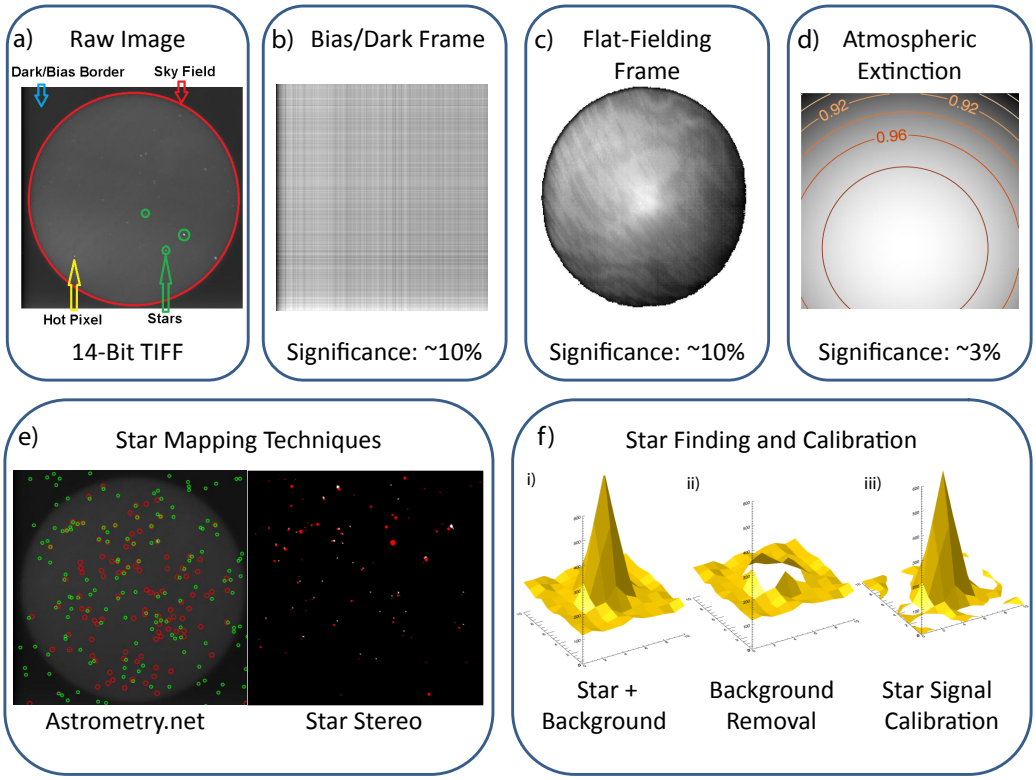

Figure 3.4: An overview of the calibration processes used to calibrate the imagers with all-sky lenses and spectral filters used in Chapter 6 [*Grubbs*, 2016].

when the camera is uniformly illuminated, i.e., during a fully dark sky. The dark sky provides uniform luminosity allowing variations in the detectors response to be measured. Aurora and clouds are avoided at this time as these create non-uniformities in the image. A full hour of data is used to remove the effects from stars, as they change location during the hour. The results from flat-fielding are shown in Figure 3.4*c* and account for approximately 10% of the raw counts per pixel.

3. **Star Mapping**

   Freely-available software packages Astrometry.net and Star Stereo are used, together with auroral images, to map the night sky using the stars, as shown in Figure 3.4*e*. A database of known star locations is compared with the stars in the image. This allows the observations of stars to be compared with the Smithsonian Astrophysical Observatory Star Catalog which contains apparent visual magnitudes and spectral types [*Whipple*, 1966]. These known star properties are then used to calibrate

the imagers:

4. **Star Calibration**

   The measured and theoretical calculations of the stars in the field of view of the imager are then used to estimate the imagers' and filters' response.

   (a) **Theoretical Photon Flux Calculation**

   By knowing the spectral type of a star, an estimate can be made of the the surface temperature. The spectral radiance of a black body, an opaque and non-reflective object, at a known temperature T and wavelength λ can be described by Planck's law:

$$B_\lambda(\lambda, T) = \frac{2hc^5}{\lambda^5} \frac{1}{e^{\frac{hc}{\lambda k_B T}} - 1} \tag{3.1}$$

   where B_λ is the spectral radiance emitted by the black body per unit wavelength, k_B is the Boltzmann constant, h the Planck constant and c the speed of light. This can be used to estimate the apparent brightness of the star at Earth assuming no atmospheric effects at specific wavelengths [*Zombeck*, 2006].

   However in reality the Earth's atmosphere will also influence the brightness and appearance of the star. Atmospheric effects which scatter the photons from the star are accounted for using an empirically derived equation for atmospheric extinction [*Kasten*, 1965], which accounts for approximately 3% of the raw counts and is shown in Figure 3.4*d*.

   The combination of the calculated photon flux, taking into account atmospheric effects at Earth, give an approximation of the expected photon flux measurement for each star, at the different spectral wavelengths. This is compared with the values measured by the camera.

   (b) **Measured Photon Flux Calculation**

   Finally the measured photon flux is found using the star mapping and a peak detection algorithm to find the imager's response to the

stars. The stars are detected, Figure 3.4*f*(i), and a median background is removed, Figure 3.4*f*(ii). The resulting signal for the star, Figure 3.4*f*(iii), is then compared with the theoretical calculation of predicted photon flux in order to find the calibration factor for each imager and filter. This allows the raw counts measured by the detector to be converted to Rayleighs.

The calibrated data allows for direct comparisons between different imagers and filters, and provides the input required in order to estimate precipitating electron energy.

3.2.2 The Global Airglow Model

The data of the different auroral emission lines provided by the MOOSE imagers allow an approximation of the characteristic precipitating electron energy to be made using an electron transport model [*G. Grubbs, personal communication*]. In order to use auroral data as input for the model, the output from the imagers need to be processed to provide in order to convert the raw counts per pixel into Rayleighs. This is achieved by the image processing techniques outlined in Section 3.2.1 and shown in Figure 3.4. Further information of the modelling technique used to estimate the characteristic precipitating electron energies during the event presented in Chapter 6 of this thesis can be found in *Grubbs* [2016]; *Grubbs et al.* [2016].

The GLobal AirglOW (GLOW) v.97 model [*Solomon*, 1989, 2001] is an electron transport model which simulates the precipitating electron distributions. This is achieved by solving the Boltzmann electron transport equation by simulating electron motion along magnetic field lines in the ionosphere [*Nagy and Banks*, 1970; *Banks et al.*, 1974; *Solomon et al.*, 1988]. The GLOW model calculates field-aligned upward and downward electron fluxes as a function of energy and altitude, allowing the emission rates for 427.8 nm, 557.7 nm, 844.6 nm and 630.0 nm auroral emissions to be calculated [*Kaeppler et al.*, 2015]. Figure 3.5 shows the predictions made by GLOW for the 427.8 nm, 844.6 nm and 557.7 nm auroral intensity as shown in *Grubbs* [2016].

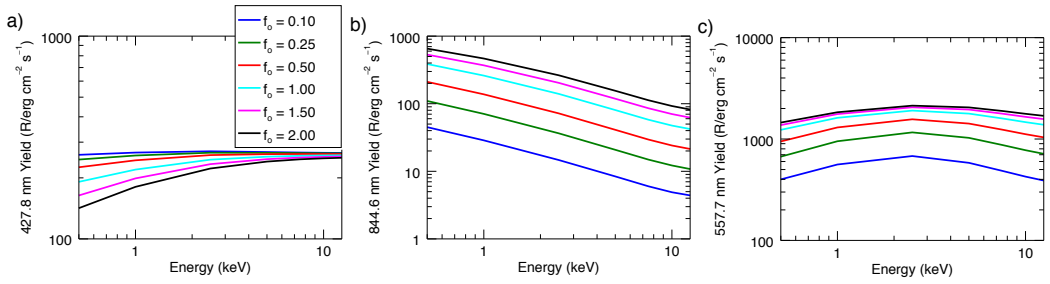

Figure 3.5: Predictions for auroral intensity as a function of characteristic electron precipitation energy for (a) 427.8 nm, (b) 844.6 nm and (c) 557.7 nm from the GLOW model for a range of values for the atmospheric constant, f_0 [*Grubbs*, 2016].

An inversion technique was developed by *Grubbs* [2016] to use the GLOW model to predict electron population characteristics when in-situ data is not available using auroral observations from the 557.7 nm, 630.0 nm (or 844.6 nm) and 427.8 nm emission lines, and by assuming a Maxwellian electron distribution (see *Strickland et al.*, 1993). The Maxwellian distribution describes plasma in thermodynamic equilibrium and is given by:

$$f(E) = \frac{Q}{2\pi E_0^3} \times E \times exp^{-E/E_0} \tag{3.2}$$

where Q is the total energy flux, E is energy and E_0 is the characteristic energy of the population [*Meier et al.*, 1989; *Strickland et al.*, 1993].

By varying the values of total energy flux, Q and characteristic energy, E_0, *Grubbs* [2016] generated an inversion map in order to compare the GLOW model with auroral observations, and estimate the most likely electron precipitation energy. An example of an inversion map is shown in Figure 3.6. In the example shown, the intensity ratio between 844.6 nm and 557.7 nm auroral emissions are used to determine the characteristic precipitation energy. The 844.6 nm emission is an Oxygen transition caused by precipitating electrons with energies below 1 keV. Hence, the ratio of 844.6 nm to 557.7 nm estimates the characteristic precipitating energy as the 844.6 nm emission is caused by low energy electrons, and the 557.7 nm emission is caused by high energy electrons. In our study, we use 630.0 nm as an estimate for low energy electrons instead of 844.6 nm. The absolute intensity of the 427.8 nm emission line is used to find the total energy flux, Q, which is based on multiple studies con-

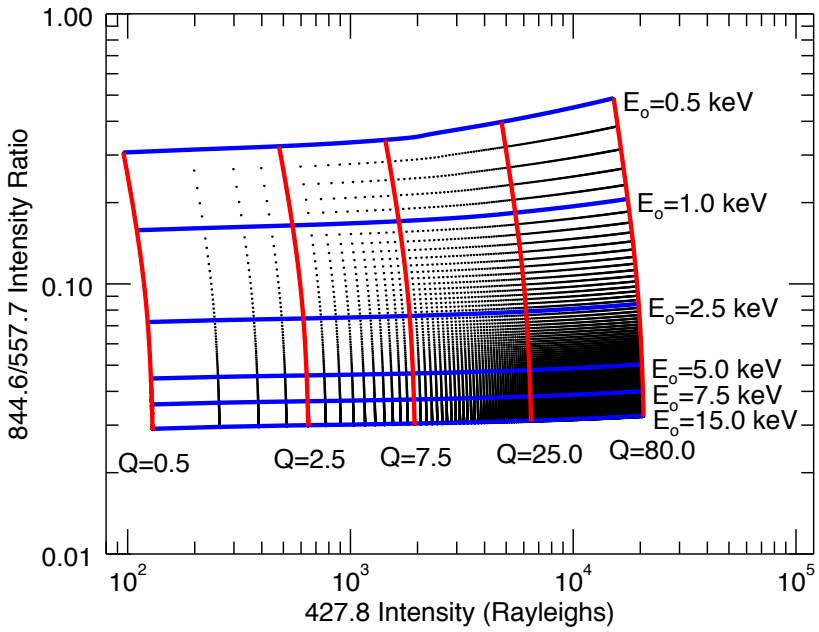

Figure 3.6: GLOW inversion map in order to determine the precipitating electron population characteristics from auroral observations. Figure taken from [*Grubbs*, 2016].

cluding that the production rate of this emission line is 220-270 R/(erg cm^{-2} s^{-1}) e.g., *Rees et al.* [1976]; *Lanchester et al.* [1997]. Auroral data from the different spectral lines are then used to determine the most likely Q and E_0 from the inversion map, to find the electron precipitation characteristics at different regions within the image.

3.3 SuperMAG and the SOPHIE Substorm list

In conjunction with auroral data, we use ground-based magnetometer data to provide more information about magnetospheric dynamics during substorms and an independent, unbiased substorm list. The substorm current system causes deflections in ground-based magnetometer data, particularly in the H-component of the magnetic field.

SuperMAG is the result of a worldwide collaboration of organisations which operate ground-based magnetometers [*Gjerloev*, 2009]. In total, the network consists of over 300 stations. The location of the magnetometers which are part of SuperMAG are shown in Figure 3.7. The data from each magnetometer in the array is re-sampled to a 1 min temporal resolution and

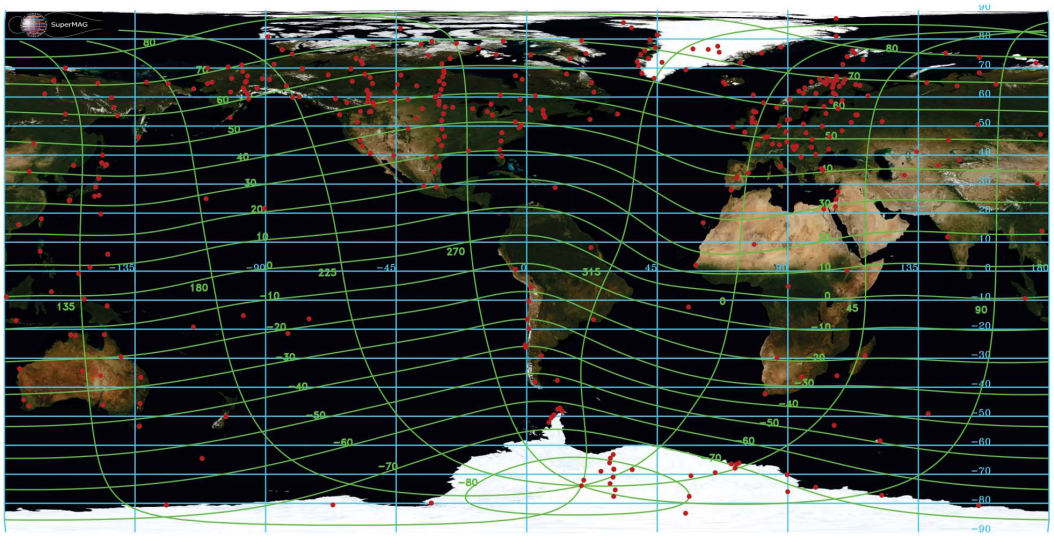

Figure 3.7: Locations of SuperMAG magnetometers shown in red, geomagnetic coordinates in blue and geographic coordinates in green. Figure taken from [*Gjerloev*, 2012].

rotated into a local magnetic coordinate system [*Gjerloev*, 2012]. The North-South component of the magnetic field is affected by current systems such as the ring current, and the ionospheric component of the auroral electrojet.

In order to use magnetometer data to understand magnetic perturbations due to ionospheric and magnetospheric currents a baseline is removed which consists of the Earth's main field and currents in the ionospheric dynamo region [*Gjerloev*, 2012]. The baseline is separated into daily variations, yearly trends and any remaining offset. These are calculated by finding the '*typical value*' of the data on the different timescales, where the typical value is defined as either the mode of the data, or the centre of a Gaussian fitted to the probability distribution. The values for the mode and Gaussian baseline are usually very similar, however the centre of the Gaussian is used if the mode is affected by single point spikes [*Gjerloev*, 2012].

This database of magnetometer data is then used to generate auroral electrojet indices: *SME*, *SMU* and *SML* [*Newell and Gjerloev*, 2011]. Traditionally the Auroral Electrojet Indices are derived by 10-12 geomagnetic stations [*Davis and Sugiura*, 1966] located in the northern auroral zone at $60.0 - 71.0^o$ geomagnetic latitude. However due uneven spacing and large geographic gaps in this array (e.g., over Russia and Europe) substorm activity is not always reflected by these indices, especially if the substorm onset location is not di-

rectly located over one of the magnetometers. The SuperMAG auroral indices differ from the traditional indices mostly due to the number of ground-based magnetic stations used in their calculation, and also by the technique of baseline removal which does not depend on the identification of '*quiet days*'. The SML index value is given by the magnetometer station with the lowest value of the H component of the magnetic field in the network at any given time. By using $\sim$ 300 stations, as opposed to 12, this gives a much more reliable estimate of substorm activity, as there are fewer and smaller gaps.

The Substorm Onsets and Phases from Indices of the Electrojet (SOPHIE) substorm list [*Forsyth et al.*, 2015] determines substorm phase and onset from the SML index on the '*basis of exceedance of a percentile in the rate of change of SML*', without insisting that the recovery phase follows an expansion phase. This removes the need to define an arbitrary threshold below which the data is indicative of a substorm expansion phase. Defining an arbitrary threshold for substorm determination is an unreliable method as substorms typically differ greatly in size, and the uneven latitudinal and longitudinal positioning of the magnetometer stations which contribute to SuperMAG, with the highest density in North America and Europe, biases the detection based on a simple threshold technique towards these local times.

Figure 3.8 shows an example of the phase identification methods and processing using the SOPHIE technique on 10 May 2005 from *Forsyth et al.* [2015]. Figure 3.8*a* shows the input SML. A low-pass filter is applied to the data with a 30 minute cutoff to remove ULF wave effects from the SCW, resulting in an uncertainty in the substorm onset timing of $\pm$15 minutes. Figure 3.8*b* shows the filtered data. Figure 3.8*c* shows the time derivative of the filtered SML, $\frac{dSML}{dt}$. A percentile threshold is chosen (in this case, 75 %), below which the rate of change in SML is defined to be an expansion phase. A corresponding maximum threshold is then calculated in order for there to be a roughly equal number of expansion and recovery phases. These thresholds are indicated by the horizontal lines in Figure 3.8*c*. The intervals which fall below the minimum threshold are labelled as substorm expansion phases, and those which rise above the maximum threshold are labelled as recovery phases. All

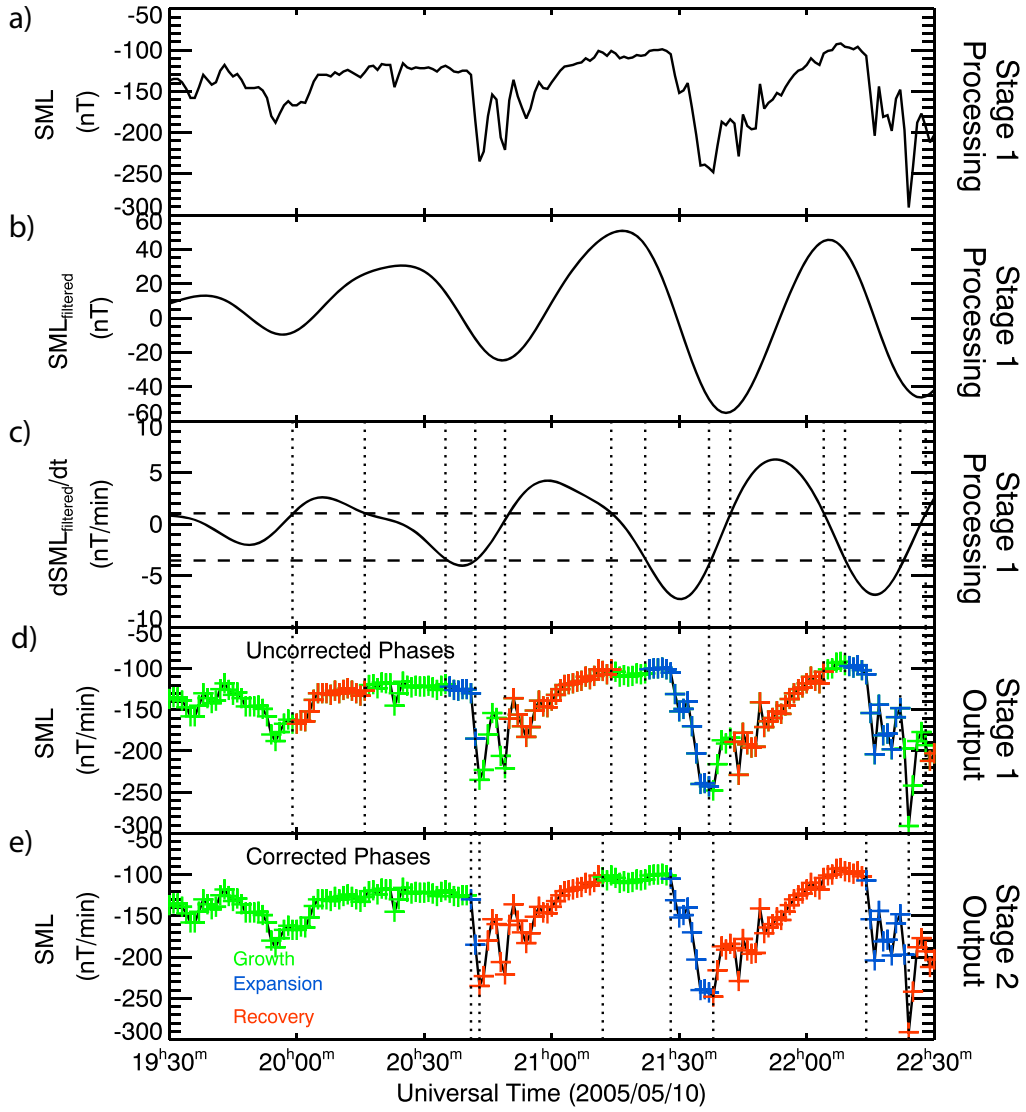

Figure 3.8: An example of the phase identification techniques employed by SOPHIE from the SML index on 10 May 2005. (*a*) The SML input data. (*b*) SML filtered using a 30 minute cutoff low-pass filter. (*c*) The time derivative of the filtered SML data, with the upper and lower percentile thresholds shown by the horizontal lines, and the times the thresholds are exceeded shown by the vertical lines. (*d*) The unfiltered SML data shown with the corresponding growth- (green), expansion- (blue) and recovery- (red) phase. (*e*) The unfiltered SML data shown with the corrected phases. Figure taken from *Forsyth et al.* [2015].

remaining intervals are labelled as a potential growth phases, see Figure 3.8*d*, as there is always coupling between the solar wind and the magnetosphere, except for a purely northward IMF, allowing the solar wind to deposit energy into the magnetosphere, see *Milan et al.* [2012]. However, growth phases which are identified for short periods between expansion and recovery phases, are corrected to be part of either the growth or recovery phase, depending on their relative position to the minimum SML value in the substorm sequence. The corrected phases are shown in Figure 3.8*e*.

During this interval, 3 substorm onsets were identified by SOPHIE, including two intervals which are preceded by a growth phase, and one which is directly after a recovery phase. In the statistical study presented in Chapter 5, we only use isolated substorms which are preceded by a growth phase, and hence only use the substorms at ∼20:40 UT and ∼21:30 UT.

3.4 Fourier Analysis

To uncover the wave-like signatures embedded in auroral arcs, we use Fourier analysis in the spatial domain to identify the characteristic spatial scales present along the substorm onset arc. Fourier analysis allows the determination of the amplitude, power spectral density and wavenumber of auroral beads.

We use a variety of methods (see Chapters 4, 5, and 6) to remove the background auroral arc intensity, allowing us to determine the spatial scales of fluctuations which are otherwise superposed onto a large background intensity (the homogenous auroral arc). The background auroral arc intensity observed by ASIs often also has a large-scale spatial dependence which is due to the location of substorm onset along the auroral arc, cloudy skies, or lunar illumination.

Once the background auroral arc intensity is removed, the characteristic spatial scale (wavenumber) is determined with use of a Fast Fourier Transform (FFT), as first described by *Cooley and Tukey* [1965]. The FFT allows spatial and temporal signals to be decomposed into their constituent frequency com-

ponents. In this thesis we use the FFT as a spatial transform which allows us to determine the wavenumber spectrum which makes up the signal.

The forward FFT is given by Equation 3.3 which transforms a spatial series into the wavenumber domain:

$$F(k) = \mathcal{F}[f(x)] = \frac{1}{N} \sum_{x=0}^{N-1} f(x) e^{-\frac{2\pi i k x}{N}} \tag{3.3}$$

where N is the number of points in the original signal $f(x)$, x is an integer ranging from 0 to $N-1$ and k is the wavenumber (defined below).

The reverse FFT is given by Equation 3.4 which transforms the wavenumber domain back to the spatial domain.

$$f(x) = \mathcal{F}[F(k)] = \sum_{k=0}^{N-1} F(k) e^{\frac{2\pi i k x}{N}} \tag{3.4}$$

The normalisation factor, in this case $1/N$ in Equation 3.3, is a result of convention and can be written on the reverse transform instead, or as $1/\sqrt{N}$ on both the forward and reverse transforms.

The positive wavenumbers, k, are given by:

$$k = \frac{x}{N\Delta x} \times 2\pi \qquad \text{for} \qquad 0 \leq x < N/2 \tag{3.5}$$

where Δx is the spatial resolution of the input signal and the factor of 2π is because $k = 2\pi/\lambda$.

The Nyquist wavenumber, the highest determinable wavenumber, depends on the resolution of the original signal by:

$$k_{Nyquist} = \frac{1}{2\Delta x} \times 2\pi \tag{3.6}$$

Again, where the factor of 2π is because $k = 2\pi/\lambda$.

The resultant amplitude and power of the signal are then given by:

$$A(k) = 2|F(k)| \quad \text{for positive } k \tag{3.7}$$

$$P(k) = 2|F(k)|^2 \quad \text{for positive } k \tag{3.8}$$

The Power Spectral Density (PSD) of a signal is the signal power per unit wavenumber. This is given by:

$$PSD(k) = \frac{1}{\Delta k} P(k) \tag{3.9}$$

where $\Delta k = 2\pi / N\Delta x$

Hence, PSD is similar to the power, however the PSD satisfies Parseval's theorem. Parseval's theorem states that the sum of the integration of the total power spectral density is proportional to the integration of the original signal squared, $f(x)^2$. In this thesis the following definition of Parseval's theorem is used:

$$\sum_{k=0}^{N/2} PSD(k) = \frac{1}{N\Delta x} \sum_{x=0}^{N-1} |f(x)|^2 \tag{3.10}$$

The discrete Fourier transform assumes that the signal is infinite. If a signal is not periodic in the sample interval, the Fourier transform of the signal can have spectral leakage i.e., the smearing of power across multiple wavenumber bins. Spectral leakage is the result of effectively computing the Fourier spectrum of a signal which has discontinuities.

Windowing the dataset is used to smoothly reduce the start and end of a signal to zero, hence removing any discontinuities. As well as reducing spectral leakage, windowing a signal also has some undesirable properties: it widens the spectral line, hence reducing frequency resolution, and it affects the amplitude of the original signal.

For a window, $w(x)$, the correction factor, W is given by:

$$W = \sum_{x=0}^{N} \frac{w(x)^2}{N} \tag{3.11}$$

For a Hanning window [*Press et al.*, 1992], which is the windowing function used in this thesis, the correction factor is $W = 0.3745$.

In order to calculate the original amplitude of the signal, the correction factor is applied to the Fourier spectrum. Hence, in this thesis the following

definitions of power spectral density and amplitude are used:

$$PSD(k) = \frac{1}{\Delta k} \frac{2|F(k)|^2}{W} \tag{3.12}$$

$$A(k) = \frac{2|F(k)|}{\sqrt{W}} \tag{3.13}$$

Chapter 4

Statistical Characterisation of the Growth and Spatial Scales of the Substorm Onset Arc

Rae et al. [2010] showed in a single case study that the formation and evolution of auroral beads along the substorm onset arc is consistent with the linear stage of a magnetospheric instability, by showing that individual spatial scales exhibit exponential growth. *Motoba et al.* [2012] observed auroral beads along the substorm onset arc at magnetically conjugate stations in the northern and southern hemispheres. This conjugacy suggests that the beads have a common driver in the equatorial region of the magnetotail. In this chapter, using data of isolated substorm onset arcs observed by the THEMIS ASIs, we present a detailed analysis of clear visually-identified auroral beading events to uncover whether beads which form along the substorm onset arc are commonly consistent with a plasma instability in the minutes prior to substorm onset. We use Fourier Analysis techniques to investigate the growth and spatial scales of the auroral beads to determine whether an instability is responsible for the beading signature, and infer which instability is most consistent with the observations.

The results presented in this chapter have been published in the *Journal of Geophysical Research* with the citation Kalmoni, N. M. E., I. J. Rae, C. E. J. Watt, K. R. Murphy, C. Forsyth, and C. J. Owen (2015), Statistical

characterization of the growth and spatial scales of the substorm onset arc, *J. Geophys. Res. Space Physics*, 120, 85038516, doi:10.1002/2015JA021470.

4.1 Introduction

4.1.1 The Substorm Controversy

The causal sequence of events leading to energy release and auroral breakup during substorms remains unknown, primarily due to a lack of spatial and temporal resolution when investigating the physical processes occurring within the first 2 minutes of substorm onset in such a vast 3D volume of space [*Ohtani*, 2004]. The discrepancy and uncertainty in timings between magnetospheric processes and auroral signatures prior to the expansion phase has caused a controversial and currently unresolved debate over the physical process leading to the substorm expansion phase onset [*Angelopoulos et al.*, 2008, 2009; *Lui*, 2009]. This debate has predominantly focussed on two substorm onset paradigms: (1) Magnetic reconnection at the Near Earth Neutral Line (NENL) [*Hones*, 1976; *Baker et al.*, 1996] causing Earthward plasma flows which destabilise the central plasma sheet. Further complexity to the NENL model has since been added e.g., *Nishimura et al.* [2010]; *Sergeev et al.* [2012] where the impacts of flow bursts on auroral breakup are discussed; (2) a near-Earth magnetospheric disturbance triggering Current Disruption (CD) in the central plasma sheet [*Roux et al.*, 1991; *Lui et al.*, 1991], resulting in the formation of the SCW and subsequently auroral breakup. Other models include the boundary layer dynamics model [*Rostoker and Eastman*, 1987], near-Earth geophysical onset model [*Maynard et al.*, 1996], and global Alfvénic interaction model [*Song and Lysak*, 2001].

4.1.2 The Auroral Substorm and Auroral Beads

Substorm onset is marked in the ionosphere by a sudden brightening of the most equatorward auroral arc or, in some instances, the formation of a new arc that brightens [*Akasofu*, 1977] and is followed by auroral breakup. Early

observations of substorm aurora provided by the Viking mission [*Anger et al.*, 1987] enabled the discovery of small-scale azimuthal auroral fluctuations, nicknamed 'auroral beads' [*Henderson*, 1994] or subsequently azimuthal auroral forms (after *Elphinstone et al.*, 1995) which form along the onset arc in the minutes leading up to auroral breakup. Auroral beads observed with space-based imagery have only been sporadically reported since [*Henderson*, 2009].

However, the continental-scale spatial coverage provided by THEMIS all-sky imagers (ASI) [*Mende et al.*, 2008] together with their high spatial and temporal resolution has led to the rediscovery of small-scale azimuthal auroral beads forming along the onset arc [*Friedrich et al.*, 2001; *Samson et al.*, 2003; *Liang et al.*, 2008; *Sakaguchi et al.*, 2009; *Rae et al.*, 2009b, 2010]. *Motoba et al.* [2012] observed magnetically conjugate auroral beads in ASI data from both Northern and Southern hemispheres, suggesting that the beads have a common driver originating in the magnetosphere.

In addition to these wave-like signatures in the aurora, simultaneous magnetic pulsations of ULF waves have also been observed in the minutes surrounding substorm onset [*Milling et al.*, 2008; *Murphy et al.*, 2009; *Rae et al.*, 2009a,b; *Mann et al.*, 2008; *Walsh et al.*, 2010; *Rae et al.*, 2011]. Moreover the ULF pulsations are repeatably observed at frequencies similar to those observed in the auroral beads [*Rae et al.*, 2012], suggesting an inextricable link between the auroral and magnetic waves.

The previously discussed studies of auroral beads were limited to descriptions of the initial azimuthal wavelength and it's temporal evolution. In contrast, *Rae et al.* [2010] provide optical analysis of substorm auroral arc azimuthal wavenumber spectra during a single event, which demonstrates that the beading of the substorm onset arc is characteristic of an instability. Together with the magnetically conjugate observations of beads by *Motoba et al.* [2012], this lead to the conclusion that beads are driven by an instability in the near-Earth plasma sheet. *Rae et al.* [2010] report that the frequency, spatial scales and growth rates of the auroral structures are most consistent with either a Cross-Field Current Instability (which predicts growth rates to peak at $\sim 0.27 - 0.4\ \mathrm{s}^{-1}$ depending on the location of the instability in the tail) [*Lui*

et al., 1991; *Lui*, 2004] or a Shear-Flow Ballooning Instability (which predicts growth rates to peak at $\sim$ 0.2 s^{-1}) [*Voronkov et al.*, 1997]. However, *Rae et al.* [2010] could not identify which of these two instabilities acted during this event, nor could they definitively rule out the Kelvin-Helmholtz instability, e.g., [*Yoon et al.*, 1996] or entropy anti diffusion instability, e.g., [*Lee et al.*, 1998] due to unknown magnetotail conditions.

In this chapter we perform a more quantitative optical analysis to that first outlined in *Rae et al.* [2010] over multiple events that display wave-like auroral beads along the substorm onset arc in the minutes leading to substorm onset. By extending the analysis technique outlined in *Rae et al.* [2010] to multiple observations of auroral beads, we are able to determine whether different observations of beads are also indicative of an instability, and if so, whether the same instability is likely to be responsible for all auroral beads studied. Hence, for each substorm and pseudo-breakup event, we characterise the spatial and temporal scales of auroral bead growth and azimuthal propagation. This allows the statistical relationship between wavenumber and growth rate of auroral beads to be found, which we then compare with theoretical predictions of instability characteristics.

4.2 Optical Analysis

An example of a typical isolated substorm onset event used in this study occurs at 04:57:00 UT on 2nd October 2011 (2011-10-02) and is presented in Figure 4.1. This event is characterised by a sudden brightening of the auroral arc at $\sim$04:57:30 UT followed by poleward auroral expansion. Figure 4.1*a-f* shows the raw auroral intensity from the ASI at Gillam (GILL) and the formation and evolution of auroral beads during the event. For the events presented in this study, we visually identify a static region of the ASI which contains the substorm onset arc for as long as possible, which is used for the subsequent analysis. This requires the arc to remain reasonably stationary prior to auroral breakup, with little or no latitudinal motion towards the end of the growth phase. In this particular event, this region is indicated by

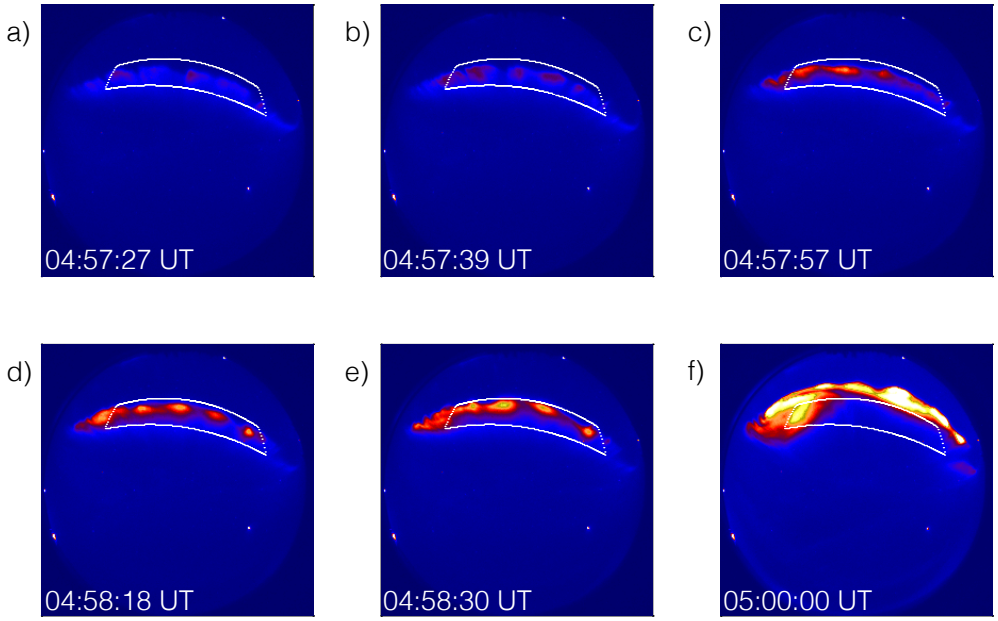

Figure 4.1: Auroral beads along the onset arc during the auroral substorm observed at GILL ASI on 2011-10-02. Lines of geomagnetic latitude at 67.8° and 68.4° and geomagnetic longitude at −33.0° and −24.0° define the field of view of our analysis and show the onset arc is aligned with constant geomagnetic latitude. We track the temporal and spatial evolution of the auroral beads within this box in our subsequent analysis. The formation and evolution of the beads is observed with time. After 04:58:30 UT (*e*) the aurora expands poleward out the box, as can be seen at a later time in (*f*).

the white box in Figure 4.1. Figure 4.1*a* shows the initial visually identifiable formation of bead-like azimuthal structure along the most equatorward auroral arc. Subsequently, the beads brighten and are visible at regular intervals along the auroral arc (Figure 4.1*b*-*d*). In Figure 4.1*e*, the arc brightens further and starts to move poleward and finally, in Figure 4.2*f* the arc shows non-regular structuring (or 'breaks-up') and expands poleward out of the field of view of the analysis box. We limit our analysis to the time interval before the aurora expands outside of the white box. Figure 4.2*a* shows a north-south slice (keogram) which demonstrates the sudden brightening and slight poleward expansion of the aurora indicative of a substorm pseudo-breakup.

4.2.1 Along-Arc Keogram

In general, the substorm onset arc is closely aligned with geomagnetic latitude [*Akasofu*, 1964], a fact we utilise in order to characterise the spatial and tem-

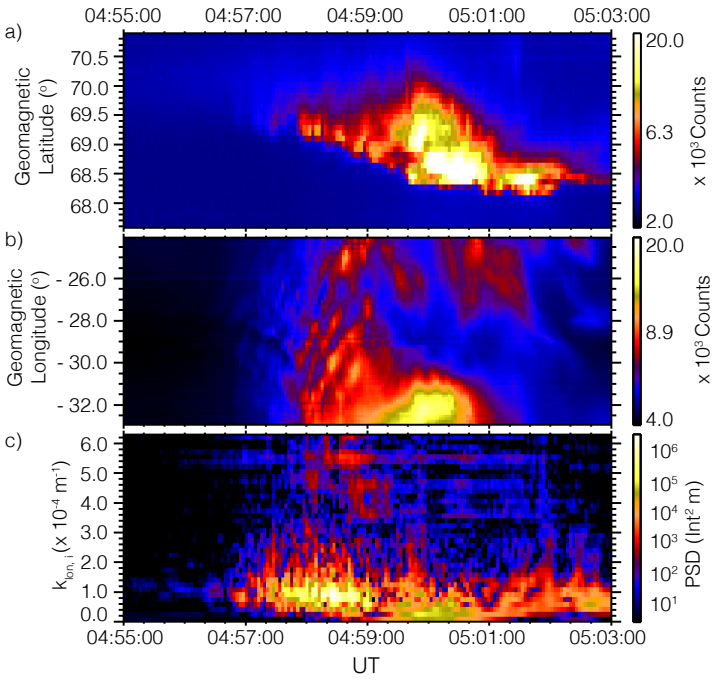

Figure 4.2: A step-by-step demonstration of the optical analysis for a substorm at Gillam on 2011-10-02. (*a*) North-South Keogram to show auroral brightening and poleward propagation. (*b*) East-West Keogram along a line of geomagnetic latitude (as a function of longitude) to track periodic azimuthal structure along the onset arc. (*c*) Power Spectral Density as a function of longitudinal wavenumber measured in the ionosphere, $k_{lon,i}$.

poral behaviour of the auroral bead evolution through substorm onset within our denoted field-of-view. Figures 4.2*b*, *c* demonstrate our analysis as performed on the 2011-10-02 substorm observed at GILL shown in Figure 4.1. Figure 4.2*b* shows auroral intensity within this box as a function of geomagnetic longitude (east-west keogram) along the onset arc. The clear formation of auroral beads along the substorm onset arc are first observed at the same time as the rapid auroral brightening (∼04:57:30 UT in Figure 4.1*a*). The periodic auroral beads initially have a westward phase propagation (to more negative longitudes), but interestingly develop eastward phase propagation (to more positive longitudes) around 20 s later.

4.2.2 Power Spectral Density

In order to calculate the Power Spectral Density (PSD) from the along-arc keogram, the data has to be processed in a number of ways. Firstly background of the auroral arc is removed from the data. Hence, the auroral

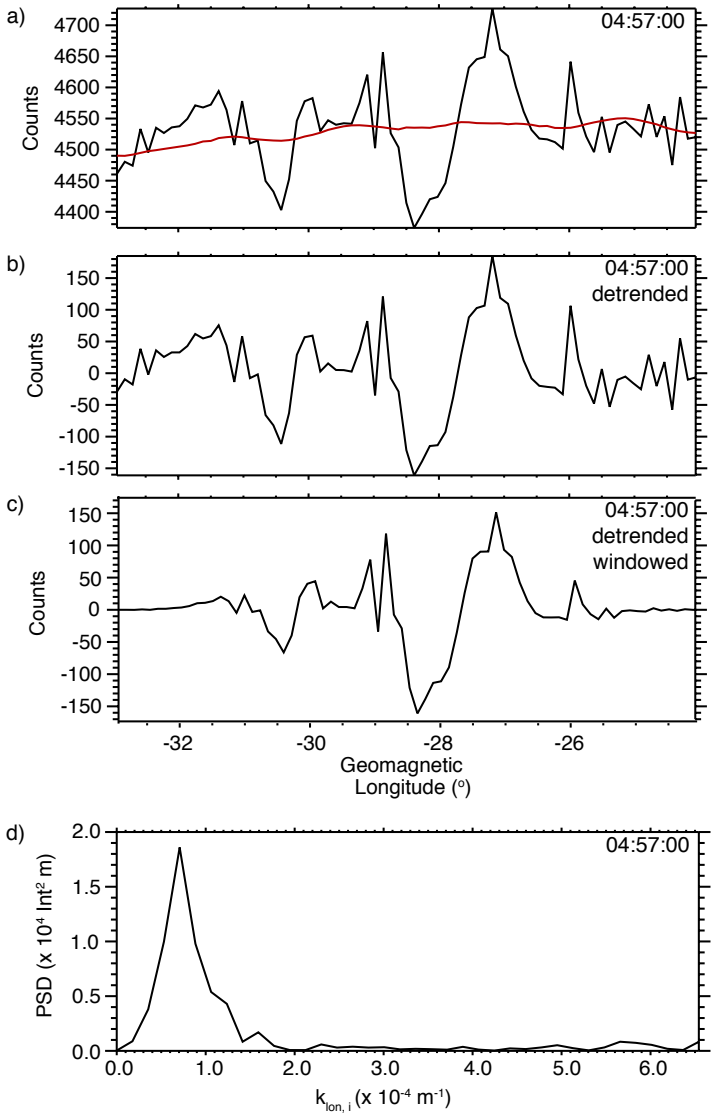

Figure 4.3: Detrending the longitudinal keogram by smoothing. (*a*) Auroral intensity as a function of longitude at 04:57:00 is shown in black. The background intensity from smoothing the series over 5° in longitude is shown in red. (*b*) The detrended data found by subtracting the signal from the background.

signature is detrended, so that we are left with the signature of the beads only. This results in an spatial series of the beads, which is centred around zero, allowing us to perform Fourier analysis on the signal of the beads only, without contamination from the background arc. We detrend the data by smoothing over 5° in longitude. This removes the beading signal, and gives the background arc intensity. Depending on the location where the initial substorm brightening occurs, the background arc intensity can also vary with longitude. This procedure is shown in Figure 4.3*a*, where the original signal (black) and smoothed function (red) are plotted. In order to detrend the data, the smoothed signal is removed from the original signal. The detrended signal is shown in Figure 4.3*b*. This means that the beaded features are centred around the zero axis, removing high powers from the zeroth-wavenumber bin in the Fourier transform. A Hanning window is applied to the detrended data to reduce spectral leakage, as is shown in Figure 4.3*c*. The resulting signal is then Fourier transformed to calculate the PSD. The PSD of the signal at a single point in time, 04:57:00 UT, is shown in Figure 4.3*d*, where a clear peak in PSD can be observed at $k_{lon,i} = 0.7 \times 10^{-4}$ m^{-1}. Figure 4.2*c* shows the temporal evolution of the spatial Fourier transform in the longitudinal direction in order to quantify the spatial periodicity of the auroral beads during this substorm. The dynamic PSD shows that the highest powers are located at $k_{lon} \approx 0.5 - 1.5 \times 10^{-4}$ m^{-1} during the initial beading interval.

4.2.3 Exponential Growth

In order to determine whether auroral beads are a signature of an instability, we determine whether they exhibit exponential growth, as the linear stage of an instability is defined as the duration during which the wave amplitudes grow exponentially in time [*Treumann and Baumjohann*, 1997]. It is visible from Figure 4.2*c* that the PSD grows over a wide range of k_{lon}. Hence, for each k_{lon}, we identify whether this corresponds to exponential growth. An example of an exponentially growing wavenumber ($k_{lon} = 0.9 \times 10^{-4}$ m^{-1}) is shown in Figure 4.4, where we show PSD as a function of time on a logarithmic scale. On a logarithmic scale a period of exponential growth is identified by a linear

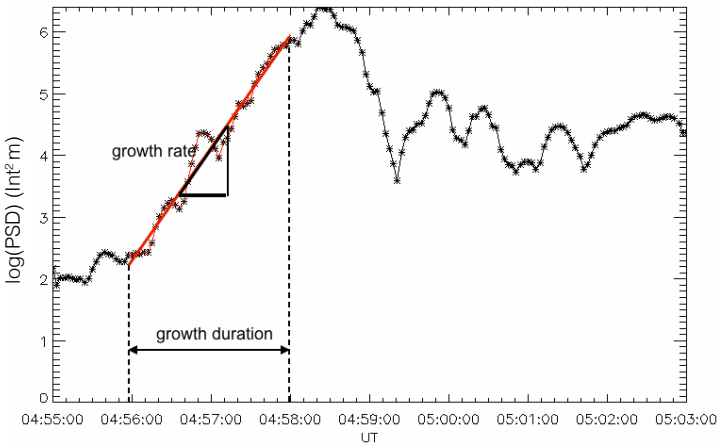

Figure 4.4: Exponential growth rate determination. The log of the power from the power spectral density (Figure 4.2*c*) for a single wavenumber, $k_{lon} = 0.9 \times 10^{-4}$ m^{-1} as a function of time shows the times between which there is exponential growth denoted by the linear fit (red). The growth rate is given by the gradient of the fit.

trend, hence we develop a linear fitting algorithm to detect exponential growth of the power spectral density time series, based upon the least absolute deviations technique. The least absolute deviations linear fitting technique is a robust fitting method which minimises the sum of the absolute vertical residuals by giving equal emphasis to all observations and therefore minimising its sensitivity to large outliers in the data. The algorithm detects the time period of exponential growth by applying a linear fit to a window of the data which systematically varies in size and location. The linear fit with the lowest absolute deviation parameter from the data provides approximate growth duration and start- and end-time (given by the start and end of the linear fit). The linear fit also allows us to determine the growth rate from the gradient of the fit for each k_{lon}. Additionally, the linear fitting algorithm must detect exponential growth:

1. For a duration longer than 30 s, since this is the typical temporal period of an auroral bead fluctuation [*Rae et al.*, 2010],
2. Which occurs before the aurora expand poleward out of the analysis field-of-view,
3. Over at least one order of magnitude in PSD.

If not all the criteria are met, then no growth rate is calculated for that particular wavenumber.

4.2.4 Substorm Onset Window

In order to estimate whether any exponential growth identified by the linear fitting technique is related to the substorm onset process, we define a substorm onset window. This ensures that wavenumbers which start to grow much earlier or much later than substorm onset are not taken into account, as we assume they are not part of the linear evolution of the instability.

We define the onset window start time as the mean exponential growth start time for any wavenumber detected to exhibit exponential growth for at least 30 seconds by the linear fitting algorithm, $\pm 1.5\sigma$, where σ is the standard deviation of the growth start times. The mean exponential growth start time is denoted by the first vertical black line (average start time over all k_{lon} as discussed above) in Figure 4.5*a*. The second vertical black line denotes the time at which the auroral beads expand poleward outside the analysis field-of-view marked in white in Figure 4.1.

In summary, in order for an individual spatial scale to be classified as exhibiting exponential growth, the following criteria need to be satisfied:

1. The exponential growth duration must be continually present over 30 s, since this is the typical temporal period of an auroral bead fluctuation [*Rae et al.*, 2010].
2. The exponential growth duration must occur prior to the auroral arc expanding poleward out of the analysis field-of-view (white box shown in Figure 4.1). The time for this event is shown by the second vertical line in Figure 4.5*a*.
3. The start time of exponential growth must be within the window identified to contain substorm onset, i.e., mean start time $\pm 1.5\sigma$.

Figure 4.5*a* shows the duration for which each individual wavenumber satisfies the above criteria. The duration of exponential growth detected is shown by the coloured bars in Figure 4.5*a*, and the bars are coloured according to the growth rate, gradient of the linear fit, that mode has. Generally, higher spatial scales exhibit slower growth. Figure 4.5*a* also shows that different wavenumbers grow exponentially for a varying length of time. Figure 4.5*b*

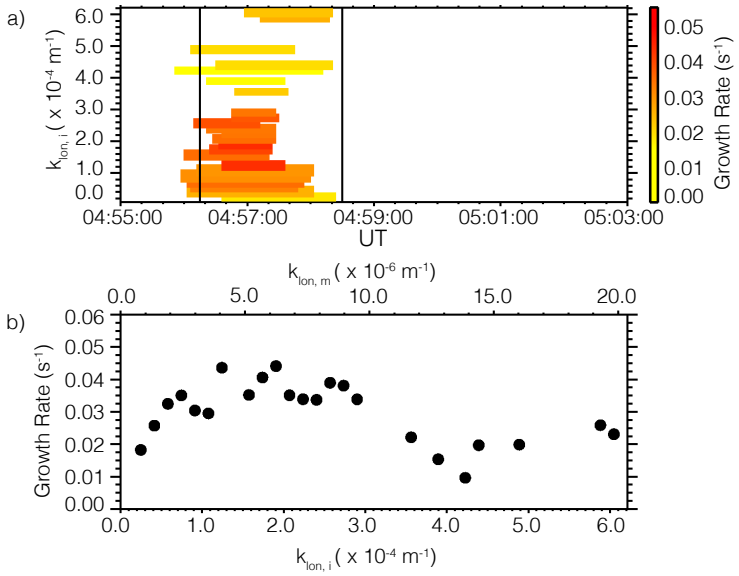

Figure 4.5: Determination of periods which exhibit exponential growth and associated growth rates (a) periods of exponential growth for each $k_{lon,i}$, where the duration of exponential growth is marked by the length of the horizontal line and the growth rate denoted by the colour. The interval encompassing substorm onset is marked by the vertical lines. Only wavenumbers that grow for over 30s and start within 1 standard deviation of the median start time are used and (b) Growth rate as a function of azimuthal wavenumber for those wavenumbers that demonstrate exponential growth according to (a).

shows the calculated growth rates as a function of k_{lon} in the ionosphere ($k_{lon,i}$) and the magnetosphere ($k_{lon,m}$). From this plot we can infer the most unstable wavenumber, which is defined as the wavenumber which exhibits the highest growth rate. The most unstable wavenumber, the range in growth rates, and the wavenumber profile, allow us to compare our observations with plasma instability theory (see Section 4.3) in order to identify which instability agrees with our observations.

4.2.5 Magnetic Field Line Mapping

Magnetic field line mapping allows us to map the auroral bead spatial scales, as measured in the ionosphere, to the magnetotail to determine their magnetospheric scale size. In the ionosphere, the substorm onset arc can form at a variety of geomagnetic latitudes, usually in the range $60^o - 71^o$ [*Frey et al.*, 2004]. When scaled to the equatorial magnetosphere, auroral arcs are mapped depending on their latitude in the ionosphere, and extent of stretching of the magnetic field lines in the tail. In order to estimate the region of

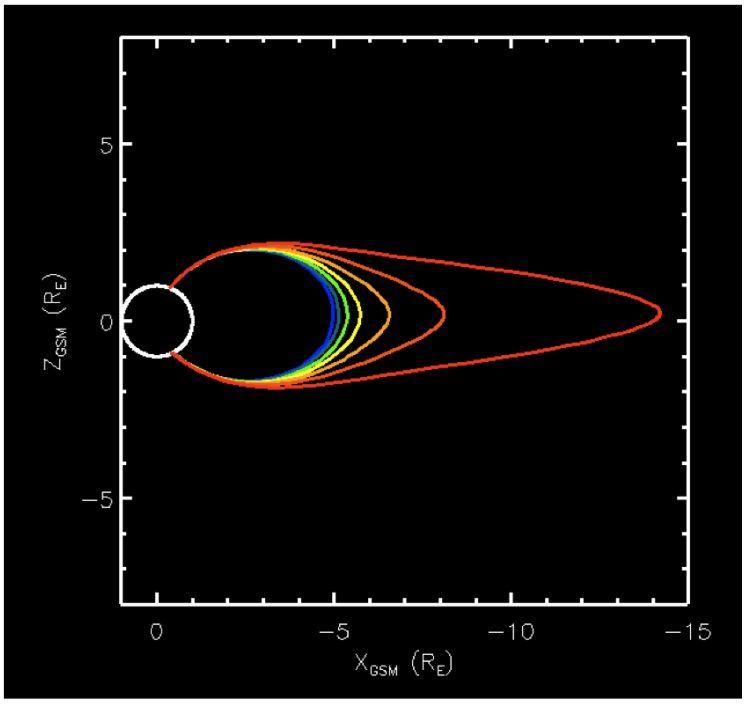

Figure 4.6: Mapping of a field line into the magnetotail in the $x - z$ plane using the T89 model [*Tsyganenko*, 1989] ranging from $K_p = 0$ (blue) to $K_p = 7$ (red). Courtesy of *C. Forsyth*.

the magnetosphere to which auroral arcs map, magnetic field line modelling is used.

Figure 4.6 shows an example of a T89 magnetic field model [*Tsyganenko*, 1989], which depends on the K_p parameter. The magnetic field has a dipolar field at low $K_p = 0$, indicated by blue field line. As K_p is increased up to $K_p = 7$, indicated by the red field line, the magnetic field becomes more stretched. Magnetic field mapping also depends on the ionospheric latitude, with magnetic field lines at lower latitudes mapping closer to Earth than those at higher latitudes.

Magnetospheric field line mapping models are based on a static magnetosphere. At substorm times this assumption does not hold, as the magnetosphere becomes highly dynamic, with a global reconfiguration of the magnetic field topology. This means that field line mapping can only be used as a guideline to measure the extent of magnetotail stretching, which is instructive in this study in order to estimate the magnetospheric wavenumber and remove latitudinal effects from the scaling of the ionospheric wavenumber. At the end

of the substorm growth phase, the magnetotail is significantly stretched due to magnetic flux build up in the magnetotail lobes, this means that field line stretching is likely to be underestimated. In this study we require that events have an undisturbed growth phase, allowing us to assume that any errors in the mapping are systematic. Although this may not provide an accurate estimation of the magnetospheric spatial scales, it allows the direct comparison of events. We use both the T89 [*Tsyganenko*, 1989] and T96 [*Tsyganenko*, 1995] models to map the auroral arcs to the magnetosphere, and conclude that there is negligible difference between the results obtained from either model. We present the results obtained by the T96 magnetic field, which depends upon solar wind dynamic pressure and y_{GSM} and z_{GSM} components of the IMF and the geomagnetic Disturbance Storm-Time index (Dst) [*Tsyganenko*, 1995].

Figure 4.2 demonstrates that although the sudden brightening of the auroral arc can be visually identified at 04:57:30 UT, the analysis of the spectral content of the aurora (Figure 4.5) shows that exponential growth of individual wavenumbers commences around 04:56:15 UT, some 75 seconds earlier. The growth rates peak at 0.045 s^{-1} at longitudinal wavenumbers measured in the ionosphere of $k_{lon,i} = 2.0 \times 10^{-4}$ m^{-1} ($\lambda_i = 30$ km) in this event, or $k_{lon,m} = 6.0 \times 10^{-6}$ m^{-1} ($\lambda_m = 1000$ km $\approx 0.15 R_E$) when mapped into the magnetosphere using a T96 model [*Tsyganenko*, 1995].

4.3 Statistics of Auroral Beads

We use the technique outlined in the Section 4.2 to analyse the growth rates and spatial scales of each of 17 isolated substorm and pseudo-breakup onset arcs, all of which contain visually-identifiable auroral beads which form along a pre-existing arc. Our events are selected from previously published auroral substorms which display clear signatures of beads such as *Liang et al.* [2008]; *Sakaguchi et al.* [2009]; *Rae et al.* [2010], and a list of substorm onset arcs detected by *K. R. Murphy* [*personal communication*]. We choose only events whose longitudes are close to the centre of the field-of-view of the ASIs so that

the beads are generated within the analysis box and remain in the same ASI for the duration of the exponentially growing phase.

Table 4.1 provides our event list and relevant characteristics including magnetic local time (MLT), magnetic latitude and longitude of the arc, direction of bead propagation, and whether the auroral arc brightened and moved polewards (and is thus defined to be a substorm, after *Akasofu*, 1964) or if the arc brightened but did not proceed to poleward expansion and full auroral break-up (pseudo-breakup). These characteristics were all identified from the auroral data only, and analysed in the same manner as the case study presented in Section 4.2. Of particular note is that all 17 wave-like auroral events occurred in the pre-midnight sector. There is no consistent azimuthal phase propagation; the direction of bead propagation varies between eastward (8 events), westward (3 events), both directions (3 events) and non-propagating (3 events), and so there is only a slight preference towards Eastward propagation (i.e., towards midnight in the pre-midnight sector). The magnitude of growth rates measured varies widely between events; maximum growth rates range over an order of magnitude between $0.03-0.3$ s^{-1}, with a median growth rate of 0.05 s^{-1}. However, for each individual event it was usually possible to discern a peak in growth rates at a particular spatial scale. The upper growth rates are not limited by the temporal cadence of the ASI as we require a minimum duration of growth of 30 s, allowing us to observe persistent growth rates above the cadence of our imager if present.

Using global auroral imaging, *Henderson* [2009] estimated the growth rate of 0.005 s^{-1} from the total auroral intensity changes over three consecutive images spanning 4 minutes. *Henderson* [2009] notes that *'as described by Cowley and Artun [1997], the growth could have been associated with an even faster "explosive" instability that leads to a "detonation"'*. *Henderson* [2009] also consider the total auroral intensity observed by the imager to determine their growth rate, including the background homogenous auroral arc (which we remove by detrending the data prior to Fourier analysis), and the sum of the entire range of spatial scales excited by the auroral beads. We propose that averaging over these separate signatures, as well as the lower cadences

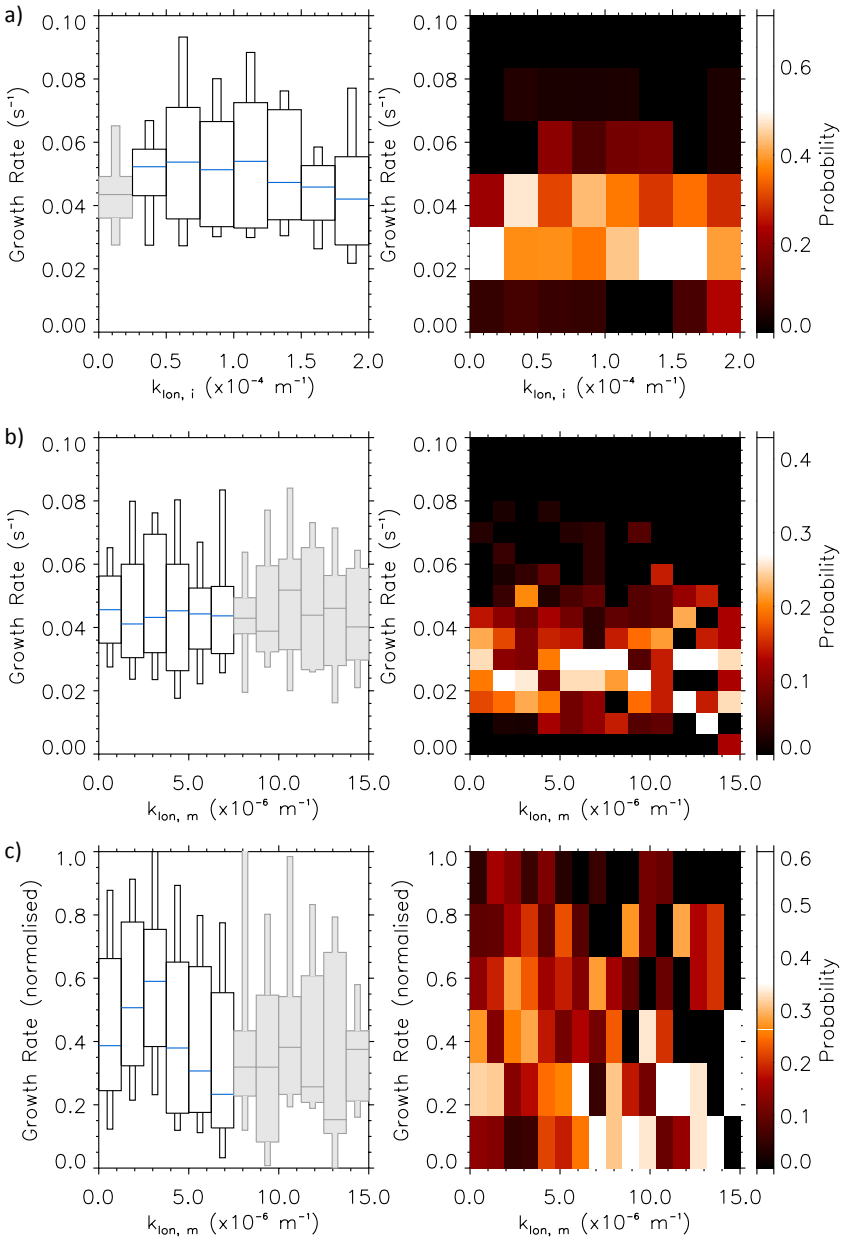

Figure 4.7: (left) A boxplot statistical analysis of growth rate as a function of spatial scale, where medians are denoted by the blue line, the large boxes represent the range of upper and lower quartiles and the smaller boxes represent the upper and lower deciles and (right) Growth rate probability occurrence plot as a function of (a) wavenumber $k_{lon,i}$ measured in the ionosphere, (b) $k_{lon,i}$ mapped to space using T96 magnetic field model, $k_{lon,m}$ and (c) Growth rates normalised to maximum growth rate for each event as a function of $k_{lon,m}$. Subscripts i and m denote ionosphere and magnetosphere respectively.

Date	ASI Station	Time (UT)	MLT	Arc MLAT	Arc MLON	Bead Propagation
28 Mar 2008	GILL	05:36:00	22:26:00	66.2–66.8	−33.0 to −22.0	Eastward
28 Nov 2005	FYKN	10:08:00	22:56:00	64.5–66.0	−100.0 to −90.0	Eastward
27 Jan 2006	FYKN	10:00:00	22:52:00	66.0–67.4	−100.5 to −91.5	None
22 Feb 2006	FSMI	06:26:30	21:32:00	66.4–67.1	−60.0 to −52.0	Westward
28 Feb 2006	WHIT	09:09:30	22:40:00	66.5–67.2	−88.0 to −80.0	Eastward
14 Feb 2007	GILL	05:07:00	22:24:00	64.9–65.8	−35.0 to −20.9	Eastward
7 Mar 2007	SNKQ	05:50:00	23:35:00	64.9–66.1	−15.0 to −5.5	Eastward
2 Oct 2008	SNKQ	04:29:00	22:56:00	66.8–67.15	−8.0 to −2.0	None
3 Jan 2009	GILL	04:36:00	21:18:00	66.7–67.2	−35.0 to −24.0	Westward
24 Feb 2009	FSIM	07:32:00	21:50:00	67.3–67.6	−70.0 to −63.0	None
15 Mar 2009	GILL	04:28:00	21:36:00	67.7–68.2	−30.0 to −20.0	Westward
7 Mar 2010	GILL	05:15:00	22:08:00	64.8 - 66.0	−39.0 to −25.0	Both
31 Dec 2010	FSMI	06:37:00	21:22:00	66.2 - 67.1	−64.0 to −53.0	Eastward
8 Mar 2011	GILL	06:24:00	23:06:00	66.9 - 67.3	−38.0 to −27.0	Eastward
2 Oct 2011	GILL	04:55:00	21:16:00	67.8 - 68.4	−45.0 to −15.0	Eastward
23 Mar 2008	GILL	05:44:00	22:24:00	67.4 - 68.0	−31.0 to −25.0	Eastward
26 Feb 2008	RANK	04:50:00	21:22:00	69.3 - 71.0	−35.0 to −22.0	Both

Table 4.1: Event list from *Kalmoni et al.* [2015]. The substorm and pseudo-breakup event list used in this study, including date, ASI station, substorm time and MLT, onset arc initial magnetic latitude and longitude, bead propagation direction and whether this auroral arc brightened but did not expand polewards (pseudo-breakup) or whether the arc expands poleward and "breaks-up" (substorm), after *Akasofu* [1964].

of the imager, results in a lower growth rate than observed when analysing individual spatial scales. Since our ASI analysis is at a significantly higher temporal resolution and we can resolve individual wavenumbers, we conclude that it is very likely that *Henderson* [2009] has indeed underestimated the growth rates. We discuss the ramifications of this result further below.

Figure 4.7 shows growth rates as a function of k_{lon} in two formats. Figure 4.7 (left) shows box plots of the statistical analysis of growth rate as a function of spatial scale, where median occurrence is highlighted as blue horizontal lines, the large boxes represent the range of upper and lower quartiles ($25th$ - $75th$ percentiles) and the smaller boxes represent the upper and lower deciles ($10th$ - $90th$ percentiles). Figure 4.7 (right) shows the probability occurrence statistics of growth rate as a function of spatial scale to demonstrate how likely a particular growth rate and k_{lon} will be observed.

Figure 4.7a shows statistics of growth rates as a function of ionospheric wavenumber, $k_{lon,i}$, which are calculated assuming an emission height of 110 km altitude. It is evident from both the (left) median and (right) probability distributions that growth rates as a function of ionospheric wavenumber appear relatively flat and the median varies between $0.04 - 0.05$ s^{-1} as a func-

tion of $k_{lon,i}$. The Mann-Whitney U-test [*Mann and Whitney*, 1947] confirmed that the small difference observed in median growth rates is not statistically significant. This means that there is no preferred or more unstable wavenumber than others as deduced solely from ionospheric measurements, and so it is equally likely that statistically a range of spatial scales as measured in the ionosphere exhibit similar growth rates.

However, our hypothesis is that auroral beads are the ionospheric manifestation of a magnetospheric plasma instability, as previously concluded by *Rae et al.* [2010]; *Motoba et al.* [2012]. To investigate the growth and structuring of magnetospheric waves that could be responsible for these ionospheric auroral beads, we map the azimuthal bead structure from the ionosphere into the equatorial plane of the magnetosphere using the T96 [*Tsyganenko*, 1995] magnetic field model, to estimate the spatial scales of the beads depending on the latitude of the arc and stretching of the magnetotail. As substorm mapping is notoriously unreliable during dynamic times, we chose only events that demonstrate steady equatorward motion of the growth phase arc prior to rapid auroral brightening, indicative of a classic substorm growth phase. This will not eliminate errors, however this does allow us to assume that the magnetic field model systematically underestimates substorm auroral bead spatial scales in the magnetosphere. The mapped spatial scales are therefore directly comparable between events even if the absolute value is likely to be lower than its actual magnitude, e.g., *Pulkkinen et al.* [1991]. Using the T96 model to estimate the source location of the auroral arcs, we find that the arcs map to a range of distances between 8-18 R_E in the equatorial plane of the magnetosphere, with the majority lying between 9-12 R_E. Beyond 9 R_E the model predicts magnetic field strengths in the plasma sheet which are < 20 nT.

Using this assumption, Figure 4.7*b* shows the statistics of mapping $k_{lon,i}$ along a T96 magnetic field to estimate $k_{lon,m}$. Again, growth rates appear relatively flat as a function of azimuthal wavenumber, suggesting that there is no preferred wavenumber observed during these events in the magnetosphere either. We propose that the lack of a clear statistical wavenumber versus growth rate profile might be a result of the tail being in differing states during

each substorm creating a continuum of unstable wave numbers; statistically this would result in the flat distribution we observe. However the Mann-Whitney U-test on this distribution suggests that the growth rates in the ranges $k_{lon,m} = 2.5 - 5.0 \times 10^{-6}$ m^{-1} are larger than the others, and that this result is statistically significant to a 95% certainty.

As noted previously, in general there is a well-defined peak in growth rate in individual case studies, but the size of the growth rate varies dramatically from event to event and by over an order of magnitude. Assuming that one specific magnetospheric instability explains the azimuthal auroral beading and auroral substorm onset, it is entirely conceivable that the rate of growth is dependent upon unknown magnetospheric parameters such as plasma density or temperature [*Forsyth et al.*, 2014], or that solar wind driving affects the ionospheric response [*Sergeev et al.*, 2014]. In other words, even though we cannot determine the specific magnetotail characteristics during each substorm, we assume that a single magnetotail instability could explain our results and investigate the implications. It must be noted that our observations demonstrate that only one instability is operating in the first few minutes of auroral beading since the exponential growth of each wavenumber bin exhibits only one well-defined growth rate during this interval. After the aurora expands outside of our analysis domain, any number of additional instabilities may be operating.

We make the assumption that a single instability may excite waves at similar spatial scales to grow at different rates, therefore resulting in the same wavenumber versus growth rate profile, but with different growth rate magnitudes between events. Directly comparing observations, without scaling growth rates could lead to a flat statistical distribution, as observed. Hence in Figure 4.7*c* we normalise the growth rates during each event to the largest growth rate in that event to investigate whether the magnetospheric spatial scales are repeatable across events. Figure 4.7*c* shows a discernible peak in growth rates at $k_{lon,m} \approx 2.5 - 3.75 \times 10^{-6}$ m^{-1} in both occurrence and medians, which corresponds to an azimuthal magnetospheric wavelength of $\lambda_\perp \approx 1700 - 2500$ km (where $\lambda_\perp = 2\pi/k_{lon,m}$). This is comparable to the ion gyroradius for ~ 2 keV ions in a $3 - 4$ nT field ($\rho_i \approx 1600 - 2200$ km) and

therefore provides evidence that the ions may play an important part in the evolution of the instability, however this value is highly dependent on magnetic field strength estimates. The Mann-Whitney U-test confirms that the peak observed in this wavenumber range is statistically significant to a 98% certainty when the growth rates are normalised. We reiterate that the wavelength is likely to be underestimated due to magnetospheric mapping during the substorm growth phase, discussed above [*Pulkkinen et al.*, 1991]. We finally note that using a different empirical magnetic field model such as T89 does not change the result that there is a distinct peak of growth rates with magnetospheric wavenumber, across a similar range.

4.4 Comparison with Candidate Plasma Instabilities

Previous studies of auroral beads suggest that this auroral phenomenon is triggered by a magnetospheric instability, e.g., *Rae et al.* [2010]; *Motoba et al.* [2012]. However, to date there has been no explicit quantitative and statistical comparison of values of the temporal (i.e., growth rates) and spatial (i.e., azimuthal wavenumbers) evolution of the beads in order to compare with instability theory.

Lui [2004] and references therein identified numerous plasma instabilities which may be involved in the initiation of substorm onset. Our observations allow us to rule out several promising plasma instabilities for our substorm events:

- The tearing instability [*Coppi et al.*, 1966] and the drift kink/sausage instability [*Zhu and Winglee*, 1996] have too slow growth rates and a radial wavenumber structuring;
- The current-driven Alfvénic instability [*Perraut et al.*, 2000] and lower-hybrid drift instability [*Yoon et al.*, 1994] predict growth rates and frequencies which are larger by an order of magnitude than those observed.

In a previous study of an isolated event, *Rae et al.* [2010] were unable to rule out the Kelvin-Helmholtz instability which is predicted to have growth rates that peak at low k_{lon} by *Yoon et al.* [1996]. However statistical observations

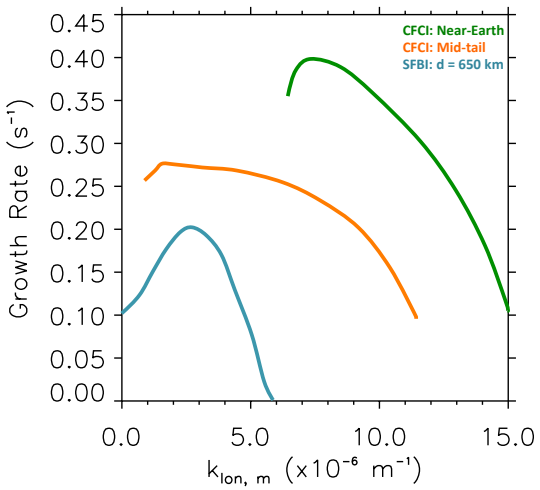

Figure 4.8: The growth rates as a function of wavenumber for the Cross-Field Current Instability, as found by *Lui et al.* [1991], with inner-edge (green) plasma sheet parameters: $V_0 = 0.5v_i$, $T_e = 3$ keV, $T_i = 12$ keV and $n_e = n_i = 0.6$ cm^{-3}, and mid-tail (orange) plasma sheet parameters: $V_0 = v_i$, $T_e = 0.2$ keV, $T_i = 2$ keV and $n_e = n_i = 0.3$ cm^{-3}. The growth rates as a function of wavenumber for the Shear-Flow Ballooning Instability (blue), as found by *Voronkov et al.* [1997], where $\rho = 4.06 \times 10^{-21}$ kg m^{-3}, $B = 40$ nT and shear flow width, $d = 650$ km. The SFBI predicts lower growth rates than the CFCI with a peak at wavenumbers of $k_{lon,m} \approx 3.0 \times 10^{-6}$ m^{-1}.

allow us to rule this out, because the growth rates associated with this instability are over of an order of magnitude greater than the rates we observe [*Hallinan and Davis*, 1970]. The Kelvin-Helmholtz, tearing and Alfvénic instabilities have been ruled out on a combination of the growth rate magnitude and the spatial structuring of the excited waves, meaning that the systematic errors acquired by magnetospheric mapping do not affect this conclusion.

This leaves the Cross-Field Current Instability [*Lui et al.*, 1991; *Lui*, 1996, 2004] and the Ballooning Instability [*Voronkov et al.*, 1997; *Pu et al.*, 1999; *Zhu et al.*, 2004], both of which can explain azimuthal structuring of the onset arc and growth rates consistent with time scales observed. We directly compare Shear-Flow Ballooning Instability [*Voronkov et al.*, 1997] and Cross-Field Current Instability with our observations. Figure 4.8 provides a direct comparison between the growth rates of the CFCI for inner-edge and mid-tail plasma sheet parameters found by *Lui et al.* [1991] and the SFBI found by *Voronkov et al.* [1997].

The challenge with studying the plasma instabilities invoked in substorm

onset is to determine where the instability is initiated in the magnetotail. The Cross-Field Current Instability as outlined in *Lui et al.* [1991] is studied using plasma sheet parameters observed in a statistical study of 15 current disruption events outlined in *Lui et al.* [1992] at radial distances of $7.4 - 8.8$ R_E. As previously stated we estimate that the auroral onset arcs do not map this close to Earth, but to the the region $9 - 12$ R_E more typically associated with the substorm onset initiation. This location is where the field changes from dipole-like to a more stretched tail-like configuration, e.g., *Samson et al.* [1992b]; *Rae et al.* [2014]. Hence, the current disruption events observed from space in *Lui et al.* [1992] may have been initiated at larger radial distances in the tail and propagated Earthward where they were observed. Later, the instability is observed closer to Earth as the substorm current wedge (SCW) expands radially and azimuthally. *Lui et al.* [1991] present growth rates as a function of magnetospheric wavenumber of the Cross-Field Current Instability in the near-Earth and mid-tail plasma sheet. In the near-Earth region the B_z component of the magnetic field is 25 nT. Assuming a T96 field; $B_z = 25$ nT maps to $\sim$ 8.5 R_E in the tail. This agrees with the locations where the instability was observed by *Lui et al.* [1992] and, although slightly closer to the Earth than our magnetic field mapping, implies the substorm onset arc is broadly consistent with the magnetic field magnitudes in the transition region between stretched and dipolar field lines *Samson et al.* [1992b]; *Lui et al.* [1991]. In [*Lui et al.*, 1991], modelling of the CFCI in the the mid-tail region assumes $B_z = 5$ nT, however this maps to $\sim$ 13 R_E in the tail using a T96 field, i.e., significantly further tailward than our events map. There is a similar problem with the Shear-Flow Ballooning Instability (SFBI) as described by *Voronkov et al.* [1997], which does not quantitatively specify a region where the instability is likely to be triggered, but simply states *'the inner edge of the plasma sheet'* where *'magnetic field lines are slightly stretched tail ward'*. The analysis of *Voronkov et al.* [1997] uses a value of $B_z = 40$ nT which, from the T96 model maps to 7.6 R_E in the tail.

The magnetic field properties investigated for both the CFCI [*Lui et al.*, 1991] and the SFBI [*Voronkov et al.*, 1997] map to significantly different regions

than our events map to using a T96 model. The CFCI maps either tailward of our events for mid-tail parameters, or earthward of our events for near-Earth parameters. The SFBI maps significantly Earthward of our events to $7.6\mathrm{R}_E$. Providing that our mapping is also prone to significant errors, it is difficult to establish which instability is more likely based on locations in the tail alone.

When considering the plasma β as a indication for regions of the tail which are more/less likely to be unstable to these instabilities there is similar uncertainty. *Zhu et al.* [2004] find that the ballooning instability is excited for plasma β values in the range of $\sim 1 - 100$. In plasmas with a higher β the high plasma pressure and associated compression stabilises the linear ballooning instability. The plasma parameters given by *Lui et al.* [1991, 1992] give a beta values of $\beta = 4.4$ which lies in this range. However it is unclear how different magnetic field strengths affect the growth rates of this instability. There is a large region of the plasma sheet that satisfy these β values [*Walsh et al.*, 2013], which suggests that a large area of the plasma sheet could be unstable to both the ballooning instability and the CFCI, hence making it difficult to conclude which instability is most likely to result in auroral beads based on plasma β alone.

4.4.1 Cross-Field Current Instability

The Cross-Field Current Instability (CFCI), as its name suggests, obtains its free energy from the cross-field current due to an increase in resistivity in the near-Earth region of the inner plasma sheet when the edge of the plasma sheet moves Earthward during the substorm growth phase. The plasma sheet thins down to a thickness comparable with an ion gyro-radius, allowing the ions to become demagnetised and drift duskward whilst electrons remain frozen to magnetic field lines. The instability takes the form of both an ion Weibel mode (IWI) [*Lui et al.*, 1993] with wavenumbers parallel to the background magnetic field and the modified two-stream instability (MTSI) with wavenumbers perpendicular to the background magnetic field [*Lui et al.*, 1991]. The angle of the waves excited is dependent on the relative ion drift speed. Higher θ (more perpendicular) waves are generated at lower drift velocities (V_0), correspond-

ing to the domination of the MTSI, whereas the more parallel propagating waves (IWI) excited at higher drift velocities have shorter wavenumbers (k). If the IWI mode is suppressed by a thin current sheet, then the MTSI will dominate leading to a more perpendicular wave propagation [*Lui et al.*, 1991], and so the MTSI could explain auroral beading signatures at the end of the substorm growth phase when the plasma sheet is sufficiently thinned.

Lui et al. [1991] investigate the CFCI using parameters representative of the inner-edge and mid tail region of the plasma sheet [*Lui et al.*, 1991, 1992]. *Lui et al.* [1992] choose $V_0 = 0.5v_i$, $n_e = n_i = 0.6$ cm^{-3}, $T_i/T_e = 4$, $T_i = 12$ keV and $B_z = 25$ nT for the inner-edge of the plasma sheet, and $V_0 = 3v_i$, $n_e = n_i = 0.3$ cm^{-3}, $T_i/T_e = 10$, $T_i = 2$ keV and $B_z = 5$ nT for the mid-tail region. Although reasonable parameters, we note that a full analysis of magnetospheric parameters with additional observational constraints from spacecraft data is beyond the scope of this work, but is necessary to definitively rule the CFCI in or out. Figure 4.8 shows the growth rates from both the inner-edge (green) and mid-tail (red) plasma parameters. The growth rates for the inner-edge parameters are higher in comparison to our auroral observations. However a clear peak in growth rates can be observed at $k_{lon} = 7.0 \times 10^{-6}$ m^{-1} ($\lambda = 900$ km). The maximum growth rate for the mid-tail parameters is lower, however the growth rate distribution is almost flat at low wavenumbers. *Lui et al.* [1991] calculate the maximum growth rates for a variety of drift velocities (shown in Table 4.2) demonstrating that the growth rates predicted in the near-Earth plasma sheet are much higher in comparison with our observations, ruling out the CFCI in the near-Earth plasma sheet as a source of auroral beads. However, the maximum rate for the mid-tail plasma sheet with a drift velocity of $V_0 = 0.3v_i$ is more consistent with our observations. We observe rates ranging over an order of magnitude from $0.03 - 0.3$ s^{-1} with a median growth rate observed across all events of ~ 0.05 s^{-1}. In order for this instability to explain our results we estimate $B_z \approx 15$ nT to reproduce a peak in growth rate at $k_{lon,m} \approx 2.5 - 3.75 \times 10^{-6}$ m^{-1} with a low drift velocity of $V_0 \approx 0.3v_i$ which predicts rates of the magnitude we observe.

Figure 4.9*a* shows a comparison of our statistical results with the char-

acteristics of the CFCI reported by *Lui et al.* [1991] for varying plasma sheet location. Our statistical results demonstrate maximum growth rates at low wavenumbers. The growth rates are in more agreements with the mid-tail parameters of the CFCI, however a flat wavenumber versus growth rate profile is predicted, which is not in agreement with our observations which are clearly peaked.

V_0/v_i	0.3	0.5	1.0	2.6	9.0
γ- midtail	0.052			0.62	2.0
γ- near-Earth		0.36	1.12		

Table 4.2: Table of maximum growth rates predicted for different drift velocities for waves in the near-Earth and mid-tail current sheet from *Lui et al.* [1991].

In summary the CFCI predict growth rates which are in the correct region for plasma sheet parameters in between the near-Earth and mid-tail region with low drift velocities. At higher B_z the peak in growth rate becomes more pronounced and occurs at higher wavenumbers and by decreasing the drift velocity lowers the magnitude of the growth rates. However the growth rates for the mid-tail parameters do not explain the clear peak in growth rates we observe when assuming that the beads are the signature of a single instability, and hence we conclude that it is unlikely that the CFCI is responsible for the auroral beads observed. However, further investigation of the effect of changing the plasma parameters on the resulting spatial scales, growth rates and shape of the distribution needs to be done in order to definitively rule this instability in or out.

4.4.2 Shear-Flow Ballooning Instability

The Shear-Flow Ballooning Instability (SFBI) is also a hybrid instability incorporating the Kelvin-Helmholtz instability, driven by small-scale shear flows and the Rayleigh-Taylor instability, driven by large-scale Earthward-directed pressure gradients. Strong azimuthal shear velocities have been observed in the equatorial regions of field line resonances. For example, *Samson et al.* [1996] report of shears up to 200 km s^{-1} over radial distances of the order of 0.1 R_E, however a pure Kelvin-Helmholtz mode has already been ruled out due

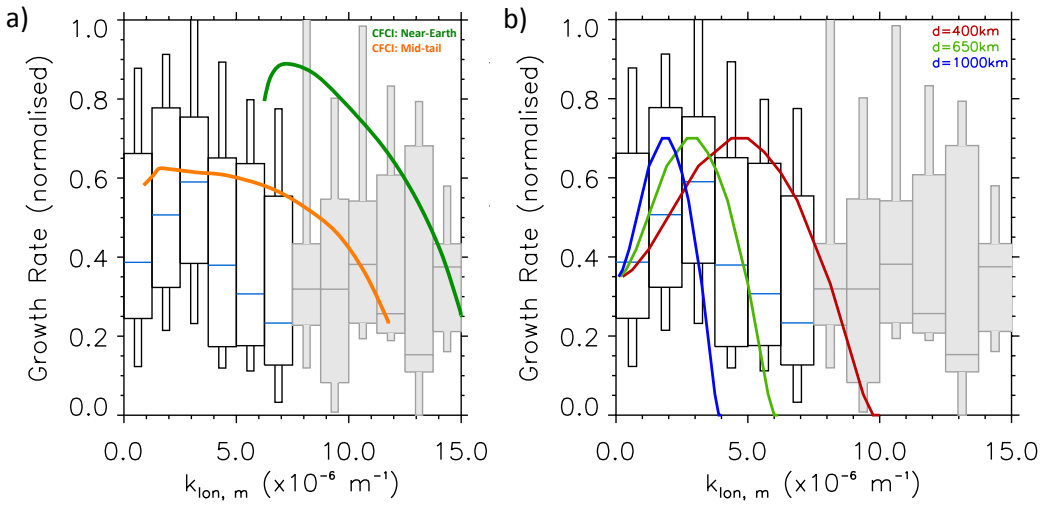

Figure 4.9: The normalised growth rate as a function of spatial scale, in comparison to: (left) the Cross-Field Current Instability characteristics found by *Lui et al.* [1991] for inner-edge plasma sheet parameters (green) where $V_0 = 0.5v_i$, $T_e = 3$ keV, $T_i = 12$ keV and $n_e = n_i = 0.6$ cm^{-3} and mid-tail plasma sheet parameters (orange) where $V_0 = v_i$, $T_e = 0.2$ keV, $T_i = 2$ keV and $n_e = n_i = 0.3$ cm^{-3}. (right) the Shear Flow Ballooning instability characteristics found by *Voronkov et al.* [1997] where $\rho = 4.06 \times 10^{-21}$ kg m^{-3}, $B = 40$ nT. Keeping these parameters constant, different growth rate curves are obtained by varying the width, d of the shear-flow region. The growth rate curves have been normalised to 0.7 which corresponds to a growth rate of 0.2 s^{-1} to facilitate qualitative comparison with the normalised growth rates from observation.

to a too low growth rate [*Hallinan and Davis*, 1970]. On the other hand, the hybrid SFBI possesses significantly faster growth rates and shorter time scale exponential growth than a pure Kelvin-Helmholtz mode, making it a suitable candidate to compare with the growth rates obtained from our optical analysis. The substorm onset arc is tied to the boundary between stretched and more dipolar field at the inner edge of the plasma sheet [*Samson et al.*, 1992b], and in precisely the region where pressure gradients control the physics behind the Shear-Flow Ballooning Instability, again pointing towards beading being the optical manifestation of this magnetospheric instability.

The MHD equations for the radial component of the shear flow velocity V_x is given by:

$$V_x'' = k^2 V_x \left(1 - \frac{V_0''}{k(\omega - kV_0)} - \frac{W}{(\omega - kV_0)^2}\right) \tag{4.1}$$

where

$$W = -\frac{g\rho_0'}{\rho_0} - \frac{g^2}{V_f^2}$$

and $\omega - kV_0(x)$ is a Doppler-shifted wave frequency, $V_f^2 = C_s^2 + V_a^2$ is the square of the fast mode velocity, C_s is the acoustic velocity, V_a is the Alfvén velocity and $V_0(x)$ the shear flow velocity, V_x'' and V_0'' denotes the second derivative with respect to x and g is the centripetal acceleration of the particles as a result of magnetic curvature and particle inertia. When $W > 0$ the pressure gradient is stable, and for $W < 0$ it is unstable and hence able to take part in substorm onset.

Voronkov et al. [1997] found, using a magnetic field $B_z = 40$ nT perpendicular to the large-scale pressure gradient, and plasma sheet mass density $\rho = 4.06 \times 10^{-21}$ kg m^{-3} that the growth rate peaks at 0.2 s^{-1} and that there is an inverse relationship between the most unstable spatial scales and the width of the shear flow region, d. This is in contrast to the CFCI, where an increase in magnetic field strength or ion drift velocity increases the wavenumber at which the growth rate peaks. This is shown in Figure 4.8 where the absolute growth rates predicted by the SFBI and CFCI are compared directly.

Figure 4.9*b* shows a comparison of our statistical results with the characteristics of the SFBI found by *Voronkov et al.* [1997] for a range of shear-flow regions. Our statistical results demonstrate maximum growth rates at small spatial scales which agree well if the SFBI was driven by a shear flow width in the magnetosphere of $600 - 700$ km. Shear flows of this scale have been observed by *Samson et al.* [1996]. This is an extremely localised region in the magnetosphere, but we should note that if the spatial scales of the instability have been underestimated due to the errors in magnetospheric mapping, this would also underestimate the size of the shear flow region predicted.

Our analysis of the SFBI suggests that there are several combinations of plasma and magnetic field characteristics that are able to explain the temporal and spatial characteristics of auroral beads, indicating that the SFBI could be the source of auroral beads observed along the substorm onset arc.

4.5 Discussion and Conclusion

The optical analysis technique presented in this chapter provides a quantitative method to remote-sense the physics of substorm onset from temporal and spatial analysis of substorm-related aurora. In the ionosphere, we have observed the auroral beads with wavelengths of ~ 60 km, evolving to ~ 120 km, in agreement with previous individual case studies e.g., *Friedrich et al.* [2001]; *Samson et al.* [2003]; *Sakaguchi et al.* [2009]; *Rae et al.* [2010]; *Motoba et al.* [2012]. The statistical analysis of multiple auroral brightenings has yielded vital new constraints on the nature of the plasma instability associated with substorm onsets and pseudo-breakups.
Specifically, we find the following:

1. The statistical result of the analysis of auroral spatial scales demonstrates the most unstable azimuthal wavelength of the magnetospheric instability is at least $\lambda_{\perp} \approx 1700 - 2500$ km;
2. The most unstable spatial scales have growth rates ranging from $0.03 - 0.3$ s^{-1} with a median growth rate of 0.05 s^{-1}.
3. The Cross-Field Current Instability in the near-Earth plasma sheet predicts growth rates which are too high to explain our observations
4. The Cross-Field Current Instability in the mid-tail region with low drift velocities could explain our growth rates, however the growth rates predicted do no show a clear peak as observed.
5. The Shear-Flow Ballooning Instability, with a localised shear flow region of ~ 650 km and plasma sheet magnetic field strength of 40 nT can best explain our observed results.

More work is necessary to fully investigate the range of plasma and magnetic field conditions that may support the instabilities identified by our analysis of the substorm aurora.

Specifically, even through the CFCI predicts waves at similar temporal and spatial scales, further analysis of the plasma characteristics is required in order to conclude whether combinations of the plasma sheet parameters and drift velocities can predict a peak in growth rates at the spatial scales

we observe. Magnetic field strengths in the region of 5 nT in combination with relative ion drift velocities of less than half the thermal velocities predict growth rates similar to our observations. However the most unstable spatial scales predicted by the CFCI are lower than those observed from auroral beads. Moreover the wavenumber versus growth rate profile for the CFCI does not match our observations. The lack of a clear peak makes it unlikely that the CFCI is the instability we are observing.

Assuming that only one instability is causing the substorm onset arc suggests that the instability most likely to play a part in the trigger of substorm onset is the Shear-Flow Ballooning Instability, as the peak growth rate of 0.2 s^{-1} at spatial scales of $k_{lon} = 2.5 - 3.75 \times 10^{-6}$ m^{-1} is predicted by this instability with a shear flow region of $\sim$ 650 km. The effect of different plasma parameters such as density, B_z and pressure gradient on the growth rate amplitude and shape as a function of wavenumber requires further investigation.

In our analysis we assumed that a single instability was acting in the inner magnetosphere. For this reason we normalised the growth rates, which showed clear peak in the statistical growth rates. However if this assumption is incorrect and there are multiple instabilities, then we cannot justify this normalisation. If this is the case, then the predictions form the CFCI in the mid-tail region could agree with our observations (Figure 4.7*b*).

In conclusion, we show for the first time a quantitative comparison between observations of the spatial and temporal structuring of the substorm onset arc and its relation to proposed magnetotail instability mechanisms. We statistically demonstrate the evolution in space and time of the substorm onset arc, providing the clearest indication yet that the substorm onset arc itself is both wave-driven and is inextricably linked to a magnetotail instability. The auroral beads exhibit exponential growth across a broad range of spatial scales in the ionosphere initially suggesting that there are no preferential spatial scales for auroral bead growth. However, when we make two relatively simple and reasonable assumptions, that magnetic field mapping introduces a systematic error, and that substorms can grow at different temporal rates, we find that there is indeed a preferred k spectrum peaking at low wavenumbers.

To provide further evidence that we are measuring the ionospheric optical manifestation of a magnetospheric instability in-situ space measurements are required. Our results provide the strongest evidence yet that the substorm onset arc is created by a plasma instability such as the Shear-Flow Ballooning Instability [*Voronkov et al.*, 1997]. We use a combination of ground-based data and magnetic field mapping to predict the location of the instability in space and it's spatial scales. By doing so, we provide important estimates of the characteristics of the magnetotail region driven unstable during the substorm and containing the substorm onset arc.

Chapter 5

Statistical Azimuthal Structuring of the Substorm Onset Arc: Implications for the Onset Mechanism

In Chapter 4, we showed that auroral beads that form along the substorm onset arc exhibit:

- A clear peak in power at low spatial scales.
- Individual spatial scales which grow exponentially with time, with specific spatial scales growing faster than others.

Exponential growth across a wide range of spatial scales suggests that an instability is responsible for the auroral beads. In this chapter we investigate whether or not beads are a 'special' case by investigating how frequently they are observed along the substorm onset arc when using an independent substorm list to provide an unbiased method of selecting our events. We therefore address whether auroral beads are a common feature during auroral substorm onset, and how this relates to substorm onset processes in the magnetosphere.

We do this in a number of ways: firstly, we use an independent substorm list (SOPHIE) to remove any bias from our event selection, rather than purposely selecting events which have a clear beading signature as in Chapter 4. Secondly, in order to increase the size of events studied, we develop an arc-finding algorithm that identifies the substorm onset arc, allowing the analysis to be performed on many more onset arcs, rather than using a static

analysis box which requires the arcs to remain reasonably stationary during the analysis window, and well-aligned with geomagnetic latitude.

The results presented in this chapter have been published in *Geophysical Research Letters* with the citation, Kalmoni, N. M. E., I. J. Rae, K. R. Murphy, C. Forsyth, C. E. J. Watt, and C. J. Owen (2017) Statistical Azimuthal Structuring of the Substorm Onset Arc: Implications for the Onset Mechanism, *Geophys. Res. Lett*, doi:10.1002/2016GL071826

5.1 Introduction

5.1.1 Using the Aurora to Remote-Sense the Magnetosphere

The substorm is a sudden brightening of the most equatorward auroral arc in the midnight sector of the auroral oval which leads auroral breakup and the large-scale expansion of the aurora across the auroral oval [*Akasofu*, 1964, 1977]. The magnetospheric dynamics linked to this process can be remotely sensed through space and ground-based auroral campaigns [*Shiokawa et al.*, 1996; *Mende et al.*, 2000, 2008; *Angelopoulos*, 2008; *Motoba et al.*, 2012]. These have enabled detailed studies of the morphology of substorm aurora and revealed the complexity of substorm observations and dynamics initially reported by *Akasofu* [1964, 1977]. Structures known as auroral rays or beads have been observed to form azimuthally along the substorm onset arc in the minutes before auroral substorm onset, e.g., *Davis* [1962]; *Henderson* [1994]. In recent years there have been many studies of auroral beads from data acquired by high temporal and spatial resolution ground-based All-Sky Imagers (ASIs) e.g., *Friedrich et al.* [2001]; *Kepko et al.* [2009]; *Sakaguchi et al.* [2009]; *Rae et al.* [2009b,a, 2010]; *Motoba et al.* [2012]; *Murphy et al.* [2014]; *Kalmoni et al.* [2015] in which beads are reported to have spatial scales, or wavelengths, in the range $30 - 150$ km in the ionosphere. *Sakaguchi et al.* [2009] reported two case studies of substorm onset arcs which exhibited beading with spatial scales of $30 - 60$ km in the ionosphere. This scale closely corresponds to the ion gyroradius of $1 - 10$ keV protons in the plasma sheet at 10 R_E where the

magnetic field strength is ~ 12 nT, suggesting that the beads were not caused by a purely MHD instability. However, as discussed in Section 2.3, calculations of a typical ion gyro radius rely on estimates of the magnetic field strength using equilibrium field models, e.g., *Tsyganenko* [1989, 1995], which are not reliable during substorm times. Hence it is difficult to rule out MHD or kinetic instabilities from these calculations alone. *Motoba et al.* [2012] observed beads with wavelengths of $30-50$ km at magnetically conjugate stations in the Northern and Southern hemisphere, confirming that the source of the beads is most likely in the equatorial magnetosphere. There have also been multiple substorm studies in which auroral beads were not reported, e.g., *Angelopoulos et al.* [2008]; *Nishimura et al.* [2010], leading to a general consensus that auroral beads are only part of the auroral substorm sequence in a small subset of substorms.

5.1.2 Auroral Beads and Plasma Instabilities

Typically the formation of exponentially growing auroral beads at substorm onset has been associated with the development of a plasma instability in the inner magnetosphere prior to the onset of reconnection in the tail e.g., *Rae et al.* [2009a]; *Murphy et al.* [2014]; *Kalmoni et al.* [2015]. *Rae et al.* [2009a] showed that auroral beads in the ionosphere and coincident ULF Pi1-2 wave activity preceded auroral breakup. In the absence of any observational evidence for the occurrence of reconnection, these authors concluded that a near-Earth magnetospheric instability developed before the onset of reconnection in the tail. Using ground-based and multi-point in-situ data *Murphy et al.* [2014] presented a detailed analysis of two consecutive substorms and demonstrated that the development of auroral beads and conjugate disturbances in the inner-magnetosphere preceded all evidence of tail reconnection further away from the Earth, however these were only individual case studies.

Kalmoni et al. [2015] presented a statistical study of auroral substorm onset arcs with clear, visually-identified, auroral beads. The authors demonstrated that, for all of these arcs, the bead amplitudes grew exponentially with time for a common range of spatial scales, suggesting these are evidence of wave

processes in the magnetosphere. This exponentially-growing auroral beads signature is indicative of a plasma instability, e.g., *Rae et al.* [2010]. The statistically dominant magnetospheric spatial scales of $k = 2.5 - 3.75 \times 10^{-6}$ m^{-1} and growth rates of ~ 0.05 s^{-1} obtained by *Kalmoni et al.* [2015] are consistent with both the shear-flow ballooning instability [*Voronkov et al.*, 1997] at the inner-edge of the plasma sheet and the cross-field current instability for typical mid-tail plasma parameters [*Lui*, 2004]. The majority of event studied mapped to $9 - 12$ R$_E$ in the magnetotail using a T96 model [*Tsyganenko*, 1995].

5.1.3 Prevalence of Auroral Beads in the Substorm Onset Sequence

In this chapter we investigate whether beads are a common feature in the substorm onset arc, or whether they are a 'special case', belonging only to the current disruption model of substorms, and not to substorms initiated by reconnection in the tail. We perform quantitative analysis of 195 onset arcs from an independent substorm list, SOPHIE [*Forsyth et al.*, 2015], in order to investigate whether azimuthal arc structure is a common feature. Through detailed, quantitative analysis we demonstrate that well-defined spatial scales (i.e., auroral beads) are observed in 90% of onset arcs.

5.2 Analysis Methods

In this study we used data from the ASIs [*Mende et al.*, 2008] associated with the NASA Time History of Events and Macroscale Interactions during Substorms (THEMIS) mission [*Angelopoulos*, 2008] to quantitatively and statistically characterise the azimuthal structure of auroral onset arcs. An example of the analysis technique used to make this characterisation is shown in Figure 5.2. Figure 5.2*a* shows an isolated auroral substorm observed at the centre of the Fort Yukon ASI on 9 February 2007. The three images show the evolution from a faint auroral arc at 10:16:00 UT, to a highly structured bright arc at 10:17:00 UT, resulting in auroral breakup at 10:17:30 UT.

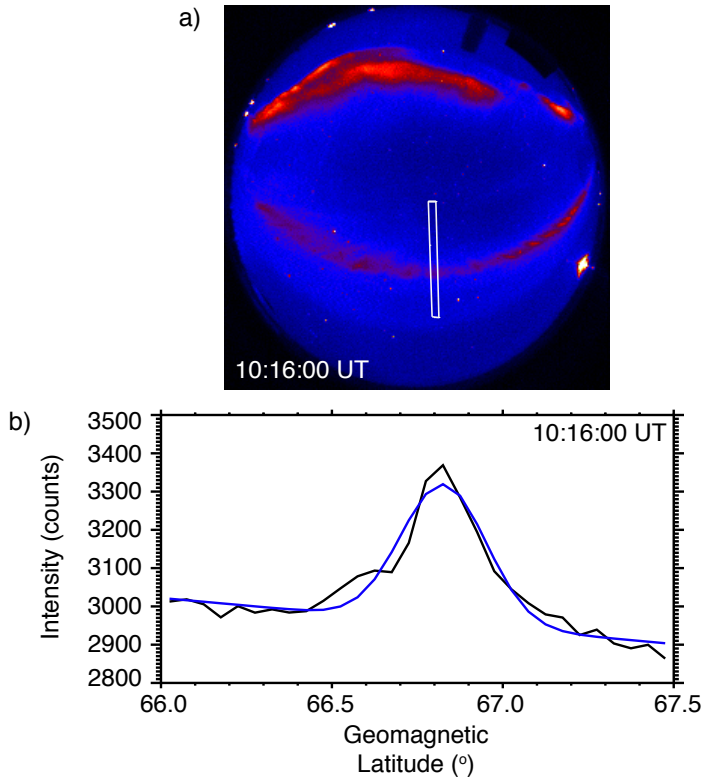

Figure 5.1: Technique used to identify the latitudinal location of the auroral arc as a function of longitude and time.(*a*) A latitudinal slice along a narrow longitudinal range is used to to create a latitudinal auroral intensity profile (*b*, black line). A Gaussian is fitted to the intensity profile (blue) to identify the centre of the auroral arc. This is repeated for the full range of longitudes at each time so the extent and evolution of the arc location is identified.

5.2.1 Arc Identification

In order to statistically study azimuthal structuring of auroral arcs, we first develop a method to automate arc identification, so that the arcs can be tracked for as long as possible. In Chapter 4, our analysis technique relied on the assumption that auroral arcs are closely aligned with constant geomagnetic latitude. This is typically true for arcs around 23:00 MLT, whereas auroral arcs are often tilted south-east prior to 23:00 MLT (magnetic local time) and north-east after 23:00 MLT, deviating from constant latitude contours by as much as 20 degrees [*Gillies et al.*, 2014]. This is presumably the result of the magnetotail being more stretched around 23:00 MLT than on the dawn and dusk flanks. Often, the onset arc will be skewed relative to constant geomagnetic latitude, making routine analysis using the technique outlined in

Chapter 4, of the azimuthal structure of the arc more difficult. We develop an arc-finding algorithm to track the latitudinally moving onset arc as a function of longitude due to the growth phase and early expansion phase of the substorm. To account for latitudinal skewing of the arc, we find the position of the arc in latitude as a function of geomagnetic longitude for each image by fitting a Gaussian function to each longitudinal slice to find the latitudinal centre of the arc. Figure 5.1*b* (black) shows an example of a latitudinal slice (indicated in Figure 5.1*a*) of auroral intensity at a narrow longitudinal location along the arc. The latitude versus intensity profile is fitted using a Gaussian function (blue) to determine the centre of the arc. The latitudinal and longitudinal range of arc-fitting a pre-defined by the user, so that, as can be seen in Figure 5.1, the poleward aurora are not included in the fit. The arcs are tracked until auroral breakup as identified by eye, at which point, by definition, there is no longer a discrete arc as the westward travelling surge has formed and aurora has begun to fill the night sky. Examples of the arcs determined by this method are outlined in white/black in Figure 5.2*a*. The arc is most clearly visible in the earliest frame shown, and does not change orientation appreciably in subsequent frames.

5.2.2 Auroral Substorm Onset Determination

The total auroral intensity is used to determine auroral substorm onset which is our zero epoch time for this statistical study. Figure 5.2*b* shows the logarithm of the total auroral intensity in the whole field of view of the Forth Yukon imager for the duration of the event. We define substorm onset as the start time of large-scale exponential growth of the total auroral intensity in the field of view of the ASI. Substorm onset has been identified as 10:16:33 UT for this event using the following definition:

Auroral substorm onset is calculated by extending the analysis window by 2 minutes before the auroral arc is first tracked and 1 minute after auroral breakup, allowing the full auroral breakup dynamics to be observed and making the technique more robust. A linear fit to the log of the brightness is calculated to determine the onset time using the following technique:

The local peaks, identified by a change in sign of the gradient, in the extended total intensity-time series are found. Prior to substorm onset, many peaks of very low amplitude are identified, however once the auroral intensity starts to increase rapidly, fewer local peaks which have a much higher amplitude are found. The first local peak which rises above a 1.0σ threshold of all the local peaks found in the extended time series is used as the final point, t_{final}, in the linear fit. A linear fit is then calculated, starting at each time point prior up until t_{final} to determine the onset time. Auroral substorm onset is the time of the start of the fit with the maximum Pearson correlation coefficient, or the earliest time at which the Pearson correlation coefficient exceeds 0.99. If no peak local peak matches the final point criteria t_{final}, then the last point in the time-series is used.

5.2.3 Along-Arc Keogram

In order to investigate the azimuthal structuring of the auroral arc, the auroral intensity for the latitudinally-moving arc (equatorward during the growth phase and poleward during the expansion phase) is used to create an along-arc (East-West) keogram as a function of geomagnetic longitude. Figure 5.2*c* shows the along-arc keogram for the moving arc identified by the arc-finding algorithm described above. On close inspection of the keogram, auroral beading, indicated by faint parallel features of higher intensity moving Westward (to lower longitudes), is visible at longitudes above $-94.0°$ prior to 10:16:30 UT. However the beading signature also becomes visible in the centre of the keogram after 10:16:00 UT at $\sim -97.0°$ longitude. These beads initially move in both Eastward and Westward directions until 10:16:33 UT (auroral onset) after which they all propagate together in the Eastward direction. The sudden change in bead direction (and/or velocity) is not an uncommon observation around the time that large-scale exponential growth of the total auroral intensity commences.

We note here that any aurora observed by the THEMIS ASIs has both an azimuthal and altitudinal extent. Hence, closer to the horizon within the THEMIS ASI field of-view, altitudinal structuring can easily be conflated with

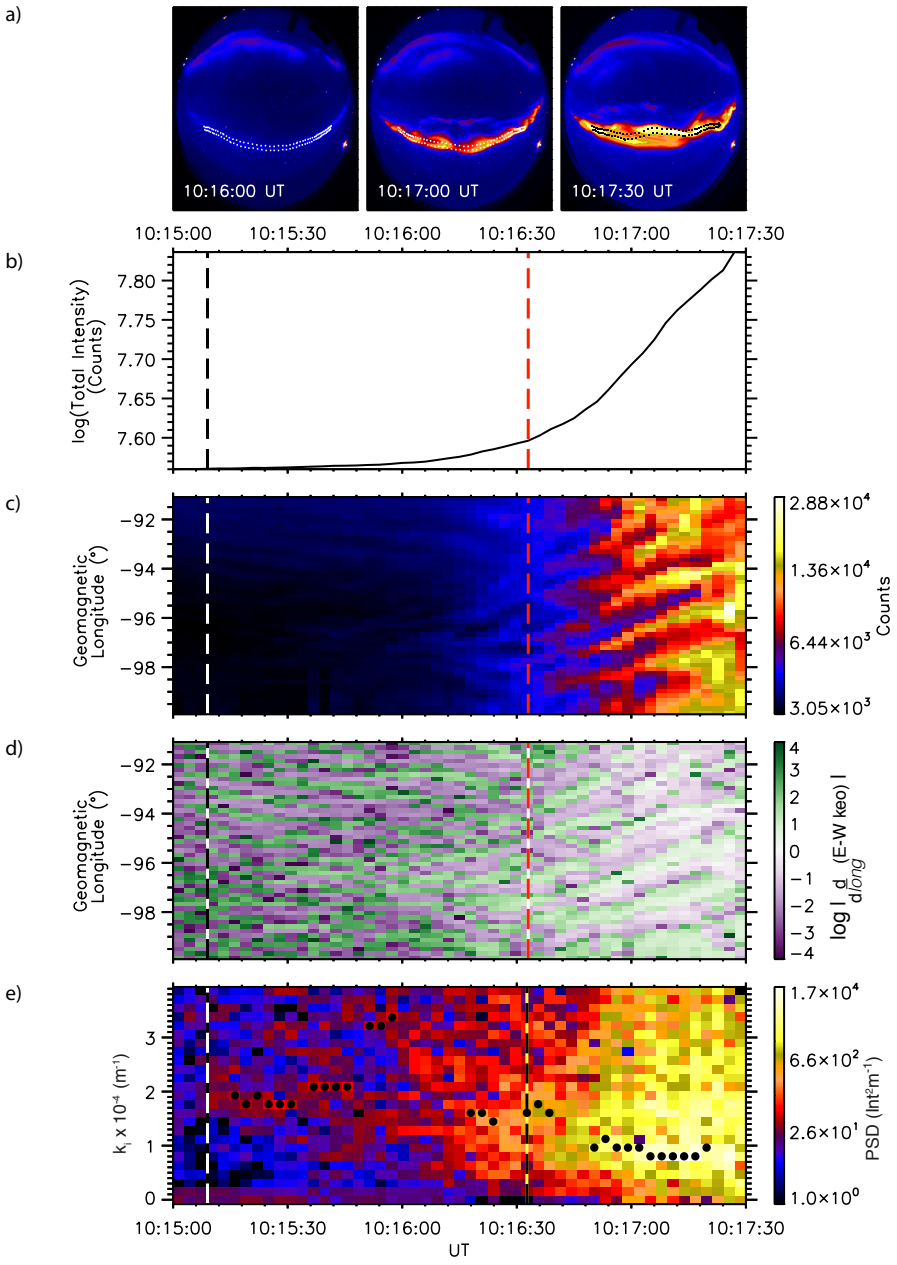

Figure 5.2: Auroral substorm observed from Fort Yukon all-sky imager on 9 February 2007. (a) The substorm onset arc in the minutes before auroral breakup. The outline of the pixels used for analysis is shown in white/ black. (b) The change in total auroral intensity from 10:15:00 - 10:17:30 UT is shown on a logarithmic scale. (c) Along-arc keogram of the auroral intensity shown in (a) to show the azimuthal structure of the aurora. (d) Spatial differential of the along-arc keogram to detrend the data, making beads more easily visually identifiable. (e) Dynamic power spectral density calculated from the differentiated keogram shown as a function of longitudinal wavenumber at 110 km altitude and time. The times and spatial scales where a clear peak in power spectral density is identified are indicated by the black dots. Beading onset is indicated by the first vertical line in panels *b*-*e* at ∼10:15:09 UT. The start of the large-scale exponential growth of the aurora (auroral onset) is indicated by the second vertical line at ∼10:16:32 UT.

azimuthal structuring, rendering issues with any statistical studies. In order to reduce the effect of any vertical structuring affecting our analysis as much as possible, we do not perform our analysis on onset arcs at the edges of the field-of-view of the auroral imagers with elevation angles less than 25^o from the horizon. The vast majority of our events have minimum elevation angles ranging between $30^o - 40^o$. Instead, we concentrate on substorm onset arcs closer to zenith where any altitudinal effects will be minimised.

5.2.4 Power Spectral Density

We use Fourier analysis of the East-West keogram to identify the characteristic structuring of the onset arc. A robust characterisation of the spatial scales requires the signal to be detrended without being polluted by a background, e.g., the homogenous background auroral arc. We use along-arc numerical differentiation (with respect to longitude) to remove the background auroral arc. This allows the study of the variations in background intensity along the arc, with minimal background contributions, and hence the resultant dataset is primarily of auroral bead amplitudes only. The differentiated keogram from which the auroral background has been removed is shown in Figure 5.2*d*. The intensity gradients associated with the auroral beads are identified throughout the along-arc keogram by the coherent green and purple features indicating a positive and negative gradient in bead intensity, respectively. This analysis reveals the much clearer visual signatures of beads by the transition from green to purple in the keogram.

Hence, we apply Fourier analysis to each time point of the differentiated keogram containing signatures of the beads only (Figure 5.2*d*) using the method outlined in *Kalmoni et al.* [2015] and Chapter 4 of this thesis. However, as we perform the analysis on the differentiated keogram (rather than detrended keogram in Chapter 4), this results in a whitened PSD i.e., multiplied by a factor of k^2. The whitened PSD gives the appearance of higher spatial scales having significantly higher amplitudes and therefore broadens spectral peak from the a regular bead signature which is quasi-monochromatic.

Figure 5.3*a* shows an example of a slice through the whitened PSD plot

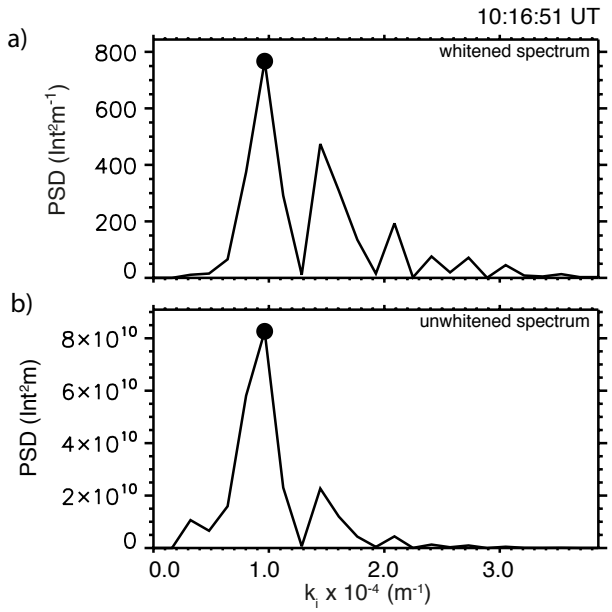

Figure 5.3: Slice of whitened and unwhitened PSD at 10:16:51 UT through Figure 5.2*e*. The peak appears less broad in the unwhitened spectrum. The characteristic spatial scale for this time is identified by the highest peak and is indicated by the black dot.

at 10:16:51 UT. The difference in the appearance of the dominant peak when the resulting PSD spectrum is unwhitened, by dividing the PSD through by a factor of k^2, is shown in Figure 5.3*b*. The unwhitening of the spectrum suppresses the power at higher spatial scales, and enhances the dominant peak identified.

We identify the temporal evolution of characteristic spatial scales from the dominant peaks in PSD. Figure 5.2*e* shows the PSD, the time evolution of the spatial Fourier transform of the differentiated along-arc keogram, quantified as a function of wavenumber, k. The PSD evolves from higher to lower wavenumbers (smaller to larger wavelengths) through the late growth phase and early expansion phase and grows around 3 orders of magnitude in the process.

In this study we use the dynamic PSD to calculate to following parameters to determine whether auroral beads are embedded within the substorm onset arc, and, if so, their evolution:

- **Characteristic spatial scale as a function of time**: The location of local peaks in the PSD in k-space allows us to determine whether

the auroral arc has a characteristic spatial scale, or wavenumber, at a particular time. A dominant peak in PSD at a specific time indicates that there is a characteristic spatial scale embedded within the onset arc, and hence that the arc has auroral beads.

The characteristic spatial scales are found as follows: all peaks in the whitened PSD at each time-point are identified by a change in sign of the gradient. The characteristic spatial scale is defined if the peak amplitude exceeds 1.3σ of all the identified peaks. The 1.3σ cut-off level was chosen after trialling this technique for multiple events, as it depends on the total number of peaks identified, which varies between times and events. We allow up to 2 characteristic spatial scales to be identified at any time, in order to allow the possibility of two superposed spatial scales to be identified if present. The lowest two wavenumber bins from the Fourier transform are discounted when finding peaks, as these correspond to the zeroth-, and $2\pi/N\Delta x$ wavenumber bins, where N is the total number of bins used for arc tracking ($N = 50$ in this event) and Δx is the bin size ($\Delta x \approx 8000$ m in this event). For this event $k_1 = 0.15 \times 10^{-4}$ m^{-1}, corresponding to a wavelength of $\lambda_1 = 400$ km, which is comparable to the length of the arc studied, hence this wavenumber would correspond to ~ 1 bead along the arc which too large in comparison to the coverage of the auroral arc and hence does not correspond to auroral beads.

The characteristic spatial scales identified are indicated in Figure 5.2*e* by the black dots in the amplitude spectra.

- **Time of bead onset**: The time at which beads start to form along the onset arc, relative to auroral onset allows the inference of the auroral sequence of events leading to substorm onset. The time of bead onset is defined as the first time point in a 30 second sliding window where a characteristic spatial scale is identified for 80% of the time points within the window, to determine whether a persistent beading signature is identifiable for at least 30 s, as this is the typical period of the beads [*Rae et al.*, 2010]. The 80% cut-off is chosen, incase a characteristic spatial scale is not identified for a particular time, even if beads are present at

that time.

- **Bead amplitude as a function of time**: Identifying the bead amplitude allows us to investigate how the beads evolve through onset, and understand why they have not been identified frequently in the past. The amplitude of each characteristic spatial scale is calculated by converting PSD to amplitude (outlined in Section 3.4).

5.2.5 Event Selection Criteria

The analysis and methodology described above is applied to ~ 200 independently identified substorm onset arcs in order to statistically quantify the azimuthal structure of such arcs. The substorms are identified using the SOPHIE algorithm [*Forsyth et al.*, 2015] from the years $2006 - 2014$ inclusive. The SOPHIE algorithm identifies substorms by identifying growth, expansion and recovery phases using the SuperMag SML index [*Newell and Gjerloev*, 2011; *Gjerloev*, 2012] and provides an independent and hence unbiased substorm list from which events are selected without any pre-condition of clear auroral beading signatures, as in Chapter 4. In order to limit our study to clearly identifiable substorm onsets that are not part of any preceding activity, the following selection criteria was used:

a) The SOPHIE substorm expansion phase was preceded by a SOPHIE growth phase.

b) There was a clear visually identified auroral breakup in the field of view of one of the ASI at the SOPHIE onset time ± 15 minutes.

c) There is a pre-existing arc in the lead up to substorm onset which becomes the onset arc, or the sudden formation of an arc [*Akasofu*, 1964, 1977].

d) If the SOPHIE onset is not an isolated auroral substorm, then the first auroral substorm in the sequence is used.

e) The initial auroral brightening is observed within the field of view of the analysis ASI (135 events) or propagates into the field of view from the East/ West (i.e., if there is no data in the exact onset location as the sky is overcast) (60 events).

Events are tracked for a varying duration of time for each substorm, depending on whether the onset arc develops from a pre-existing growth phase arc, whether the arc suddenly forms at auroral onset and how quickly it breaks up. Each onset arc is tracked until auroral breakup, which is visually identified, at which point there is no longer a discrete arc as the westward travelling surge has formed and aurora has begun to fill the night sky. The THEMIS ASI resolution at zenith is ~ 1 km, however in order to track the full extent of the auroral arc we use data from a large range of elevation angles. Data closest to zenith is averaged across a few pixels to match the resolution at lower elevation angles. The extent of averaging required varies from event to event depending on the location of the auroral arc in the ASI. This provides equally spaced azimuthal bins necessary for subsequent Fourier analysis of the East-West keogram. The smallest spatial scale limit for each arc studied is set by Fourier Nyquist wavenumber, which depends on the size of the azimuthal bins used to track the auroral arc.

5.3 The Azimuthal Structuring of the Onset Arc

5.3.1 Superposed Epoch Analysis

Figure 5.4 shows a superposed epoch analysis of the results for all 195 events analysed, where auroral substorm onset corresponds to the zero epoch time as discussed. Figure 5.4*a* shows the number of data points used to make Figure 5.4*b*, *c*. Note that the number of points can exceed the number of events (195) used in the study, as the individual PSDs (e.g., Figure 5.2*e*) are re-binned into a uniform common k versus *time* grid to create the statistical plot in Figure 5.4*b*. This means that for events with a low Nyquist wavenumber, multiple points for the same event can fall into a single statistical bin. In the range from -2.5 to $+1$ minutes and up to $k = 3.0 \times 10^{-4}$ m^{-1} there are over 100 data points per bin (shown in white in Figure 5.4*a*). This shows that the results between these values presented in Figure 5.4*b* - *d* are not statistical outliers.

Figure 5.4*b* shows the median PSD, calculated from all 195 arcs as a func-

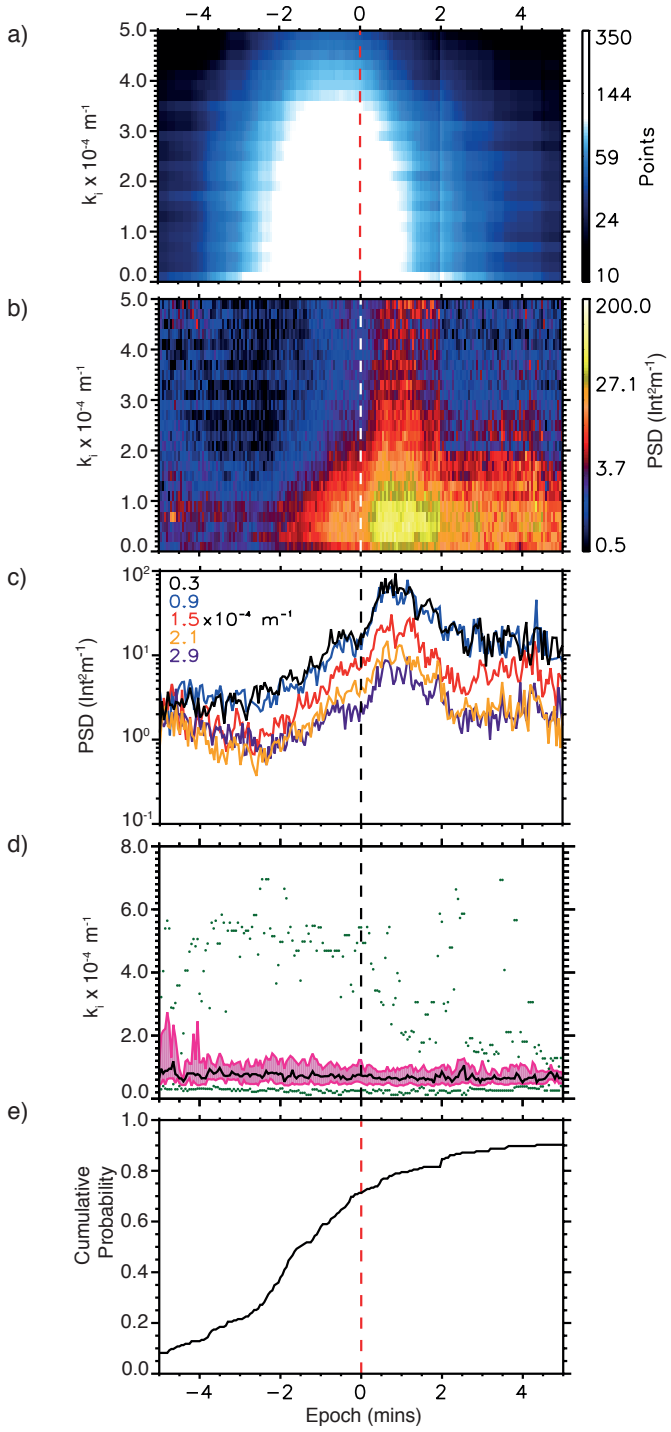

Figure 5.4: Statistical results from the analysis of 195 substorm onset arcs. The epoch time is auroral onset (the second vertical line in Figure 5.2 *b* - *e* as defined for that event). (*a*) Number of points in each bin. The white area indicates over 100 points/bin: this coverage is achieved from -2.5 to +1 minutes surrounding onset and up to $k = 3.5 \times 10^{-4}$ m^{-1}. (*b*) Median statistical Power Spectral Density as a function of along-arc wavenumber and time. Low wavenumber are enhanced $2 - 3$ minutes before auroral onset, after which all wavenumbers grow. (*c*) Horizontal slices of the PSD for 5 representative wavenumbers: $k =$ 0.3 (black) , 0.9 (blue), 1.5 (red), 2.1 (yellow), 2.9 (purple) $\times 10^{-4}$ m^{-1}. (*d*) Statistics of the peak wavenumbers identified (the black dots in Figure 5.2*e*). Median peak wavenumber as a function of time is shown by the black line, upper and lower quartiles within the pink shading. Minimum and maximum values identified for each time point are shown by the green dots. Note the y-axis has been extended up to $k = 8.0 \times 10^{-4}$ m^{-1} in this panel. (*e*) Cumulative probability of the bead onset time showing the proportion of events which exhibit beading relative to auroral substorm onset.

tion of wavenumber. The median PSD exhibits a peak at low wavenumbers, indicating that beads are statistically evident in the independently selected substorm onset arcs analysed. The statistical analysis shows a tendency for PSD to peak at low characteristic wavenumbers, $k = 0.4 - 1.2 \times 10^{-4}$ m^{-1} ($\lambda = 50 - 160$ km), with 80 km spatial scales being the most common. We note here that the broader spectral peak may be due to a combination of statistical averaging over many events, and the effect of using whitened PSDs (e.g., Figure 5.2*e*) to generate this statistical plot. In general, enhancement of PSD at these wavenumbers exists $2 - 3$ minutes prior to substorm onset. Around 2 minutes prior to substorm onset, the statistical wave power grows over a large range of spatial scales up to $k = 2.0 \times 10^{-4}$ m^{-1}.

In Figure 5.4*c*, we also show growth through specific wavenumbers to demonstrate that growth over a wide range of wavenumbers commences at approximately the same time. Hence, the appearance of growth at higher wavenumbers occurring later in Figure 5.4*b* is an effect of the colour scale plot, as the lower wavenumbers have a higher background power than the higher wavenumbers. Figure 5.4*c* shows horizontal slices on a logarithmic scale through 5 representative wavenumbers shown in Figure 5.4*b* for $k = 0.3$, 0.9, 1.5, 2.1, 2.9 $\times 10^{-4}$ m^{-1}. The overall exponential trend in PSD growth is consistent with the linear stage of a plasma instability, as has been previously shown in individual case studies [*Rae et al.*, 2010; *Kalmoni et al.*, 2015]. Growth in the statistical PSD of the beads is observed prior to large-scale auroral substorm onset (Figure 5.2*b*) over a wide range of spatial scales. This is the exponential growth of the beads, which starts prior to the large-scale exponential growth of total auroral intensity (which includes both the background auroral arc intensity and the auroral beads). Hence, the median of auroral bead power at each wavenumber shows exponential growth in the minutes before the more generally accepted definition of auroral onset.

Figure 5.4*d* shows the statistics of the characteristic spatial scales identified using the method described in Section 5.2.4 which are denoted by the black dots in Figure 5.2*e*. The median spatial scale remains approximately constant at $k = 0.8 \times 10^{-4}$ m^{-1} ($\lambda = 80$ km) at all epochs. There is no clear

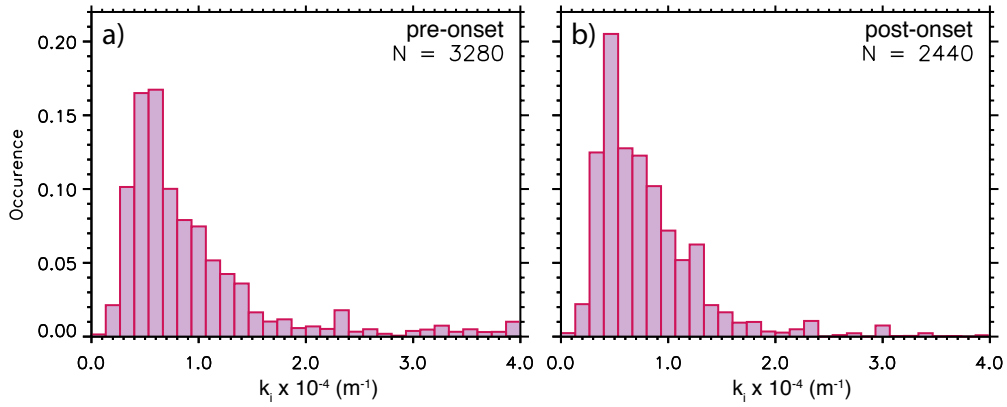

Figure 5.5: Histogram showing the sum of the distributions of characteristic spatial scales for each event. The total distributions for pre- (left) and post- (right) onset times, with the median wavenumber value for the distributions reducing from $k_{pre,med} = 0.87 \times 10^{-4}$ m^{-1} ($\lambda_{pre} = 72$ km) to $k_{post,med} = 0.73 \times 10^{-4}$ m^{-1} ($\lambda_{post} = 86$ km), and hence statistically a slight reduction in the characteristic spatial scales after onset.

change in the median (black), upper and lower quartiles (pink), and minimum (lower dotted) values of the distributions of characteristic spatial scales before and after substorm onset. This suggests that, at least in each event, one single instability dominates for the duration of the analysis, or that multiple instabilities which excite the same characteristic wavenumber must be present.

Auroral beads were detected by our automated algorithm for over 90% of events analysed. The cumulative probability of auroral beading is shown in Figure 5.4*e*. This is calculated from the beading onsets described in Section 5.2. Characteristic azimuthal spatial scales are detected for 70% of events prior to auroral onset, increasing to 90% at 2 minutes post onset, demonstrating that instabilities are integral to the substorm onset process.

5.3.2 Characteristic Spatial Scales

Figure 5.5 shows the distribution of the characteristic spatial scales identified 2 minutes prior (left) and 2 minutes post (right) substorm onset. The distributions shown are the sum of the characteristic spatial scales identified by the analysis described in Section 5.2.4 and shown by the black dots in Figure 5.2*e* of all events analysed. The peak of the distribution is $k_{max} = 0.5 \times 10^{-4}$ m^{-1} both before and after substorm onset. However there is a reduction in the median wavenumber from $k_{pre,med} = 0.87 \times 10^{-4}$ m^{-1} ($\lambda_{pre} = 72$ km) prior

to onset, to $k_{post,med} = 0.73 \times 10^{-4}$ m^{-1} ($\lambda_{post} = 86$ km). A narrowing of the distribution after onset, with an increase in height of the peak, also shows this effect, as the beads statistically transition from smaller to larger scales through onset. This decrease in wavenumber is also visible in the example event presented in Figure 5.2*e* where the identified characteristic wavenumbers are lower after onset. This shows that beads are a ubiquitous signature of the substorm onset arc, and are an indication that the instability causing the beading signature evolves from smaller to larger spatial scales as it progresses. In order to understand why beads have previously been under-reported, we examine the relative amplitude of the detected beads to the auroral arc on which they occur.

5.3.3 Auroral Bead Amplitude

Figure 5.6*a* shows the occurrence probability of fractional bead amplitude (bead amplitude / arc intensity) as a function of arc intensity for pre- (i) and post- (ii) onset times. The arc intensity is defined as the median background arc auroral intensity at that time. The increasing trend in the distribution shows that bead amplitude and arc intensity grow independently from each other.

Figure 5.6*b* shows the probability of fractional bead amplitude (bead amplitude / arc intensity) as a function of bead amplitude in the same format as Figure 5.6*a*. The distribution shows that for larger bead amplitudes, the beads constitute a larger fraction of the total arc intensity, which means that they are more easily visually identifiable. Figure 5.6*b* also demonstrates that there is a higher likelihood of high bead amplitude post-onset (ii) compared to pre-onset (i). This demonstrates that both absolute bead amplitudes and bead amplitude relative to the background arc intensity grow during substorm onset. Prior to substorm onset the distribution has a tail of low bead amplitudes, which are less than 40 counts above of the background arc, and 1% of the total arc intensity (bottom left of Figure 5.6*b*(i)). Very few points in the distribution have amplitudes above 2000 counts and extend above 30% of the total arc intensity (top-right of Figure 5.6*b*(i)). Post-onset, Figure 5.6*b*(ii), it

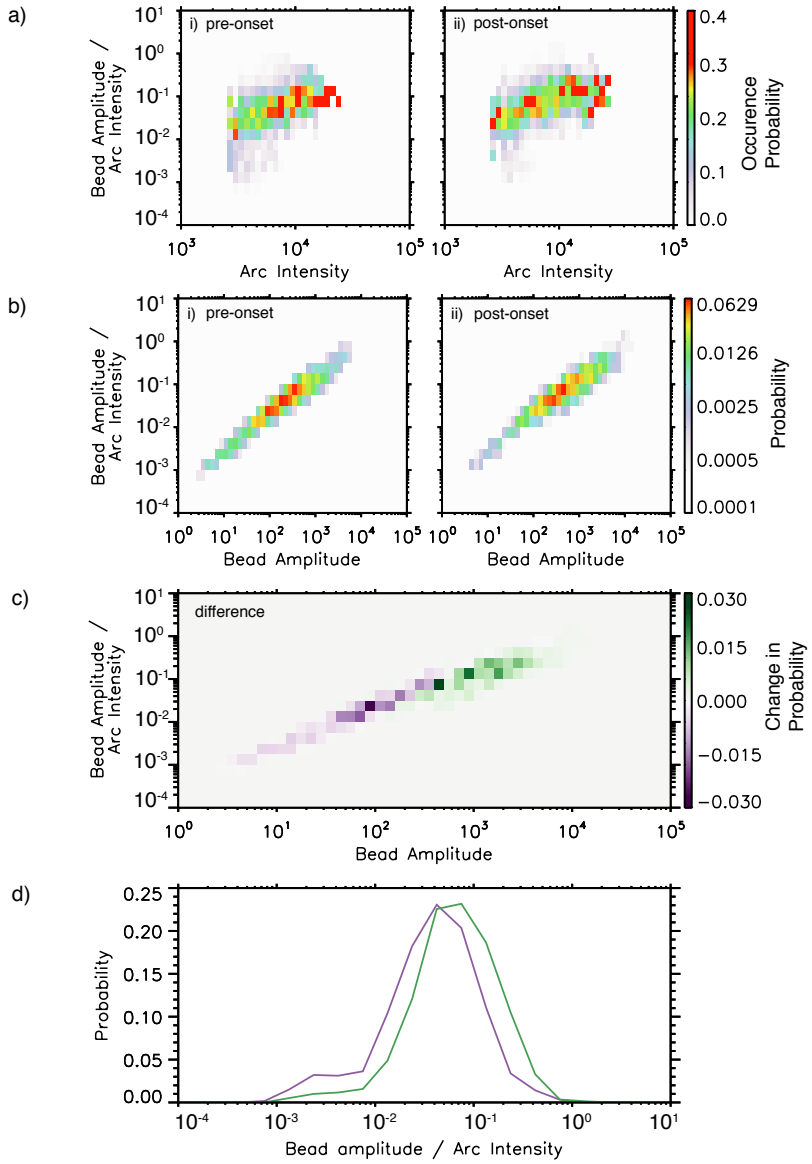

Figure 5.6: (a) Occurrence probability of the ratio of bead amplitude to median arc intensity as a function arc intensity. for each time point where a peak wavenumber is identified (e.g., Figure 5.2*e*). Amplitude for pre onset (i) and post-onset (ii) times shown as a 2D histogram. Fractional bead amplitude is lower for low arc intensity, showing bead amplitude dominates the fraction. (b) Probability of the ratio of bead amplitude to median arc intensity as a function of bead amplitude for pre-onset (i) and post-onset (ii) times shown as a 2D histogram. Higher counts are observed towards the lower-left of the distribution prior to onset, this shifts to higher counts at higher amplitudes towards the top-right of the distribution after onset. (c) 2D histogram difference between the pre- and post- onset probabilities. (d) The probability distribution of the fractional bead amplitude for beads before (purple) and after onset (green).

is clear from the lower left of the two dimensional histogram that fewer events have such low bead amplitudes, and that there are more events with higher bead amplitudes and fractional bead amplitudes, showing that the bead amplitude grows through substorm onset. Clearly, the auroral arc intensity also grows. However a change in both the absolute bead amplitude, as well as the fractional bead amplitude between the pre- and post- onset distributions, demonstrates that not only that there is an increase in bead amplitude during the substorm onset process, but also that the bead amplitude and arc intensity grow independently from each other.

In Figure 5.6*c* we show the difference in the pre- and post-onset distributions. The difference in the distribution confirms that there is a decrease in the percentage of points in the distribution where the bead amplitude is a small fraction of the background arc intensity, and an increase in the number of points where the bead amplitude is a larger fraction of the background arc intensity. Figure 5.6*d* shows the probability distribution of the fractional bead amplitude. The pre-onset fractional bead amplitude distribution shifts towards higher fractional amplitudes after onset. This change confirms that the bead amplitude and arc intensity are changing independently of each other during the onset process. Pre-onset, 88% of the events have beads with amplitude of less than 10% of the arc intensity, post onset this number decreases to 76%. Despite the fact these onset arcs are almost always azimuthally structured, the majority of auroral beads have an amplitude lower than 10% of the background arc. This low fractional bead amplitude explains why beads are not frequently reported during substorms, as low amplitude beads will not be visually identified unless quantitative auroral analysis techniques, such as those described in this Chapter are used.

5.4 Discussion

In this chapter we present evidence that azimuthal structuring known as 'auroral beads' is a fundamental component of the onset arc, and beads are observed in at least 90% of auroral substorms. This study is the most comprehensive

statistical study to date which supports theories [*Lui et al.*, 1991; *Roux et al.*, 1991; *Voronkov et al.*, 1997; *Lui*, 2004] that an instability is an integral component to the substorm mechanism, and previous observations e.g., [*Rae et al.*, 2009a, 2010; *Motoba et al.*, 2012; *Kalmoni et al.*, 2015] by showing that auroral beads, the ionospheric manifestation of a plasma instability, are a ubiquitous signature and therefore necessary for substorm onset. However whether the instability is initiated locally in the near-Earth tail, or due to the effects of reconnection in the distant tail remains to be determined. Well-defined azimuthal structuring exists within most substorm onset arcs, and grows exponentially before the large-scale classical 'Akasofu' onset. This implies that a magnetospheric instability is active during the overwhelming majority of substorms in the minutes preceding global auroral brightening.

It has been shown on multiple occasions that the substorm onset arc is embedded within closed field lines in the inner magnetosphere e.g., [*Samson et al.*, 1992b; *Murphy et al.*, 2012, 2014]. The open-closed field line boundary is defined by the poleward edge of the electron aurora [*Blanchard et al.*, 1995], which is significantly poleward of the substorm onset arc and presumably conjugate to the tail reconnection site. Auroral substorm onset occurs near the peak in the proton aurora, which is conjugate to the location where the magnetospheric magnetic field topology changes from dipolar to tail-like and pressure gradients develop [*Samson et al.*, 1992b]. Hence, this is also the region where the magnetotail is most unstable to, for example, Shear-Flow Ballooning Instability [*Voronkov et al.*, 1997]. As demonstrated here, auroral beads, the ionospheric projection of the substorm onset instability, are observed prior to auroral substorm onset in over 70% of substorms, and during 90% of substorms within 2 minutes of onset. The high prevalence of beads suggests that the instability in the inner magnetosphere develops before the classical definition of substorm onset. No other mechanisms are able to reliably describe the repeated observation of periodic auroral beads observed azimuthally along the substorm onset arc. Our results demonstrate a fundamental link between substorm onset and the development of an inner-magnetospheric plasma instability.

We note here that the traditional notion of 'substorm onset', the time at which the substorm starts, is not necessarily a useful concept. This definition of a single time at which the substorm detonates is subjective, and does not describe the physical processes which eventually lead to a large-scale substorm. However the concept of an 'onset window' during which auroral beads start to grow exponentially prior to auroral breakup is much more useful, allowing us to understand more about the ubiquitous processes which happen prior to global auroral breakup

Prior to onset, bead power is located at low wavenumbers with small amplitude fluctuations. During the end of the substorm growth phase, more magnetic flux is piled in to an increasingly unstable system. Sources of free energy, e.g., a large-scale pressure gradient, velocity shears, temperature anisotropies allow quasi-stable waves to grow and the instability to be initiated. This can be observed in the aurora by exponential growth of auroral bead amplitudes during the linear stage of the instability [*Rae et al.*, 2010; *Kalmoni et al.*, 2015]. Statistically, the instability simultaneously excites exponentially growing waves over a wide range of spatial scales. *Rae et al.* [2010]; *Kalmoni et al.* [2015] demonstrate that in individual events specific wavenumbers grow faster than others, allowing a comparison between observational instability characteristics and predictions made by simulations and theory, e.g., *Voronkov et al.* [1997]; *Lui* [2004].

Auroral beads have previously been considered to be a 'special case' or statistical outlier, and not a common signature of the substorm onset process. However, auroral beads are typically reported when the bead intensity is much larger than the background arc intensity, and so they are easily identifiable on visual inspection, hence they have been under-reported prior to this study. We show that characteristic spatial scales can be identified in the vast majority of all observations with quantitative analysis, thus auroral beads should not be considered a special case, rather a common feature in the auroral substorm sequence. In Figure 5.6 we demonstrate that, in the majority of cases studied, the bead amplitude is less than 10% of the background arc intensity. A lower ratio of bead amplitude to arc amplitude makes these characteristic spatial

scales more difficult to identify without quantitative analysis, and this explains why auroral beads have not been previously reported as a regular feature of onset arcs.

Bead signatures can be extremely low amplitude (Figure 5.6), sometimes constituting only ~ 40 raw counts by the ASI (only 1% of the background arc intensity). The processes which result in auroral beads, and indeed what processes create the substorm onset arc, are unclear. However, we show here that bead amplitudes grow exponentially which is a classic signature of the linear stage of an instability. What process or processes drive this particular instability, how magnetosphere-ionosphere coupling operates, and how the beads relate to the substorm onset arc are all open questions that arise from our hypothesis that beads are ubiquitous to substorm onset arcs.

We note here that the spatial resolution and sensitivity available from the THEMIS ASIs may not always resolve the required spatial scales for beads to be resolved. Although the spatial resolution of the THEMIS ASIs corresponds to ~ 1 km at zenith, this resolution becomes much lower towards the horizon. At the spatial and temporal resolution of the ASIs a beading onset time was identified for 90% of events, with 70% of events prior to auroral substorm onset. We propose that higher spatially resolved and more sensitive auroral measurements would demonstrate that beads are a universal signature along the onset arc. Hence, a plasma instability is active in the inner magnetosphere and therefore an integral component of the substorm process during all substorms.

5.5 Conclusions

In this work we have presented detailed auroral analysis of the spatial structuring and dominant scales of ~ 200 independently identified substorm onset arcs. We show that in at least 90% of events studied auroral beads are observed along the onset arc in the minutes surrounding substorm onset. Auroral beads are statistically be observed ~ 2 minutes before auroral onset at low spatial scales and are the signature of a quasi-stable waves which exist in

the near-Earth magnetosphere on closed field lines. Around auroral onset the waves start to grow exponentially over a wide range of spatial scales, this is characteristic of the linear stage of the instability [*Rae et al.*, 2010; *Murphy et al.*, 2014; *Kalmoni et al.*, 2015]. During the transition from pre- to post onset times the consistent median statistical characteristic spatial scale of the instability throughout the analysis are indicative that a single instability is active at these times, or multiple instabilities which grow over a similar range of spatial scales making it impossible to differentiate them using this technique. Previously auroral beads have been under-reported, because the bead amplitude is typically less than 10% of the background arc intensity and are thus difficult to identify without quantitative analysis techniques. This is consistent with the substorm onset arc being either created, or perturbed, by an instability in the equatorial inner magnetosphere, which precedes auroral break-up by several minutes. In-situ measurements are required to investigate this, and determine whether the instability is initiated via external energy sources or locally at the near-Earth edge of the plasma sheet

Chapter 6

Using Multi-Spectral Observations to Determine the Drivers of Substorm Onset Aurora

In Chapters 4 and 5 we focused on data from white-light imagers, which primarily respond the the green-line (557.7 *nm*) auroral emission. However in this data chapter we perform our along-arc analysis techniques on data from the Multi-spectral Observatory Of Sensitive EM-CCDs (MOOSE) imagers at Poker Flat, Alaska, in order to investigate how signatures of beads vary in different auroral emission lines, and hence determine the characteristic energy of electrons incident on the ionosphere (e.g., *Rees and Luckey*, 1974). Using multi-spectral data allows the investigation of the auroral acceleration processes which drive auroral beads, and hence the substorm onset aurora.

For this case study, the imager setup consisted of 3 co-located ASIs with a 3.3 Hz cadence producing 512×512 pixel images, rendering a spatial resolution of $\sim$ 500 m per pixel at zenith, compared to the 0.33 Hz cadence and $\sim$ 1 km spatial resolution of the THEMIS ASIs. Additionally, each MOOSE ASI has a spectral filter to allow the individual auroral emission lines with wavelengths 630.0 nm, 557.7 nm and 427.8 nm to be sampled. Also, a narrow-field (19^o) imager with a 40.7 Hz cadence is pointed at magnetic zenith, providing unprecedented coverage of the substorm aurora (see Section 3.2 for further information on the MOOSE imagers). This imager has a spatial resolution

of $\sim$ 126 m per pixel, allowing small-scale structures to be resolved. The multi-spectral imagers provide us with key information regarding the auroral acceleration processes which generate auroral beads. Increased spatial ($\times$2) and temporal ($\times$10) resolution ASI data, in comparison to the THEMIS ASIs (and much higher for the narrow-field imager), also allows us to study whether smaller, previously unresolvable, spatial scales are present along the substorm onset arc or whether the lower resolution data from presented in Chapters 4 and 5 is sufficient to fully resolve substorm aurora dynamics.

6.1 Introduction

A magnetospheric substorm can be remotely observed from the aurora by the brightening and poleward expansion of the most equatorward arc or the sudden formation of an arc, located in the midnight sector of the auroral oval [*Akasofu*, 1964]. Auroral breakup is directly associated with the onset of a substorm, but the exact cause of auroral breakup, and how it relates to the magnetospheric processes associated with a substorm are not well understood.

The origins of the pre- and post- substorm aurora have been researched in depth, including where in the magnetosphere they map, and the auroral acceleration processes responsible. Using conjugate Fast Auroral SnapshoT (FAST) Explorer [*Carlson*, 1992] and THEMIS ASI observations, *Jiang et al.* [2012] found that the pre-existing auroral arc is consistent with electrons accelerated by a static potential drop, and is embedded within the proton aurora. This is in agreement with *Deehr and Lummerzheim* [2001] who found that the substorm onset arc also maps slightly poleward of the peak in proton aurora. The peak in proton aurora (Hβ emission) maps to the transition region between stretched and dipolar magnetic field lines in the magnetotail [*Samson et al.*, 1992a], hence the substorm onset and pre-existing arcs observed by *Deehr and Lummerzheim* [2001]; *Jiang et al.* [2012] respectively map slightly tailward of this region.

A study of simultaneous observations of an auroral substorm using FAST and IMAGE-Far UltraViolet (FUV) imager data by *Mende et al.* [2003] found

that the poleward surge of the substorm aurora, roughly $\sim$ 1 minute after onset was consistent with Alfvén wave-accelerated electrons. However the energy spectrum of the electrons responsible for the aurora equatorward of the surge were consistent with accelerated by quasi-static "inverted V" electric fields.

Taken together, these results suggest that the pre-existing and substorm onset arc may be accelerated by different mechanisms.

Both global space-based imagers and ground-based ASIs have also enabled multiple observations of auroral beads aziumthally along the substorm onset arc, in the minutes prior to substorm onset e.g., *Henderson* [1994]; *Friedrich et al.* [2001]; *Henderson* [2009]; *Kepko et al.* [2009]; *Sakaguchi et al.* [2009]; *Rae et al.* [2009a,b, 2010]; *Motoba et al.* [2012]; *Murphy et al.* [2014]; *Kalmoni et al.* [2015]. These signatures have been shown to grow exponentially, and hence are consistent with an instability [*Rae et al.*, 2010; *Kalmoni et al.*, 2015]. Auroral beads were thought to be part of a '*special case*' of substorm, however in the previous chapter we show that they are a common signature which form along the substorm onset arc in the minutes prior to the vast majority, if not all, substorm onsets.

Auroral beads have been linked to the onset of ULF waves, e.g., *Rae et al.* [2009b]. Also, *Newell et al.* [2009] showed that the power of Alfvén wave-accelerated aurora increased by 182% in comparison to quiet times, more than any other type of aurora. Hence, waves are clearly an important, if not vital, component of the substorm onset process.

Voronkov et al., [1997; 2000] propose the Shear-Flow Ballooning Instability (SFBI) as a possible explanation for observations of auroral beads (discussed in detail in Section 2.7.1.3). The SFBI is a hybrid instability between the Kelvin-Helmholz (KH) instability due to a small-scale shear flow, and the Rayleigh-Taylow instability due to a large-scale Earthward pressure gradient in the magnetotail. *Voronkov et al.* [1997] suggest that initially a magnetospheric shear flow vortex grows from a narrow shear-flow in the magnetotail. After the KH instability saturates and becomes nonlinear, the ballooning mode is subsequently driven, which can grow to amplitudes at higher rates than a simple KH instability. Using the CANOPUS project [*Rostoker et al.*, 1995] ASI

and Meridian Scanning Photometer (MSP) data set, *Voronkov et al.* [2000] studied large-scale auroral vortices observed during a substorm growth phase, expansion phase onset and psuedo-breakup and compared these observations with the characteristic of the SFBI. The auroral arcs, which develop into vortices, formed on the poleward boundary of the proton aurora (Hβ emission, 486.1 nm) and on the equatorward boundary of the electron aurora. This is the region in the magnetosphere where the magnetic field topology transitions form dipolar to stretched [*Samson et al.*, 1992a] Other instabilities such as the Cross-Field Current Instability (CFCI, *Lui*, 2004 and references therein) have also been proposed to destabilise the inner-magnetosphere during a substorm. The CFCI has been shown to be consistent with auroral beads in a thin plasma sheet when the IWI mode is suppressed and when the relative velocities between ions and electrons is low [*Kalmoni et al.*, 2015; *Lui*, 2016].

The physical processes in the magnetosphere which lead to the generation of auroral arcs are yet to be determined [*Denton et al.*, 2016]. However it is highly likely that the processes which result in auroral arcs and auroral beads, the regions where they map to, the acceleration processes which energise precipitating particles up to auroral energies, and the magnetospheric processes which constitute the substorm are inextricably linked. As we have already seen, substorms coincide with the onset of ULF waves as measured from the ground (e.g., *Murphy et al.*, 2009; *Rae et al.*, 2009b] and space [e.g., *Rae et al.*, 2009a; *Walsh et al.*, 2010) which also agrees with the hypothesis that the substorm aurora are Alfvén-wave driven (e.g., *Mende et al.*, 2003). In this study we are able to investigate the nature of the substorm onset arc and auroral beads for the first time, with unprecedented data from the MOOSE imagers, by performing the same analysis on auroral data in multiple wavelengths.

6.2 Experimental Set-Up

Auroral observations were taken with the MOOSE imagers (see Section 3.2 for further details). The set-up consisted of 3 All-Sky Imagers with filters for the red aurora (630.0 nm), which is typically observed around $150 - 200$ km

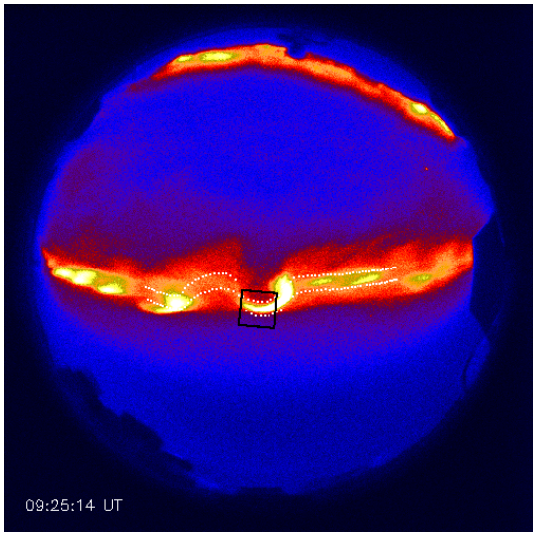

Figure 6.1: Data from 557.7 nm (green) MOOSE imager ASI at 09:25:14 UT on 18 September 2012 during the evolution of auroral beads during an auroral substorm. The edges of the identified arc, found by an arc-finding algorithm, are indicated by white pixels. The field-of-view of the narrow-field imager is indicated by the black box.

altitude, the green aurora (557.7 nm), at $\sim$ 110 km altitude and the blue aurora (427.8 nm) at $\sim$ 90 km altitude, and a high resolution narrow-field imager at magnetic zenith. A broadband Schott BG3 filter is used on the narrow-field imager, which selects prompt emissions, e.g., blue-line aurora, (see *Samara et al.*, 2012; *Michell et al.*, 2012). The field of view of the narrow-field imager in relation to the ASIs is shown by the black box in Figure 6.1. The white arc-outline was found using an arc-finding algorithm which is described in the following section.

6.3 Analysis Techniques

In this study the analysis techniques used are largely similar to those used in previous chapters. However in the following section we briefly outline the techniques used, any changes from previous chapters, and additional techniques developed specifically for this data-set, prior to presenting the results in Section 6.4.

6.3.1 Arc Identification

The arc finding algorithm is very similar to the one used for the analysis in Chapter 5: the location of the arc in latitude is found by fitting a Gaussian to each longitudinal slice to account for the equatorward and poleward propagation of the arc during the late growth and early expansion phase, and for possible latitudinal skewing of the arc [*Gillies et al.*, 2014] prior to auroral breakup.

However for the analysis presented in this chapter we use a more sophisticated algorithm [*K.R. Murphy, personal communication*][1] The main differences are:

- If the arc cannot be detected at a particular time and longitude, the algorithm uses the previous arc location as a seed for the new Gaussian fit. This makes it easier to identify a section of the arc if it has faded relative to the previous image.
- The auroral arc can be tracked backwards in time. Due to the inherent nature of auroral brightening during substorm onset, the auroral arc at a later time is brighter, making it much more easily identifiable by a Gaussian-fitting algorithm. When the arc is tracked from a later time, together with using the previous location to seed a new fit, the arc can be tracked much longer than tracking forwards in time. This allows us to study the formation and scales of auroral beads much earlier than was possible in previous studies.

An example of the arc location, identified using this algorithm is shown by the white pixels in Figure 6.1.

6.3.2 Along-Arc Keogram and Power Spectral Density

The techniques for creating an along-arc keogram and Power Spectral Density (PSD) are exactly the same as those outlined in Chapter 5. Prior to using Fourier analysis to identify the characteristic structuring of the onset arc, we

[1]The arc-finding algorithm developed by K.R. Murphy, and adapted by N.M.E. Kalmoni for compatibility with this data-set, has not been previously published

detrend the data using along-arc numerical differentiation (with respect to longitude) to remove the background auroral arc. The differentiated keogram contains the signatures of the beads only. Hence, we apply Fourier analysis in the longitudinal direction to each time point of the differentiated keogram, resulting in spatial Fourier spectrum, which varies in time, as in Chapters 4 and 5. However, as we perform the analysis on the differentiated keogram this results in a whitened PSD, i.e., multiplied by a factor of k^2. The whitened PSD gives the appearance of higher spatial scales having significantly higher amplitudes and therefore may broaden the appearance of any peaks in power. The whitening of the PSD is an unavoidable effect of using numerical differentiation as our background removal technique.

6.3.3 Data Calibration and Electron Energy Estimation

The auroral data was calibrated by analysing the ASIs' response to total darkness, known background stars and estimations of atmospheric effects [*Grubbs*, 2016; *Grubbs et al.*, 2016], allowing for direct comparisons to be made between the data from the different emission lines. The calibration techniques used are outlined in detail more in Section **??**.

An inversion technique developed by [*Grubbs*, 2016] together with the calibrated auroral intensity ratios [*Grubbs et al.*, 2016] for the different optical wavelengths is used to estimate a characteristic energy of precipitating electrons which cause these auroral emissions using the GLobal AirglOW (GLOW) model [*Solomon*, 1989, 2001], also described in more detail in Section **??**.

6.3.4 Small-Scale Feature Identification

As will be seen in the subsequent results section (Section 6.4), the narrow-field imager, which is pointed at magnetic zenith and whose field of view is outlined in Figure 6.1, is able to detect small-scale substructure of auroral beads. As these structures can be very faint, and are not necessary closely aligned with geomagnetic longitude, it is not possible to use the arc-finding algorithm to analyse them.

Instead, we use a spatial bandpass filter and feature finding algorithm from

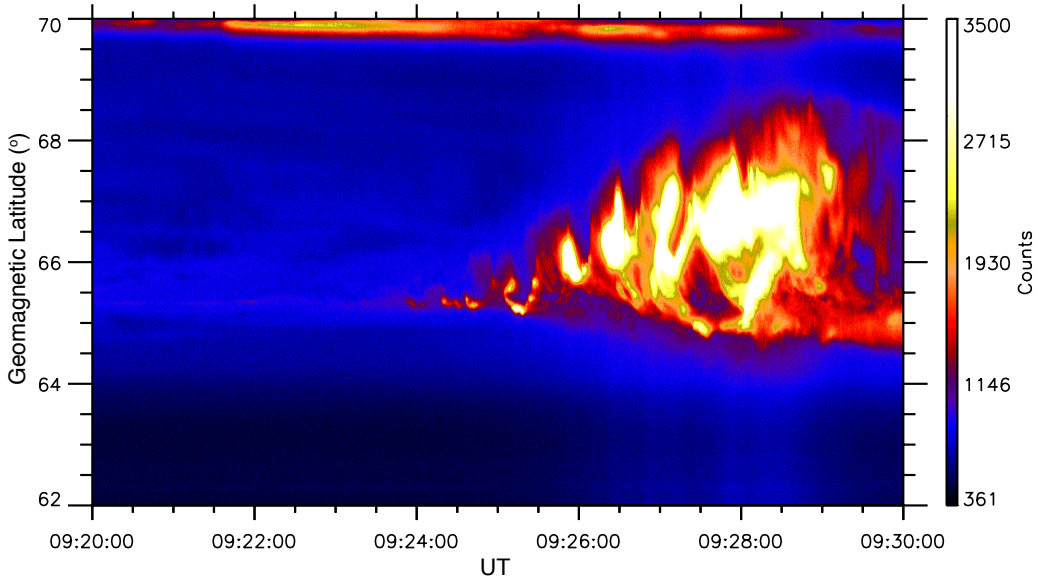

Figure 6.2: North-South keogram of a substorm on 18 September 2016 observed at 09:20:00 - 09:30:00 UT. The keogram is generated by taking a slice through the centre of the green-line MOOSE All-Sky Imager at Poker Flat, Alaska.

the Emory IDL Library[2] [*Crocker and Grier*, 1996] on the narrow-field-of-view images. The spatial bandpass filter removes the stars from the original data. The feature finding algorithm requires an approximate size of the features of interest, hence removing the ability to detect structures on other scales. However this tool does allow automated, and reproducible classification of auroral bead substructure, rather than visual and subjective identification.

6.4 Results

On 18 September 2012 an isolated substorm was observed near the zenith of the 3 MOOSE ASIs and the Narrow-field imager at Poker Flat, Alaska. Figure 6.2 shows a north-south keogram of the event through the centre of the green-line ASI. The keogram shows the brightening of a pre-existing arc at 09:24:00 UT close to the equatorward edge of the diffuse aurora, shown by the increased auroral intensities at latitudes between $\sim 65.0° - 70.0°$ geomagnetic latitude prior to 09:24:00 UT. The arc brightens, followed by a rapid poleward expansion of the aurora around 09:25:00 UT. This results in large-scale auroral

[2]The Emory IDL library can be found at http://www.physics.emory.edu/faculty/weeks//idl/

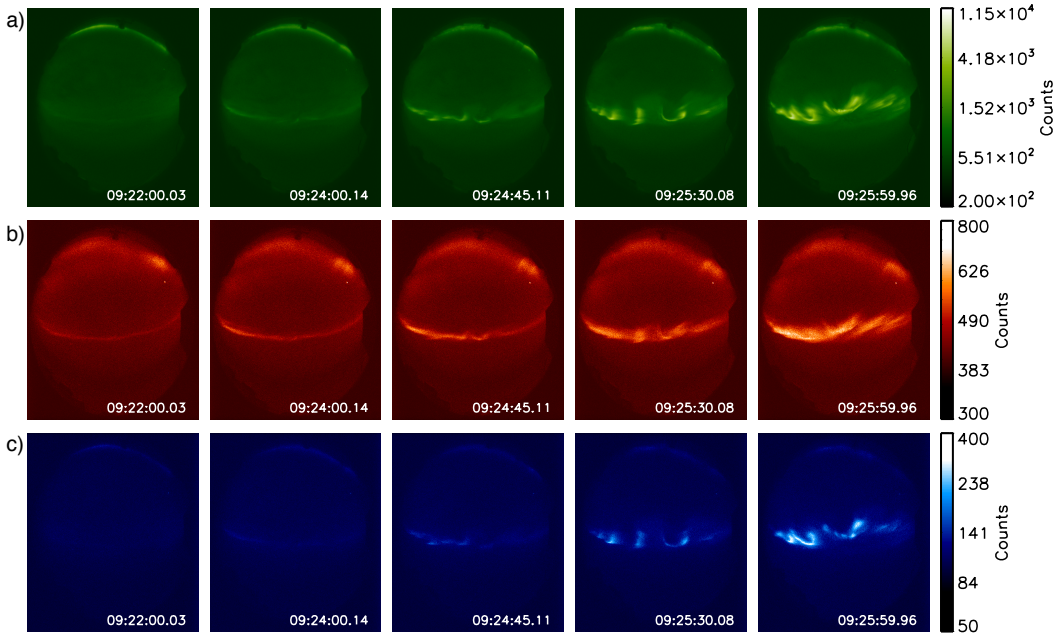

Figure 6.3: The raw, uncalibrated data of auroral observations obtained by green (557.7 nm), red (630.0 nm) and blue (427.8 nm) aurora during a substorm on 18 September 2012 at 09:22:00 - 09:26:00 UT observed from Poker Flat. The images shown in the different emission lines were taken at the same time, allowing the differences between the different aurora to be compared.

breakup, where the auroral expands from the initial arc geomagnetic latitude of $\sim 65.5°$ to at least 68.5°.

A summary of the auroral substorm observations in 557.7 nm (green, *a*), 630.0 nm (red, *b*) and 427.8 nm (blue, *c*) in is presented in Figure 6.3. Prior to onset, substorm onset arc, is most-clearly visible in 630.0 nm (Figure 6.3*b* at 09:22:00 UT). However, when observed in the 557.7 nm, the arc appears much fainter, and is embedded within diffuse aurora visible both from the North-South keogram shown in Figure 6.2 and the raw data (Figure 6.3*a* at 09:22:00 UT). The auroral arc cannot be observed in the 427.8 nm at this time (Figure 6.3*c*).

By 09:24:00 UT the auroral arc in 630.0 nm has widened, and brightened significantly from $\sim 400 - 500$ Counts. The arc is very faint, but resolvable, in 557.7 nm, and barely visible in 427.8 nm. Close inspection of the arc in both in 557.7 nm and 630.0 nm at 09:24:00 UT shows a very faint signature of azimuthal structuring (beads) of the onset arc at zenith of the ASI. At 09:24:45 UT, azimuthal structuring is undoubtedly observed all along the arc,

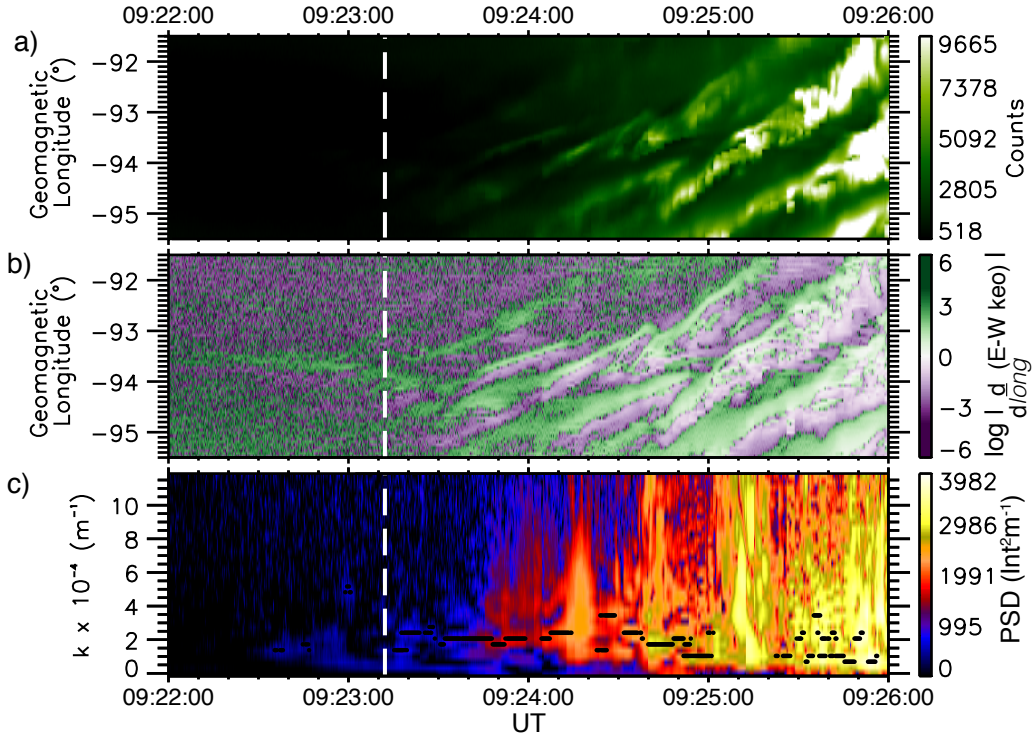

Figure 6.4: Quantitative analysis of along-arc structuring using arc-finding algorithm between 09:22:00 - 09:26:00 UT. *a*) The along-arc keogram of the green-line auroral data showing along-arc auroral intensity as a function of geomagnetic longitude and time. *b*) The spatial differential of the along-arc keogram with respect to geomagnetic longitude as a function of time on a logarithmic scale. *c*) The power spectral density calculated form the Fourier transform of the differential keogram in the longitudinal direction.

including very faintly in the 427.8 nm data. In the later frames at 09:25:30 UT and 09:26:00 UT the beads are visible in all emission lines, however they appear more blurred in the red-line due to the longer emission life-time of the red aurora. The onset arc expands poleward and breaks up around 09:26:00 UT, at which point the arc can no longer be tracked.

By using the arc-finding algorithm detailed in Section 6.3.1, the location in latitude and longitude of the arc in 557.7 nm (green) is tracked as from 09:22:00 UT − 09:26:00 UT. In Figure 6.4*a* we show the along-arc keogram for this time range of the 557.7 nm aurora. The beads which are propagating along the arc in the eastward direction can be identified by the repeating patterns moving to higher longitudes (eastward). The along-arc keogram is detrended by using a spatial differentiation of the keogram with respect to longitude, shown in Figure 6.4*b* and discussed in Section 6.3.2. The spatial differentiation

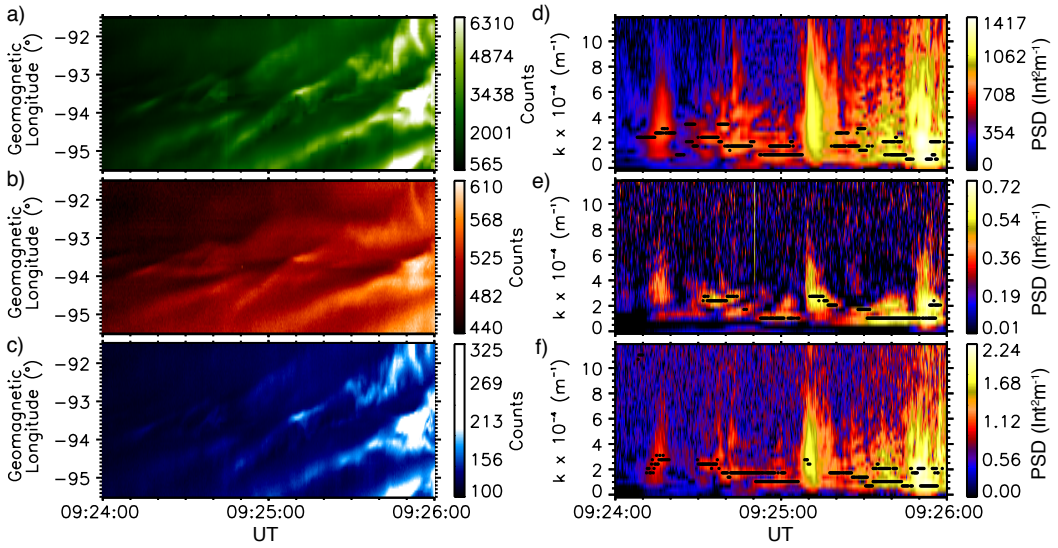

Figure 6.5: Quantitative analysis of along-arc structuring in green, red and blue emission lines between 09:24:00 - 09:26:00 UT. (*a* - *c*) The along-arc keograms for the green-, red-, and blue-line data respectively. (*d* - *e*) The respective power spectral densities calculated from the differential along-arc keograms, which are not shown in this figure. See Figure 6.4*b* for an example.

of the keogram with respect to longitude allows the initial formation of low amplitude beads to be observed by detrending the original keogram. The PSD of the differentiated along-arc keogram is calculated using a Fourier transform in the longitudinal direction, as shown in Figure 6.4*c*. Here we note that the Nyquist wavenumber of this analysis is $k_{Nyquist} \approx 12 \times 10^{-4}$ m^{-1}, which is much higher than the Nyquist wavenumber of this analysis performed in previous chapters due to the increased spatial resolution of the MOOSE ASIs in comparison to the THEMIS ASIs. The formation of the beads can be identified as a clear increase in power spectral density at low spatial scales, initially at $k \approx 2 \times 10^{-4}$ m^{-1} at ∼09:23:10 UT and subsequently reducing to $k \approx 1 \times 10^{-4}$ m^{-1} around ∼09:25:00 UT. The characteristic spatial scales identified using the same criteria as outlined in Section 5.2.4 are shown by the black dots. From the identified characteristic spatial scales we determine a beading onset (also defined in Section 5.2.4), at 09:23:12 UT, which is shown by the white vertical dashed line in the plot.

The auroral arcs for 630.0 nm (red) and 427.8 nm (blue) emission lines were also found using the arc-finding algorithm. This is necessary because the different emission wavelength emit at different altitudes. Hence, in an ASI

field-of view this means the arc appears to be in a slightly different location. The 557.7 nm and 630.0 nm auroral arcs were able to be tracked as early as 09:22:00 UT. However the auroral arc in 427.8 nm was only trackable after 09:24:00 UT as we were unable to detect it prior to this time.

Figure 6.5 shows the along-arc keograms and respective PSDs of the 3 different emission lines between 09:24:00 − 09:26:00 UT, to allow a direct comparison between the different spectral lines. The PSD is calculated by the Fourier transform of the differentiated along-arc keogram (as is demonstrated in Figure 6.4, however this intermediate step to detrend the data is not shown in Figure 6.5). The keograms of the 557.7 nm (green), 630.0 nm (red) and 427.8 nm (blue) aurora (Figure 6.5*a-c*) show that the beads, the repeating parallel features, approximately follow the same eastward trajectories along the arc during this time interval, and hence confirm that the beads are observable in all 3 emission lines. In particularly the 557.7 nm and 427.8 nm emission appear very similar, as they are both relatively prompt, and localised in emission altitude at $\sim$ 110 km and $\sim$ 90 km respectively. The repeating signatures of the beads in 630.0 nm are more blurred, presumably due to the much longer emission life-time of $\sim$ 110 s of the atomic Oxygen electron transition which results in the emission of a 630.0 nm wavelength photon. The extended emission life-time means that the Oxygen atoms can travel a significant distance before they re-emit a photon, hence 'blurring' the signature of the beads. Despite this, the beads are still identifiable in the original red-line data and along-arc keogram.

Comparatively the PSD of the keograms has a very similar pattern for all wavelengths with most of the power located at low wavenumbers. The characteristic spatial scales identified in each data-set are remarkably similar. At specific times this PSD spreads to a broadband peak over a wide range in wavenumbers. This coincides when an individual bead moves through the centre of the field of view of the ASI, and hence may be due to spatial aliasing of possible bead sub-structuring only visible at magnetic zenith.

As outlined in Sections **??**, 6.3.3, the raw data from the MOOSE ASIs shown in Figure 6.3 was cross-calibrated between the 3 separate ASIs and

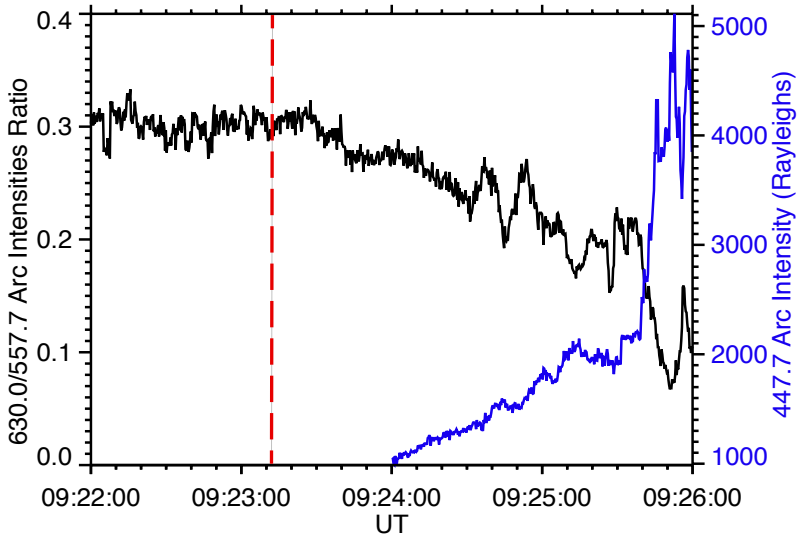

Figure 6.6: The ratio of median auroral arc intensity in 630.0 nm and 557.7 nm shown in black. The ratio is approximately constant at 0.3, then reduces after ∼09:23:25 UT. The median arc intensity 427.8 nm is shown in black, however this data was only available after 09:24:00 UT. The vertical line shows the time beads are first detected along the substorm arc at 09:23:12 UT, as indicated in Figure 6.4.

spectral filters, allowing a direct comparison between the observations from the different cameras. Using the calibrated data, the temporal evolution of the median arc intensity is used to estimate the change in characteristic electron precipitation energy by using the ratios of auroral intensity form the different emission lines, in a similar way to the electron inversion map in Figure 3.6 [*Grubbs*, 2016]. The median arc intensity in the 630.0 nm aurora is used as an estimate for low energy electron precipitation, and the arc intensity of the 557.7 nm aurora for high energy electron precipitation.

In Figure 6.6 we show the ratio of the median arc intensity of 630.0/557.7 as an indicator of the characteristic energy of the precipitating electrons. The ratio remains relatively constant at 0.3 between 09:22:00 UT to ∼09:23:25 UT. When compared to the energy inversion map from *Grubbs* [2016] shown in Figure 3.6, a ratio of 0.3 suggests a characteristic electron energy < 1.0 keV, corresponding primarily to low energy 630.0 nm aurora. However after ∼09:23:25 UT the ratio starts to decrease, suggesting an increase in the characteristic energy of precipitating electrons. The time at which the decrease commences is remarkably similar to time auroral beads are first identified

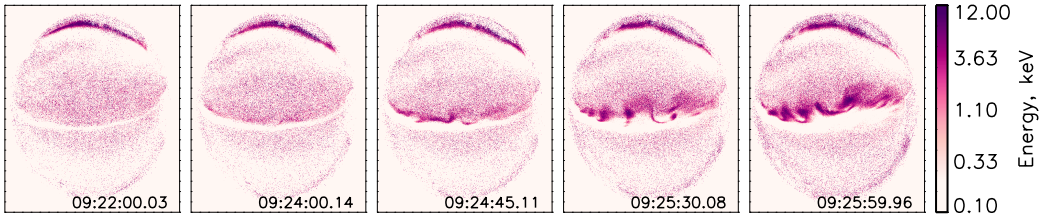

Figure 6.7: Precipitating electron energies derived from the GLOW model for the same time intervals as shown in Figure 6.3

along the substorm onset arc at 09:23:12 UT. The time at which beads were first identified along the arc from the 557.7 nm PSD, shown in Figure 6.4, 09:23:12 UT, is indicated in Figure 6.6 by the dashed vertical red line. The slight discrepancy between the timings could be attributed to the initial beads forming locally at zenith along the arc, whereas the ratios are calculated from the median of the intensity of the full extent of the arc. The ratio drops to its lowest value of ~ 0.07 at $\sim$09:25:50 UT meaning the characteristic energy of the auroral electrons is higher, and according to the energy inversion map corresponds to a characteristic precipitating electron energy of ~ 2.5 keV. The median 427.8 nm arc intensity is also shown in Figure 6.6 between 09:24:00 UT − 09:26:00 UT (prior to 09:24:00 UT the arc-tracking algorithm was unable to detect an arc). The intensity of the 427.8 nm aurora is commonly used as an indicator of total precipitating electron energy flux, and follows a very similar (but opposite) trend of the 630.0 nm/557.7 nm auroral ratio. This is because the 630.0 nm/557.7 nm ratio of is inversely proportional to the characteristic energy of the precipitating electrons, and hence confirming that it is likely that there is an increase in characteristic precipitating electron energy during this interval.

The calibrated auroral intensity for the different optical wavelengths were then used to estimate the characteristic energy of electron precipitation using the inversion technique [*Grubbs*, 2016] of the GLOW model. Figure 6.7 shows the characteristic electron precipitation energies obtained from GLOW [*G. Grubbs, personal communication*]. It must be noted that these results should only be used as a qualitative indication of a change in precipitating particle energies, as there were no in-situ conjunctions during this event allowing for

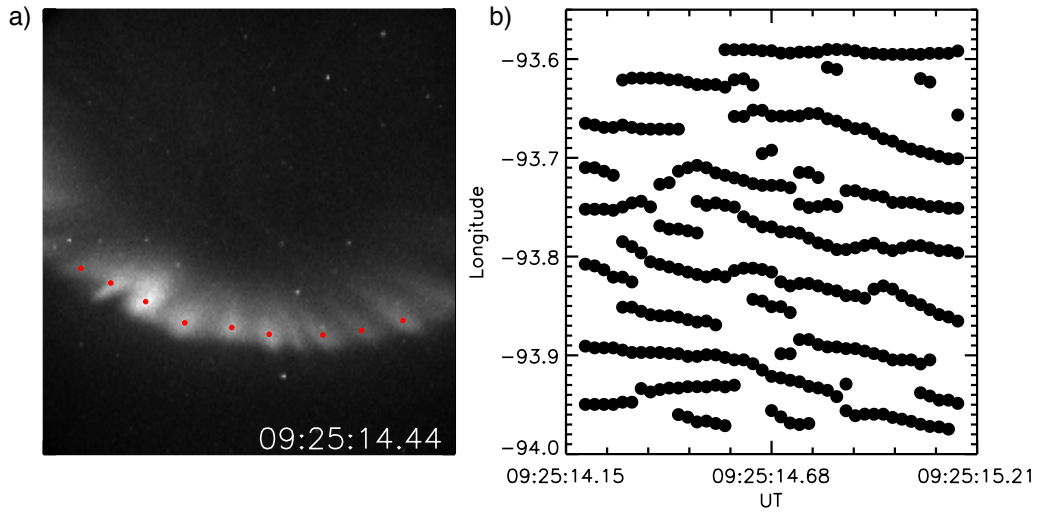

Figure 6.8: (*a*) Narrow-field data from an auroral bead at zenith at 09:25:14.44 UT. Locations of mini-beads identified using the Emory Library are indicated by the red dots. (*b*) Locations of mini-beads as a function of geomagnetic longitude between 09:25:14.15 - 09:25:15.21 UT showing westward propagation.

calibration of electron energies with the model. As expected from the arc intensity ratios in Figure 6.6, the results from GLOW also show a general increase in characteristic energy of the electrons precipitating into the arc and auroral beads. In Figure 6.7 at 09:22:00 UT a clear depletion in electron energy in the region where the auroral arc is most clearly visible in the red-line aurora, with electron energies of < 0.8 keV. At 09:24:00 UT a slight increase in the electron energies $\sim 1 - 3$ keV becomes visible. In the subsequent panels of Figure 6.7, the energy of the arc electrons continues to increase, with the estimated energies extending up to 12 keV. It also becomes more obvious that there is higher energy electron precipitation at the centre of the beads, than in the rest of the arc. This is also observed during in-situ observations of precipitating electrons within beads by the Cascades2 sounding rocket observations [*Lynch et al.*, 2012]. It is currently unclear whether the region slightly equatorward of the arc which shows a depletion in characteristic precipitating electron energy for the duration of the analysis is a real result, or an artefact of the inversion technique, and so we make no conclusions based on this depletion.

The narrow-field imager, which is pointed at magnetic zenith (indicated in Figure 6.1), is perfectly positioned to observe beads travel through its field

of view prior to auroral breakup. A time where a bead moves through the field of view of the narrow imager is shown in Figure 6.1. In Figure 6.8*a* we present the data from the narrow-field imager at 09:25:14.44 UT, the same time when the auroral bead in Figure 6.1 moves through the field of view. Sub-structure is clearly visible within the larger bead, we term these 'mini-beads'. A similar signature was observed as other beads travelled through the field of view of this camera, however at this time the sub-structure was clearest and we were able to track the motion of the mini-beads. We used the spatial bandpass filter and feature finding algorithm from the Emory IDL Library [*Crocker and Grier*, 1996] on the images. The location of mini-beads were tracked for roughly 1 s of data between 09:25:14.15 - 09:25:15.21 UT. An example of the mini-bead locations found using the Emory analysis tools are indicated by the red dots plotted over the data observed by the narrow-field camera in Figure 6.8*a*, showing a good agreement between the mini-beads, and the locations found by the Emory feature finding algorithm. This allowed the locations of the mini-beads to be found as a function of time, the result of which is shown in Figure 6.8*b*. The spacing of the mini beads of roughly $0.3^\circ - 0.5^\circ$ in geomagnetic longitude, corresponding to a bead spacing of $1 - 2$ km in the ionosphere at 100 km altitude, corresponding to only 2-3 pixels at zenith of the ASIs. Even though we are unable resolve the mini-beads explicitly in the ASI data, the sharp spikes in PSD across a wide range of spatial scales visible in Figure 6.5*d-f* may be due to the spatial aliasing of this sub-structure when the beads move across zenith of the ASIs.

From the identified locations of the mini-beads in subsequent frames it is clear that they are propagating in the westward direction, to lower longitudes. This is in the opposite direction to the propagation of the large-scale beads, which propagate in the eastward direction along the arc. Observations show that the intensities of the individual mini-beads do not change significantly on timescales of the cadence of the imager (40.7 Hz, i.e., 1 frame every ~ 0.025 s) and over the 1 s duration that the mini-beads were tracked for.

6.5 Discussion

We present observations of a substorm onset arc at the centre of the field of view of the MOOSE ASIs. The substorm aurora were observed in unprecedented temporal and spatial resolution, at multiple auroral wavelengths and also through a narrow-field-of-view imager to reveal sub-structure of auroral beads. Our observations shows a clear change in the nature of the substorm onset arc in the minutes prior to auroral breakup and the large-scale increase in auroral intensity.

During this event, our observations of the 630.0 nm (red), 557.7 nm (green) and 427.8 nm (blue) aurora initially show that the substorm onset arc is primarily visible in 630.0 nm aurora, with a very faint signature of the arc is also visible in 557.7 nm aurora. It has long been established that auroral signatures in different emission lines correspond to electrons with different energies precipitating into the ionosphere. For example, the 630.0 nm aurora are typically associated with the precipitation of low energy electrons of < 1 keV, whereas the 557.7 nm aurora is caused by higher energy electrons of < 10 keV [*Rees*, 1963]. Observations of an auroral arc in a single wavelength are therefore as a result of the precipitation of a narrow range of electron energies. In this case, where the auroral arc is visible mostly in 630.0 nm, these electrons are expected to have low energies. This observation is consistent with *Jiang et al.* [2012], who report that, using in-situ FAST measurements, the pre-existing auroral arc is caused by the precipitation of low-energy (< 1 keV), monochromatic electrons, which are accelerated by quasi-static, field-aligned electric fields.

Ratios of the aurora in different wavelengths have been used as an indication of the characteristic energy of the precipitating electrons which cause the auroral signature (e.g., *Rees and Luckey*, 1974; *Grubbs*, 2016). The ratios of the calibrated 630.0 nm and 557.7 nm auroral arc intensities [*G. Grubbs, personal communication*], initially show (between 09:22:00 UT − 09:23:25 UT), that the ratio is approximately constant at 0.3. From the energy inversion map in Figure 3.6, this approximately corresponds to a characteristic electron energy of < 1 keV and explains why the arc is primarily visible in the 630.0 nm

auroral emission. Hence, the stable ratio during this time period, and the fact that the auroral arc is not easily identifiable in the 557.7 nm and 427.8 nm emission lines, suggests that the electrons are accelerated by a quasi-static potential drop.

However, after ∼09:23:25 UT, there is a change in both the raw spectrally-resolved data and the arc intensity ratios calculated for this event. From the raw data shown in Figure 6.3 it is apparent that after ∼09:24:00 UT the auroral arc becomes more easily distinguishable in the 557.7 nm auroral emission. The arc also becomes more easily visible in the 427.8 nm emission. This effect can also be observed in the reduction of the ratio of 630.0 nm/557.7 nm auroral arc intensity after ∼09:23:25 UT, suggesting that the characteristic energy of precipitating electrons increases after this time, as the ratio is inversely proportional to energy. Not only are the electron energies higher, the observations of the auroral arc in multiple auroral emissions also shows that the accelerated range of electron energies is broad ($< 1 - 10$ keV). Aurora which is caused by electrons with a wide range of energies i.e., 'broadband' aurora, are typically associated with Alfvén wave-driven auroral acceleration processes [*Johnstone and Winningham*, 1982; *Lotko*, 1986; *Keiling*, 2008]. This is consistent with in-situ FAST observations reported by *Mende et al.* [2003] who observed that the poleward surge of the substorm aurora, ~ 1 minute after substorm onset was consistent with Alfvén wave-accelerated electrons. However our observations are of the initial development of the substorm aurora, rather than minutes after substorm onset observed by *Mende et al.* [2003]. As is shown in Chapters 4 and 5, typically bead growth only lasts for $2 - 3$ minutes, so observations a full minute after substorm onset is a large fraction of this time, during which a lot can have changed.

Observations of auroral beads are detected almost simultaneously to the reduction in the 630.0 nm/557.7 nm auroral arc intensity ratio. Thus, the beads appear to form only along the wave-driven arc. The observations of beads in all three auroral emissions confirm that the beads are caused by a the precipitation of electrons with a range of energies, associated with wave-driven acceleration processes. Results from the GLOW model, shown in Figure 6.7

suggest that the electron energies are highest in the centre of auroral beads.

Observations by *Jiang et al.* [2012] conclude that the pre-existing auroral arc is driven by a quasi-static potential drop, as is the case for our substorm onset arc prior to ∼09:23:25 UT. However in this case-study we show that the beads along the onset arc are from wave-accelerated electrons. Hence, the substorm onset arc that is initially driven by a potential drop is subsequently driven unstable by waves, which are manifested in the formation of auroral beads along the onset arc. Furthermore, observations of the aurora in multiple emission lines, and an increase in the characteristic energy of auroral electrons, support this conclusion.

The formation of auroral beads along the substorm onset arc in the minutes prior to onset and auroral breakup have been studied in detail using multiple observations from both ground- and space-based datasets. *Motoba et al.* [2012] observed auroral beads from conjugate stations in the Northern and Southern hemisphere, indicating that they have a common driver in the magnetosphere. Together with observations that the substorm onset arc embedded within closed field lines, e.g., *Samson et al.* [1992b]; *Murphy et al.* [2012, 2014]; *Jiang et al.* [2012]; *Voronkov et al.* [2000]; *Deehr and Lummerzheim* [2001], and often within the proton aurora, the equatorward edge of which maps to the transition region between stretched and dipolar magnetic field configurations. *Rae et al.* [2010] present rigorous quantitative analysis of a case-study which provide unambiguous evidence that beads are driven by an instability.

Combining these findings leads to the conclusion that beads are driven by an instability at the near-Earth edge of the plasma sheet, where ions become demagnetised from the magnetic field when the plasma sheet is sufficiently thin. *Kalmoni et al.* [2015] and the results presented in Chapters 4 and 5 of this thesis confirm that the results presented by *Rae et al.* [2010] are repeatable in a small statistical study of 'beady-onset' arcs, and that these are also consistent with a plasma instability. In Chapter 5 we show that beads are actually an integral part of at least 90% of substorms, suggesting that a near-Earth instability is a fundamental part of the substorm onset process. In this Chapter we go further by confirming that in at least one case, the substorm onset arc

itself, and the beads embedded within it, are accelerated by wave-processes. This supports our conclusion that beads are driven by waves which go unstable, initiating the linear stage of an instability.

Finally, we also present unprecedented spatial and temporal resolution data of auroral beads, which uncovers substructure within the large-scale beads. There have been no previous observations of theses substructures within beads. However, *Semeter and Blixt* [2006] report perpendicular structuring of auroral arcs due to Alfvén wave dispersion. *Semeter and Blixt* [2006] also report that the thin arcs observed within the larger arc, appear to propagate in the opposite direction to the large-scale arc, which is the same in our observations of mini-beads propagating in the westward direction, whereas the large-scale beads propagate eastward along the arc. *Semeter and Blixt* [2006] conclude that their observations are consistent with theoretical predictions of shear Alfvèn wave dispersion, which predicts that the perpendicular group and phase velocity are oppositely directed. However it is difficult to conclusively determine whether the same processes drive the formation and evolution of the mini-beads observed, with only 1 s of high-resolution data in conjunction with ~ 4 minutes of lower resolution data.

6.6 Conclusions

In conclusion, we have observed a substorm in unprecedented temporal and spatial resolution as well as in multiple auroral emission lines. The data indicates that auroral beads form along the substorm onset arc at approximately the same time as the arc becomes visible in multiple wavelengths, indicative of broadband wave-acceleration. The auroral beads are also visible in all auroral emission lines observed. The ratios of the auroral arc intensity in the different wavelengths, suggest that the arc is initially excited due to a quasi-static potential drop. However the arc subsequently becomes Alfvénic at the same time as the auroral beads are first observed. We hypothesise that the arc observed has changed in nature during the onset process. Our conclusion is that an originally monoenergetic substorm onset arc is perturbed by the substorm on-

set process. Since substorm onset arc has been shown to be wave-driven, this affirms that wave-driven auroral processes take over as the dominant acceleration process in the creation of auroral beads and the large-scale substorm.

Chapter 7

Conclusions and Future Work

7.1 Conclusions

Ever since the substorm was first identified from auroral observations by *Akasofu* [1964], the magnetospheric processes and the sequence of events that lead to this dynamic auroral display have been violently disputed, and remain so to this day. The substorm is a key part in the fundamental interaction between the solar wind and the magnetosphere, however the lack of understanding of the important physical processes leading to this global disturbance hinder our ability to understand and predict the magnetospheric response to external driving. The substorm aurora are one of the key pieces to the puzzle and using the aurora allows us to document both the large and small-scale evolution of the processes leading to substorm onset, will help us eventually solve this fundamental magnetospheric interaction.

In this thesis detailed quantitative analysis uncovering the intricacies of the structuring of substorm onset auroral arcs is performed on data from ground-based auroral all-sky imagers. This work has determined that magnetospheric instabilities play a pivotal role in the substorm onset process. By using the all-sky imagers from the THEMIS mission, it has been possible to remote sense and place severe constraints on the type and characteristics of the magnetospheric instability. Furthermore, the instability has been quantitatively linked to auroral beads, and has been observed during at least 90% of

substorms. This has been achieved this in the following ways:

Previously, only *Rae et al.* [2010] had unambiguously shown that the signature of auroral beads were consistent with an instability from a single case study. A statistical study of auroral beading events was required to determine whether beads are commonly consistent with a plasma instability in the minutes prior to substorm onset. Hence, in Chapter 4 of this thesis, a detailed statistical study of substorm onset arcs which exhibited clear beading signatures during a subset of isolated substorms and pseudo-breakups was presented. In the minutes prior to the rapid brightening and poleward expansion of the aurora, regularly spaced auroral beads formed along the substorm onset arc. Fourier analysis techniques were used to show that a range of spatial scales exhibited exponential growth, which is the sign of the linear stage of a plasma instability. In order to gain some understanding on where this instability could be operation, an equilibrium magnetic field model was used to the majority of the auroral onset arcs studied to $9-12\mathrm{R}_E$. It was established that specific spatial scales exhibited higher growth rates than others, and compared my observations to simulations and theory of magnetospheric plasma instabilities proposed to play a part in the substorm onset process. Moreover it was possible to concluded that the auroral beads observed were most consistent with a shear-flow ballooning instability [*Voronkov et al.*, 1997], which is likely to obtain its energy from the transition region between dipolar and stretched magnetic field lines, however the Cross-Field Current Instability [e.g. *Lui*, 2004] for mid-tail plasma parameters could not be definitively ruled out.

Following the statistical affirmation that beads, prior to substorm onset, are instability driven, a statistical study was necessary to resolve how frequently beads are part of the substorm onset sequence. In Chapter 5, the prevalence of the formation of auroral beads along the substorm onset arc was investigated by using an independent substorm onset list, SOPHIE [*Forsyth et al.*, 2015] to identify substorms for study. The list included ~ 200 events with seemingly homogenous onset arcs, and onset arcs which exhibited clear beading. By using similar Fourier analysis techniques to study whether the auroral arcs had underlying azimuthal structuring, it was discovered that au-

roral beads are embedded within at least 90% of substorm onset arcs, with characteristic scales of $80 - 105$ km in the ionosphere. It is uncertain whether the remaining 10% of events did not have beads, or wether they were simply unresolvable. Statistically, it was found that a wide range of spatial scales also grow exponentially, again a characteristic signature of the linear stage of an instability. This is undeniable evidence that auroral beads are a common feature of the auroral substorm sequence, and hence that a plasma instability is an integral part of the substorm onset process. By demonstrating that auroral bead amplitudes are generally extremely low, it was shown that beads are often difficult to identify by eye, especially early on in the substorm process, hence why they have previously been thought of as a 'special case', rather than a common feature of the substorm.

In Chapters 4 & 5 the data analysed had no multi-spectral information, and hence it was impossible to infer the type of auroral acceleration processes operating during substorms. In Chapter 6, a case-study of a substorm onset arc observed by multi-spectral all-sky imagers was presented. It was initially shown that the auroral arc was only visible in the red-line aurora, which occurs due to the precipitation of low energy particles, and is a sign that the precipitating electrons were accelerated by a quasi-static potential drop. However in the minutes leading up to substorm onset the pre-existing arc also became visible in the blue and green-line aurora, as well as developing auroral beads. The observations of the onset arc in multiple auroral emission lines is consistent with broadband auroral acceleration, due to kinetic Alfvén waves [e.g. *Lotko*,1986]. This provides the first quantitative demonstration of the general consensus that the substorm onset arc is driven by kinetic Alfvén waves, after *Mende et al.* [2003] who observed wave-driven aurora $1 - 2$ minutes after substorm onset. This further confirms previous conclusions that the substorm onset arc, and auroral beads are driven by waves in the plasma sheet which go unstable. The results from this study suggest that the waves which cause auroral beads, and the waves which accelerate auroral electrons to high precipitation energies are linked.

In summary, in this thesis it has been shown through individual case

studies, and statistically that auroral beads are indicative of a plasma instability in the magnetosphere. When investigated using Fourier analysis, it was found that a wide range of bead spatial scales grow exponentially, but that certain spatial scales grow faster than others, suggesting that beads are most-likely driven by a Shear-Flow Ballooning Instability [*Voronkov et al.*, 1997]. Furthermore, we also show that beads are a common feature of the auroral substorm sequence. In at least 70% of events, auroral beads form and grow prior to the large scale increase in auroral intensity associated with the substorm expansion phase, showing that a plasma instability is a fundamental to the substorm onset process. Finally, we us a single case-study captured by unprecedented auroral imagery to observe auroral beads in multiple auroral emission lines, showing that electrons with a wide range of energies are causing this signature. Detailed analysis of the aurora have allowed us to improve our understand the processes and plasma properties in the minutes surrounding substorm onset, irrefutably confirming that the substorm instability is fundamental to the onset process. This places severe constraints on the instability, enabling future in-situ observations of auroral beads and associated processes in the magnetotail.

7.2 Future Work

In this thesis new analysis techniques for auroral data have been developed to remote-sense the magnetotail, allowing us to improve our understanding of the intricate processes at play in the near-Earth magnetosphere during substorms. The results show unequivocal evidence that auroral beads are instability-driven auroral signatures. By studying auroral beads in depth, it has been determined that beads are ubiquitous to all substorm onset arcs and hence that instabilities are a vital component of substorm onset. However in-situ observations are required in order to definitively solve the substorm mystery.

In order to definitively determine whether all auroral beads are consistent with a magnetospheric instability, and whether the same instability is driving

the beads, the temporal evolution of the large database of events presented in Chapter 5 needs to be investigated further. Constructing an observational dispersion relation of auroral beads will allow the determination whether large and small amplitude beads are driven by the same processes. By using conjugate in-situ spacecraft data, the extent of tail stretching and typical magnetospheric parameters can be determined. In Chapter 6, applying the spatial analysis techniques developed in this thesis to the ratios of the auroral data, will allow the determination whether specific spatial scales observed along the substorm onset arc are driven by different auroral acceleration processes.

With regard to the substorm instability, observation and statistics of the state of the magnetotail prior and during a substorm are necessary to pin-point the instability responsible. By characterising plasma sheet parameters such as thermal energy, temperature anisotropies, electron and ion energies, magnetic energy and flow energy (all of which can allow instabilities to grow) will allow us to establish the free energy source enabling the initiation of the instability. This will allow the determination of the prominent substorm model: whether the substorm is initiated in the tail through reconnection and earthward plasma flows, or locally in the near-Earth plasma sheet (or both). This will improve the understanding of the transfer of energy within the magnetotail and plasma sheet and is vital for identifying the type of instability (or instabilities) active during substorm onset. Direct observations of the waves excited in the minutes prior to substorm onset will also provide a measurement of the region of the magnetotail which is unstable to the instability without relying on equilibrium magnetic field mapping assumptions which are unlikely to be inaccurate during active substorm times. The satellites from the THEMIS mission are well-positioned for such a study, as well as magnetotail data from the MMS mission which will allow smaller scales to be investigated due to the closer positioning of the satellites.

Secondly, I would like to improve understanding magnetosphere-ionosphere coupling and auroral acceleration processes active during a substorms which project beads into the ionosphere, and uncover the magnetospheric source of auroral arcs. A statistical study of Cluster observations

in the auroral acceleration region, linked with the plasma sheet processes will unravel how the released energy is converted into auroral precipitation. A statistical study of this region, will demonstrate the differences between quiet, pre-substorm, and post-substorm times, the regions where wave-particle interactions occur, as well as comparing wave-acceleration of electrons with quasi-static potential drop acceleration. These observations will allow us to link the auroral processes with energy conversion in the plasma sheet. The type of waves observed will provide a global picture of how the near-Earth magnetosphere reacts to instability initiation in the plasma sheet and how this affects auroral electron precipitation.

Finally detailed conjugate studies of the auroral substorm onset arc, together with THEMIS/ MMS observations of the plasma sheet and magnetotail, as well as Cluster at perigee in the auroral acceleration region will provide the link between the separate regions of the magnetosphere during a substorm. This will provide a large-scale picture of the wave and energy propagation from the plasma sheet to the auroral acceleration region and answer how auroral beads are generated.

Bibliography

Akasofu, S.-I. (1964), The development of the auroral substorm, *Planetary and Space Science*, *12*(4), 273 – 282, doi:http://dx.doi.org/10.1016/0032-0633(64)90151-5.

Akasofu, S.-I. (1977), Physics of magnetospheric substorms, *Astrophysics and Space Science Library*, *47*.

Angelopoulos, V. (2008), The themis mission, *Space Science Reviews*, *141*(1-4), 5–34, doi:10.1007/s11214-008-9336-1.

Angelopoulos, V., W. Baumjohann, C. F. Kennel, F. V. Coroniti, M. G. Kivelson, R. Pellat, R. J. Walker, H. Lhr, and G. Paschmann (1992), Bursty bulk flows in the inner central plasma sheet, *Journal of Geophysical Research: Space Physics*, *97*(A4), 4027–4039, doi:10.1029/91JA02701, bursty BUlk FLows.

Angelopoulos, V., C. F. Kennel, F. V. Coroniti, W. C. Feldman, J. T. Gosling, M. G. Kivelson, R. J. Walker, and C. T. Russell (1993), Observations of a quasi-static plasma sheet boundary, *Geophysical Research Letters*, *20*(24), 2813–2816, doi:10.1029/93GL01979.

Angelopoulos, V., J. P. McFadden, D. Larson, C. W. Carlson, S. B. Mende, H. Frey, T. Phan, D. G. Sibeck, K.-H. Glassmeier, U. Auster, E. Donovan, I. R. Mann, I. J. Rae, C. T. Russell, A. Runov, X.-Z. Zhou, and L. Kepko (2008), Tail reconnection triggering substorm onset, *Science*, *321*(5891), 931–935, doi:10.1126/science.1160495.

Angelopoulos, V., J. P. McFadden, D. Larson, C. W. Carlson, S. B. Mende, H. Frey, T. Phan, D. G. Sibeck, K.-H. Glassmeier, U. Auster, E. Donovan,

I. R. Mann, I. J. Rae, C. T. Russell, A. Runov, X.-Z. Zhou, and L. Kepko (2009), Response to comment on "tail reconnection triggering substorm onset", *Science*, *324*(5933), 1391, doi:10.1126/science.1168045.

Anger, C. D., S. K. Babey, A. L. Broadfoot, R. G. Brown, L. L. Cogger, R. Gattinger, J. W. Haslett, R. A. King, D. J. McEwen, J. S. Murphree, E. H. Richardson, B. R. Sandel, K. Smith, and A. V. Jones (1987), An ultraviolet auroral imager for the viking spacecraft, *Geophysical Research Letters*, *14*(4), 387–390, doi:10.1029/GL014i004p00387.

Aubry, M. P., and R. L. McPherron (1971), Magnetotail changes in relation to the solar wind magnetic field and magnetospheric substorms, *Journal of Geophysical Research*, *76*(19), 4381–4401, doi:10.1029/JA076i019p04381.

Axford, W. I. (1969), Magnetospheric convection, *Reviews of Geophysics*, *7*(1-2), 421–459, doi:10.1029/RG007i001p00421.

Baker, D. N., T. I. Pulkkinen, V. Angelopoulos, W. Baumjohann, and R. L. McPherron (1996), Neutral line model of substorms: Past results and present view, *J. Geophys. Res.,* , *101*, 12,975–13,010, doi:10.1029/95JA03753.

Banks, P. M., C. R. Chappell, and A. F. Nagy (1974), A new model for the interaction of auroral electrons with the atmosphere: Spectral degradation, backscatter, optical emission, and ionization, *Journal of Geophysical Research*, *79*(10), 1459–1470, doi:10.1029/JA079i010p01459.

Baumjohann, W., and R. A. Treumann (1996), *Basic space plasma physics*, first ed., Imperial College Press, doi:10.1142/p015.

Baumjohann, W., G. Paschmann, and H. Lhr (1990), Characteristics of high-speed ion flows in the plasma sheet, *Journal of Geophysical Research: Space Physics*, *95*(A4), 3801–3809, doi:10.1029/JA095iA04p03801.

Blanchard, G. T., L. R. Lyons, J. C. Samson, and F. J. Rich (1995), Locating the polar cap boundary from observations of 6300 Å auroral emission, *Journal of Geophysical Research*, *100*(A5), 7855, doi:10.1029/94JA02631.

Burch, J. (2000), Image mission overview, *Space Science Reviews*, *91*(1), 1–14, doi:10.1023/A:1005245323115.

Carlson, C. W. (1992), The fast auroral snapshot explorer, *Eos, Transactions American Geophysical Union*, *73*(23), 249–256, doi:10.1029/91EO00202.

Chapman, S., and V. C. A. Ferraro (1931), A new theory of magnetic storms, *Terrestrial Magnetism and Atmospheric Electricity (Journal of Geophysical Research)*, *36*, 77, doi:10.1029/TE036i002p00077.

Chaston, C. C., J. W. Bonnell, C. W. Carlson, J. P. McFadden, R. E. Ergun, and R. J. Strangeway (2003), Properties of small-scale alfvn waves and accelerated electrons from fast, *Journal of Geophysical Research: Space Physics*, *108*(A4), n/a–n/a, doi:10.1029/2002JA009420, 8003.

Cheng, C. Z. (2004), Physics of substorm growth phase, onset, and dipolarization, *Space Sci. Rev.*, *113*, 207–270, doi:10.1023/B:SPAC.0000042943.59976.0e.

Cheng, C. Z., and A. T. Y. Lui (1998), Kinetic ballooning instability for substorm onset and current disruption observed by AMpte/cce, *Geophys. Res. Lett.*, *25*(21), 4091???4094, doi:10.1029/1998gl900093.

Cheng, C. Z., and S. Zaharia (2004), Mhd ballooning instability in the plasma sheet, *Geophysical Research Letters*, *31*(6), n/a–n/a, doi:10.1029/2003GL018823, l06809.

Cooley, J. W., and J. W. Tukey (1965), An algorithm for the machine calculation of complex Fourier series, *Mathematics of Computation*, *19*, 297–301.

Coppi, B., G. Laval, and R. Pellat (1966), Dynamics of the geomagnetic tail, *Physical Review Letters*, *16*, 1207–1210, doi:10.1103/PhysRevLett.16.1207.

Cowley, S. C., and M. Artun (1997), Explosive instabilities and detonation in magnetohydrodynamics, *Physics Reports*, *283*, 185 – 211, doi:http://dx.doi.org/10.1016/S0370-1573(96)00060-9, turbulence and Intermittency in Plasmas.

Cowley, S. W. H. (2000), *Magnetosphere-Ionosphere Interactions: A Tutorial Review*, pp. 91–106, American Geophysical Union, doi:10.1029/GM118p0091.

Cowley, S. W. H., and M. Lockwood (1992), Excitation and decay of solar wind-driven flows in the magnetosphere-ionosphere system, *Annales Geophysicae*, *10*, 103–115.

Crocker, J. C., and D. G. Grier (1996), Methods of digital video microscopy for colloidal studies, *Journal of Colloid and Interface Science*, *179*(1), 298 – 310, doi:10.1006/jcis.1996.0217.

Dalgarno, A., I. Latimer, and J. McConkey (1965), Corpuscular bombardment and n2+ radiation, *Planetary and Space Science*, *13*(10), 1008 – 1009, doi:http://dx.doi.org/10.1016/0032-0633(65)90160-1.

Dassoulas, J., D. L. Margolies, and M. R. Peterson (1985), The ampte cce spacecraft, *IEEE Transactions on Geoscience and Remote Sensing*, *GE-23*(3), 182–191, doi:10.1109/TGRS.1985.289512.

Davis, T. N. (1962), The morphology of the auroral displays of 1957-1958: 2. Detail analyses of Alaska data and analyses of high-latitude data, *Journal of Geophysical Research*, *67*(1), 75–110, doi:10.1029/JZ067i001p00075.

Davis, T. N. (1978), Observed characteristics of auroral forms, *Space Science Reviews*, *22*(1), 77–113, doi:10.1007/BF00215814.

Davis, T. N., and M. Sugiura (1966), Auroral electrojet activity index ae and its universal time variations, *Journal of Geophysical Research*, *71*(3), 785–801, doi:10.1029/JZ071i003p00785.

Deehr, C., and D. Lummerzheim (2001), Ground-based optical observations of hydrogen emission in the auroral substorm, *Journal of Geophysical Research*, *106*(A1), 33, doi:10.1029/2000ja002010.

Denton, M. H., J. E. Borovsky, M. Stepanova, and J. A. Valdivia (2016), Preface: Unsolved problems of magnetospheric physics, *Journal of Geo-*

physical Research: Space Physics, pp. n/a–n/a, doi:10.1002/2016JA023362, 2016JA023362.

Donovan, E., S. Mende, B. Jackel, M. Syrjasuo, M. Meurant, I. Voronkov, H. U. Frey, V. Angelopoulos, and C. M. (2006), The azimuthal evolution of the substorm expansive phase onset aurora, *ICS-8*, pp. 55–60.

Donovan, E., S. Mende, B. Jackel, H. Frey, M. Syrjsuo, I. Voronkov, T. Trondsen, L. Peticolas, V. Angelopoulos, S. Harris, M. Greffen, and M. Connors (2006), The {THEMIS} all-sky imaging array system design and initial results from the prototype imager, *Journal of Atmospheric and Solar-Terrestrial Physics*, *68*(13), 1472 – 1487, doi:http://dx.doi.org/10.1016/j.jastp.2005.03.027, passive Optics AeronomyPassive Optics Workshop.

Dungey, J. W. (1961), Interplanetary magnetic field and the auroral zones, *Physical Review Letters*, *6*, 47–48, doi:10.1103/PhysRevLett.6.47.

Elphinstone, R. D., D. J. Hearn, L. L. Cogger, J. S. Murphree, H. Singer, V. Sergeev, K. Mursula, D. M. Klumpar, G. D. Reeves, M. Johnson, and et al. (1995), Observations in the vicinity of substorm onset: Implications for the substorm process, *Journal of Geophysical Research*, *100*(A5), 7937, doi:10.1029/94ja02938.

Ergun, R. E., C. W. Carlson, J. P. McFadden, F. S. Mozer, G. T. Delory, W. Peria, C. C. Chaston, M. Temerin, R. Elphic, R. Strangeway, R. Pfaff, C. A. Cattell, D. Klumpar, E. Shelley, W. Peterson, E. Moebius, and L. Kistler (1998), Fast satellite observations of electric field structures in the auroral zone, *Geophysical Research Letters*, *25*(12), 2025–2028, doi:10.1029/98GL00635.

Fairfield, D. H., and N. F. Ness (1970), Configuration of the geomagnetic tail during substorms, *Journal of Geophysical Research*, *75*(34), 7032–7047, doi:10.1029/JA075i034p07032.

Fennell, J. F., S. G. Claudepierre, J. B. Blake, T. P. O'Brien, J. H. Clemmons, D. N. Baker, H. E. Spence, and G. D. Reeves (2015), Van allen

probes show that the inner radiation zone contains no mev electrons: Ect/mageis data, *Geophysical Research Letters*, *42*(5), 1283–1289, doi: 10.1002/2014GL062874, 2014GL062874.

Forsyth, C., C. E. J. Watt, I. J. Rae, A. N. Fazakerley, N. M. E. Kalmoni, M. P. Freeman, P. D. Boakes, R. Nakamura, I. Dandouras, L. M. Kistler, C. M. Jackman, J. C. Coxon, and C. M. Carr (2014), Increases in plasma sheet temperature with solar wind driving during substorm growth phases, *Geophysical Research Letters*, p. 0, doi:10.1002/2014GL062400.

Forsyth, C., I. J. Rae, J. C. Coxon, M. P. Freeman, C. M. Jackman, J. Gjerloev, and A. N. Fazakerley (2015), A new technique for determining Substorm Onsets and Phases from Indices of the Electrojet (SOPHIE), *Journal of Geophysical Research: Space Physics*, *120*(12), 10,592–10,606, doi:10.1002/2015JA021343.

Frey, H. U., S. B. Mende, V. Angelopoulos, and E. F. Donovan (2004), Substorm onset observations by IMAGE-FUV, *Journal of Geophysical Research*, *109*(A10), A10,304, doi:10.1029/2004JA010607.

Friedrich, E., J. C. Samson, and I. Voronkov (2001), Ground-based observations and plasma instabilities in auroral substorms, *Physics of Plasmas (1994-present)*, *8*(4), 1104–1110, doi:http://dx.doi.org/10.1063/1.1355678, wave-like formations observed in aurora during substorm onset.

Gillies, D. M., D. J. Knudsen, E. F. Donovan, E. L. Spanswick, C. Hansen, D. Keating, and S. Erion (2014), A survey of quiet auroral arc orientation and the effects of the interplanetary magnetic field, *Journal of Geophysical Research: Space Physics*, *119*(4), 25502562, doi:10.1002/2013ja019469.

Gjerloev, J. W. (2009), A global ground-based magnetometer initiative, *Eos, Transactions American Geophysical Union*, *90*(27), 230–231, doi:10.1029/2009EO270002.

Gjerloev, J. W. (2012), The SuperMAG data processing technique, *Journal of Geophysical Research: Space Physics*, *117*(A9), n/a–n/a, doi:10.1029/2012JA017683.

Grubbs, G. (2016), Magnetosphere-ionosphere coupling during active aurora, Ph.D. thesis, University of Texas at San Antonio.

Grubbs, G., R. Michell, M. Samara, D. Hampton, and J.-M. Jahn (2016), A synthesis of star calibration techniques for ground-based narrowband electron-multiplying charge-coupled device imagers used in auroral photometry, *Journal of Geophysical Research: Space Physics*, *121*(6), 5991–6002, doi:10.1002/2015JA022186, 2015JA022186.

Hallinan, T. J., and T. Davis (1970), Small-scale auroral arc distortions, *Planetary and Space Science*, *18*(12), 1735 – 1744, doi:http://dx.doi.org/10.1016/0032-0633(70)90007-3.

Hameiri, E., P. Laurence, and M. Mond (1991), The ballooning instability in space plasmas, *Journal of Geophysical Research: Space Physics*, *96*(A2), 1513–1526, doi:10.1029/90JA02100.

Henderson, M. G. (1994), Implications of viking imager results for substorm models, Ph.D. thesis, University of Calgary.

Henderson, M. G. (2009), Observational evidence for an inside-out substorm onset scenario, *Annales Geophysicae*, *27*(5), 2129–2140, doi:10.5194/angeo-27-2129-2009.

Heppner, J. P. (1954), Time sequences and spatial relations in auroral activity during magnetic bays at college, alaska, *Journal of Geophysical Research*, *59*(3), 329–338, doi:10.1029/JZ059i003p00329.

Heppner, J. P. (1958), A study of the relationships between the aurora borealis and the geomagnetic disturbances caused by electric currents in the ionosphere, Ph.D. thesis, California Institute of Technology.

Hirsch, M., R. J. Wareham, M. L. Martin-Fernandez, M. P. Hobson, and D. J. Rolfe (2013), A Stochastic Model for Electron Multiplication Charge-Coupled Devices - From Theory to Practice, *PLoS ONE*, *8*, e53,671, doi:10.1371/journal.pone.0053671.

Hones, E. W., S.-I. Akasofu, S. J. Bame, and S. Singer (1971), Poleward expansion of the auroral oval and associated phenomena in the magnetotail during auroral substorms, 2, *Journal of Geophysical Research*, *76*(34), 8241–8257, doi:10.1029/JA076i034p08241.

Hones, E. W., T. A. Fritz, J. Birn, J. Cooney, and S. J. Bame (1986a), Detailed observations of the plasma sheet during a substorm on april 24, 1979, *Journal of Geophysical Research: Space Physics*, *91*(A6), 6845–6859, doi:10.1029/JA091iA06p06845.

Hones, E. W., T. A. Fritz, J. Birn, J. Cooney, and S. J. Bame (1986b), Detailed observations of the plasma sheet during a substorm on april 24, 1979, *Journal of Geophysical Research: Space Physics*, *91*(A6), 6845–6859, doi:10.1029/JA091iA06p06845.

Hones, J., E. W. (1976), Observations in the earth's magnetotail relating to magnetic merging, *Solar Physics*, *47*(1), 101–113, doi:10.1007/BF00152248.

Hosokawa, K., S. E. Milan, M. Lester, A. Kadokura, N. Sato, and G. Bjornsson (2013), Large flow shears around auroral beads at substorm onset, *Geophysical Research Letters*, *40*(19), 4987–4991, doi:10.1002/grl.50958.

Jacobs, J. A., and K. Sinno (1960), World-Wide Characteristics of Geomagnetic Micropulsations, *Geophysical Journal*, *3*, 333–353, doi:10.1111/j.1365-246X.1960.tb01707.x.

Jacobs, J. A., Y. Kato, S. Matsushita, and V. A. Troitskaya (1964), Classification of geomagnetic micropulsations, *Journal of Geophysical Research*, *69*(1), 180–181, doi:10.1029/JZ069i001p00180.

Jiang, F., R. J. Strangeway, M. G. Kivelson, J. M. Weygand, R. J. Walker, K. K. Khurana, Y. Nishimura, V. Angelopoulos, and E. Donovan (2012), In situ observations of the preexisting auroral arc by THEMIS all sky imagers and the FAST spacecraft, *Journal of Geophysical Research*, *117*(A5), A05,211, doi:10.1029/2011JA017128.

Johnstone, A. D., and J. D. Winningham (1982), Satellite observations of suprathermal electron bursts, *Journal of Geophysical Research: Space Physics*, *87*(A4), 2321–2329, doi:10.1029/JA087iA04p02321.

Kaeppler, S. R., D. L. Hampton, M. J. Nicolls, A. Strmme, S. C. Solomon, J. H. Hecht, and M. G. Conde (2015), An investigation comparing ground-based techniques that quantify auroral electron flux and conductance, *Journal of Geophysical Research: Space Physics*, *120*(10), 9038–9056, doi:10.1002/2015JA021396, 2015JA021396.

Kalmoni, N., I. Rae, C. Watt, K. Murphy, C. Forsyth, and C. Owen (2015), Statistical characterization of the growth and spatial scales of the substorm onset arc, *Journal of Geophysical Research A: Space Physics*, *120*(10), doi:10.1002/2015JA021470.

Kasten, F. (1965), A new table and approximation formula for the relative optial air mass, *Archiv für Meteorologie, Geophysik und Bioklimatologie, Serie B*, *14*(2), 206–223.

Keiling, A. (2008), Alfven waves and their roles in the dynamics of the earth's magnetotail: A review, *Space Science Review*, *142*.

Kepko, L., E. Spanswick, V. Angelopoulos, E. Donovan, J. McFadden, K. H. Glassmeier, J. Raeder, and H. J. Singer (2009), Equatorward moving auroral signatures of a flow burst observed prior to auroral onset, *Geophysical Research Letters*, *36*(24), doi:10.1029/2009GL041476.

Kivelson, M. G., and C. T. Russell (1995), *Introduction to Space Physics*, first ed., Cambridge University Press.

Lanchester, B. S., M. H. Rees, D. Lummerzheim, A. Otto, H. U. Frey, and K. U. Kaila (1997), Large fluxes of auroral electrons in filaments of 100 m width, *Journal of Geophysical Research: Space Physics*, *102*(A5), 9741–9748, doi:10.1029/97JA00231.

Lee, L. C., L. Zhang, A. Otto, G. S. Choe, and H. J. Cai (1998), Entropy antidiffusion instability and formation of a thin current sheet during geomag-

netic substorms, *Journal of Geophysical Research: Space Physics*, *103*(A12), 29,419–29,428, doi:10.1029/97JA02141.

Lester, M., W. J. Hughes, and H. J. Singer (1983), Polarization patterns of Pi 2 magnetic pulsations and the substorm current wedge, *J. Geophys. Res.,* , *88*, 7958–7966, doi:10.1029/JA088iA10p07958.

Li, X., R. S. Selesnick, D. N. Baker, A. N. Jaynes, S. G. Kanekal, Q. Schiller, L. Blum, J. Fennell, and J. B. Blake (2015), Upper limit on the inner radiation belt mev electron intensity, *Journal of Geophysical Research: Space Physics*, *120*(2), 1215–1228, doi:10.1002/2014JA020777, 2014JA020777.

Liang, J., E. F. Donovan, W. W. Liu, B. Jackel, M. Syrjäsuo, S. B. Mende, H. U. Frey, V. Angelopoulos, and M. Connors (2008), Intensification of preexisting auroral arc at substorm expansion phase onset: Wave-like disruption during the first tens of seconds, *Geophys. Res. Lett.,* , *35*, L17S19, doi:10.1029/2008GL033666.

Liu, W. W. (1997), Physics of the explosive growth phase: Ballooning instability revisited, *Journal of Geophysical Research: Space Physics*, *102*(A3), 4927–4931, doi:10.1029/96JA03561.

Lotko, W. (1986), Diffusive acceleration of auroral primaries, *Journal of Geophysical Research: Space Physics*, *91*(A1), 191–203, doi:10.1029/JA091iA01p00191.

Lui, A. (2004), Potential plasma instabilities for substorm expansion onsets, *Space Science Reviews*, *113*(1-2), 127–206, doi:10.1023/B:SPAC.0000042942.00362.4e.

Lui, A. T. Y. (1991), A synthesis of magnetospheric substorm models, *Journal of Geophysical Research: Space Physics*, *96*(A2), 1849–1856, doi:10.1029/90JA02430.

Lui, A. T. Y. (1996), Current disruption in the earth's magnetosphere: Observations and models, *Journal of Geophysical Research: Space Physics*, *101*(A6), 13,067–13,088, doi:10.1029/96JA00079.

Lui, A. T. Y. (2009), Comment on 'tail reconnection triggering substorm onset', *Science*, *324*, 1391–, doi:10.1126/science.1167726.

Lui, A. T. Y. (2016), Cross-field current instability for auroral bead formation in breakup arcs, *Geophys. Res. Lett.,* , *43*, 6087–6095, doi:10.1002/2016GL069892.

Lui, A. T. Y., C.-L. Chang, A. Mankofsky, H.-K. Wong, and D. Winske (1991), A cross-field current instability for substorm expansions, *J. Geophys. Res.,* , *96*, 11,389, doi:10.1029/91JA00892.

Lui, A. T. Y., R. E. Lopez, B. J. Anderson, K. Takahashi, L. J. Zanetti, R. W. McEntire, T. A. Potemra, D. M. Klumpar, E. M. Greene, and R. Strangeway (1992), Current disruptions in the near-earth neutral sheet region, *J. Geophys. Res.,* , *97*, 1461–1480, doi:10.1029/91JA02401.

Lui, A. T. Y., P. H. Yoon, and C.-L. Chang (1993), Quasi-linear analysis of ion weibel instability in the earth's neutral sheet, *J. Geophys. Res.,* , *98*, 153–163, doi:10.1029/92JA02034.

Lynch, K. A., D. Hampton, M. Mella, B. Zhang, H. Dahlgren, M. Disbrow, P. M. Kintner, M. Lessard, E. Lundberg, and H. C. Stenbaek-Nielsen (2012), Structure and dynamics of the nightside poleward boundary: Sounding rocket and ground-based observations of auroral electron precipitation in a rayed curtain, *Journal of Geophysical Research: Space Physics*, *117*(A11), n/a–n/a, doi:10.1029/2012JA017691, a11202.

Mann, H. B., and D. R. Whitney (1947), On a test of whether one of two random variables is stochastically larger than the other, *Ann. Math. Statist.*, *18*(1), 50–60, doi:10.1214/aoms/1177730491.

Mann, I., D. Milling, I. Rae, L. Ozeke, A. Kale, Z. Kale, K. Murphy, A. Parent, M. Usanova, D. Pahud, E.-A. Lee, V. Amalraj, D. Wallis, V. Angelopoulos, K.-H. Glassmeier, C. Russell, H.-U. Auster, and H. Singer (2008), The upgraded carisma magnetometer array in thethemis era, *Space Science Reviews*, *141*(1-4), 413–451, doi:10.1007/s11214-008-9457-6.

Maynard, N. C., W. J. Burke, E. M. Basinska, G. M. Erickson, W. J. Hughes, H. J. Singer, A. G. Yahnin, D. A. Hardy, and F. S. Mozer (1996), Dynamics of the inner magnetosphere near times of substorm onsets, *Journal of Geophysical Research*, *101*(A4), 7705, doi:10.1029/95ja03856.

McPherron, R. (1972), Substorm related changes in the geomagnetic tail: the growth phase, *Planetary and Space Science*, *20*(9), 1521 – 1539, doi:http://dx.doi.org/10.1016/0032-0633(72)90054-2.

McPherron, R. L. (1970), Growth phase of magnetospheric substorms., *J. Geophys. Res.,* , *75*, 5592–5599, doi:10.1029/JA075i028p05592.

McPherron, R. L., C. T. Russell, and M. P. Aubry (1973), Satellite studies of magnetospheric substorms on august 15, 1968: 9. phenomenological model for substorms, *J. Geophys. Res.,* , *78*, 3131, doi:10.1029/JA078i016p03131.

Meier, R. R., D. J. Strickland, J. H. Hecht, and A. B. Christensen (1989), Deducing composition and incident electron spectra from ground-based auroral optical measurements: A study of auroral red line processes, *Journal of Geophysical Research: Space Physics*, *94*(A10), 13,541–13,552, doi:10.1029/JA094iA10p13541.

Mende, S., S. Harris, H. Frey, V. Angelopoulos, C. Russell, E. Donovan, B. Jackel, M. Greffen, and L. Peticolas (2008), The themis array of ground-based observatories forthe study of auroral substorms, *Space Science Reviews*, *141*(1-4), 357–387, doi:10.1007/s11214-008-9380-x.

Mende, S. B., H. Heetderks, H. U. Frey, M. Lampton, S. P. Geller, R. Abiad, O. H. W. Siegmund, A. S. Tremsin, J. Spann, H. Dougani, S. A. Fuselier, A. L. Magoncelli, M. B. Bumala, S. Murphree, and T. Trondsen (2000), Far ultraviolet imaging from the IMAGE spacecraft. 2. Wideband FUV imaging, *Space Science Reviews*, *91*(1), 271–285, doi:10.1023/A:1005227915363.

Mende, S. B., C. W. Carlson, H. U. Frey, L. M. Peticolas, and N. Østgaard (2003), FAST and IMAGE-FUV observations of a substorm onset, *Journal of Geophysical Research (Space Physics)*, *108*, 1344, doi:10.1029/2002JA009787.

Mende, S. B., H. U. Frey, V. Angelopoulos, and Y. Nishimura (2011), Substorm triggering by poleward boundary intensification and related equatorward propagation, *Journal of Geophysical Research: Space Physics*, *116*(A5), n/a–n/a, doi:10.1029/2010JA015733, a00I31.

Michell, R. G., M. G. McHarg, M. Samara, and D. L. Hampton (2012), Spectral analysis of flickering aurora, *Journal of Geophysical Research: Space Physics*, *117*(A3), n/a–n/a, doi:10.1029/2011JA016703, a03321.

Milan, S. E., M. Lester, S. W. H. Cowley, K. Oksavik, M. Brittnacher, R. A. Greenwald, G. Sofko, and J.-P. Villain (2003), Variations in the polar cap area during two substorm cycles, *Annales Geophysicae*, *21*(3), 1121–1140, doi:10.5194/angeo-21-1121-2003, paper 3.

Milan, S. E., J. S. Gosling, and B. Hubert (2012), Relationship between interplanetary parameters and the magnetopause reconnection rate quantified from observations of the expanding polar cap, *Journal of Geophysical Research: Space Physics*, *117*(A3), n/a–n/a, doi:10.1029/2011JA017082, a03226.

Milling, D. K., I. J. Rae, I. R. Mann, K. R. Murphy, A. Kale, C. T. Russell, V. Angelopoulos, and S. Mende (2008), Ionospheric localisation and expansion of long-period pi1 pulsations at substorm onset, *Geophys. Res. Lett.,* , *35*, L17S20, doi:10.1029/2008GL033672.

Motoba, T., K. Hosokawa, A. Kadokura, and N. Sato (2012), Magnetic conjugacy of northern and southern auroral beads, *Geophys. Res. Lett.,* , *39*, L08108, doi:10.1029/2012GL051599.

Murphy, K. R., I. J. Rae, I. R. Mann, D. K. Milling, C. E. J. Watt, L. Ozeke, H. U. Frey, V. Angelopoulos, and C. T. Russell (2009), Wavelet-based ulf wave diagnosis of substorm expansion phase onset, *Journal of Geophysical Research (Space Physics)*, *114*, A00C16, doi:10.1029/2008JA013548.

Murphy, K. R., I. R. Mann, I. J. Rae, C. L. Waters, B. J. Anderson, D. K. Milling, H. J. Singer, and H. Korth (2012), Reduction in field-aligned cur-

rents preceding and local to auroral substorm onset, *Geophysical Research Letters*, *39*(15), doi:10.1029/2012GL052798.

Murphy, K. R., D. M. Miles, C. E. J. Watt, I. J. Rae, I. R. Mann, and H. U. Frey (2014), Automated determination of auroral breakup during the substorm expansion phase using all-sky imager data, *Journal of Geophysical Research: Space Physics*, *119*(2), 1414–1427, doi:10.1002/2013JA018773.

Nagy, A. F., and P. M. Banks (1970), Photoelectron fluxes in the ionosphere, *Journal of Geophysical Research*, *75*(31), 6260–6270, doi:10.1029/JA075i031p06260.

Newell, P. T., and J. W. Gjerloev (2011), Evaluation of SuperMAG auroral electrojet indices as indicators of substorms and auroral power, *Journal of Geophysical Research: Space Physics*, *116*(A12), n/a–n/a, doi:10.1029/2011JA016779.

Newell, P. T., T. Sotirelis, and S. Wing (2009), Diffuse, monoenergetic, and broadband aurora: The global precipitation budget, *Journal of Geophysical Research: Space Physics*, *114*(A9), n/a–n/a, doi:10.1029/2009JA014326, a09207.

Newell, P. T., A. R. Lee, K. Liou, S.-I. Ohtani, T. Sotirelis, and S. Wing (2010), Substorm cycle dependence of various types of aurora, *Journal of Geophysical Research: Space Physics*, *115*(A9), n/a–n/a, doi:10.1029/2010JA015331, a09226.

Nishimura, Y., L. Lyons, S. Zou, V. Angelopoulos, and S. Mende (2010), Substorm triggering by new plasma intrusion: Themis all-sky imager observations, *J. Geophys. Res.*, *115*(A7), A07,222–.

Ohtani, S., K. Takahashi, L. J. Zanetti, T. A. Potemra, R. W. McEntire, and T. Iijima (1992), Initial signatures of magnetic field and energetic particle fluxes at tail reconfiguration - explosive growth phase, *J. Geophys. Res.,* , *97*, 19,311, doi:10.1029/92JA01832.

Ohtani, S.-I. (2004), Flow bursts in the plasma sheet and auroral substorm onset: Observational constraints on connection between midtail and near-earth substorm processes, *Space Sci. Rev.*, *113*, 77–96, doi:10.1023/B:SPAC.0000042940.59358.2f.

Ohtani, S.-I., and T. Tamao (1993), Does the ballooning instability trigger substorms in the near-earth magnetotail?, *Journal of Geophysical Research: Space Physics*, *98*(A11), 19,369–19,379, doi:10.1029/93JA01746.

Olson, J. V., and G. Rostoker (1975), Pi 2 pulsations and the auroral electrojet, *Planet. Space Sci.*, *23*, 1129–1139, doi:10.1016/0032-0633(75)90163-4.

Østgaard, N., G. Germany, J. Stadsnes, and R. R. Vondrak (2002), Energy analysis of substorms based on remote sensing techniques, solar wind measurements, and geomagnetic indices, *Journal of Geophysical Research: Space Physics*, *107*(A9), SMP 9–1–SMP 9–14, doi:10.1029/2001JA002002, 1233.

Parker, E. N. (1958), Dynamics of the Interplanetary Gas and Magnetic Fields., *ApJ*, *128*, 664, doi:10.1086/146579.

Perraut, S., O. Le Contel, A. Roux, and A. Pedersen (2000), Current-driven electromagnetic ion cyclotron instability at substorm onset, *J. Geophys. Res.,* , *105*, 21,097, doi:10.1029/2000JA900059.

Press, S. A. William H Flannery, Brian Pand Teukolsky, and W. Vetterling (1992), Numerical recipes in c, *Press Syndicate of the University of Cambridge, New York*, *24*.

Pu, Z. Y., K. B. Kang, A. Korth, S. Y. Fu, Q. G. Zong, Z. X. Chen, M. H. Hong, Z. X. Liu, C. G. Mouikis, R. W. H. Friedel, and T. Pulkkinen (1999), Ballooning instability in the presence of a plasma flow: A synthesis of tail reconnection and current disruption models for the initiation of substorms, *Journal of Geophysical Research: Space Physics*, *104*(A5), 10,235–10,248, doi:10.1029/1998JA900104.

Pulkkinen, T. I., D. N. Baker, D. H. Fairfield, R. J. Pellinen, J. S. Murphree, R. D. Elphinstone, R. L. McPherron, J. F. Fennell, R. E. Lopez, and T. Na-

gai (1991), Modeling the growth phase of a substorm using the tsyganenko model and multi-spacecraft observations - cdaw-9, *Geophys. Res. Lett.,* , *18*, 1963–1966, doi:10.1029/91GL02002.

Rae, I. J., I. R. Mann, V. Angelopoulos, K. R. Murphy, D. K. Milling, A. Kale, H. U. Frey, G. Rostoker, C. T. Russell, C. E. J. Watt, M. J. Engebretson, M. B. Moldwin, S. B. Mende, H. J. Singer, and E. F. Donovan (2009a), Near-Earth initiation of a terrestrial substorm, *Journal of Geophysical Research: Space Physics*, *114*(A7), n/a–n/a, doi:10.1029/2008JA013771.

Rae, I. J., I. R. Mann, K. R. Murphy, D. K. Milling, A. Parent, V. Angelopoulos, H. U. Frey, A. Kale, C. E. J. Watt, S. B. Mende, and C. T. Russell (2009b), Timing and localization of ionospheric signatures associated with substorm expansion phase onset, *Journal of Geophysical Research: Space Physics*, *114*(A1), 0, doi:10.1029/2008JA013559.

Rae, I. J., C. E. J. Watt, I. R. Mann, K. R. Murphy, J. C. Samson, K. Kabin, and V. Angelopoulos (2010), Optical characterization of the growth and spatial structure of a substorm onset arc, *Journal of Geophysical Research*, *115*(2), 10,222.

Rae, I. J., K. R. Murphy, C. E. J. Watt, and I. R. Mann (2011), On the nature of ulf wave power during nightside auroral activations and substorms: 2. temporal evolution, *Journal of Geophysical Research: Space Physics*, *116*(A5), n/a–n/a, doi:10.1029/2010JA015762.

Rae, I. J., C. E. J. Watt, K. R. Murphy, H. U. Frey, L. G. Ozeke, D. K. Milling, and I. R. Mann (2012), The correlation of ulf waves and auroral intensity before, during and after substorm expansion phase onset, *Journal of Geophysical Research: Space Physics*, *117*(A8), n/a–n/a, doi:10.1029/2012JA017534.

Rae, I. J., K. R. Murphy, C. E. J. Watt, G. Rostoker, R. Rankin, I. R. Mann, C. R. Hodgson, H. U. Frey, A. W. Degeling, and C. Forsyth (2014), Field line resonances as a trigger and a tracer for substorm onset, *Journal of Geophysi-*

cal Research: Space Physics, *119*(7), 5343–5363, doi:10.1002/2013JA018889, 2013JA018889.

Rayleigh (1882), Investigation of the character of the equilibrium of an incompressible heavy fluid of variable density, *Proceedings of the London Mathematical Society*, *s1-14*(1), 170–177, doi:10.1112/plms/s1-14.1.170.

Rees, M. H. (1963), Auroral ionization and excitation by incident energetic electrons, *Planetary and Space Science*, *11*(10), 1209 – 1218, doi:http://dx.doi.org/10.1016/0032-0633(63)90252-6.

Rees, M. H., and D. Luckey (1974), Auroral electron energy derived from ratio of spectroscopic emissions 1. model computations, *Journal of Geophysical Research*, *79*(34), 5181–5186, doi:10.1029/JA079i034p05181.

Rees, M. H., G. J. Romick, H. R. Anderson, and R. T. Casserly, Jr. (1976), Calculation of auroral emissions from measured electron precipitation - Comparison with observation, *J. Geophys. Res.,* , *81*, 5091–5096, doi:10.1029/JA081i028p05091.

Rostoker, G., and T. Eastman (1987), A boundary layer model for magnetospheric substorms, *Journal of Geophysical Research*, *92*(A11), 12,187, doi:10.1029/ja092ia11p12187.

Rostoker, G., J. C. Samson, F. Creutzberg, T. J. Hughes, D. R. McDiarmid, A. G. McNamara, A. V. Jones, D. D. Wallis, and L. L. Cogger (1995), Canopus — a ground-based instrument array for remote sensing the high latitude ionosphere during the istp/ggs program, *Space Science Reviews*, *71*(1), 743–760, doi:10.1007/BF00751349.

Roux, A., S. Perraut, P. Robert, A. Morane, A. Pedersen, A. Korth, G. Kremser, B. Aparicio, D. Rodgers, and R. Pellinen (1991), Plasma sheet instability related to the westward traveling surge, *J. Geophys. Res.,* , *96*, 17,697, doi:10.1029/91JA01106.

Russell, C., P. Chi, D. Dearborn, Y. Ge, B. Kuo-Tiong, J. Means, D. Pierce,

K. Rowe, and R. Snare (2008), Themis ground-based magnetometers, *Space Science Reviews*, *141*(1-4), 389–412, doi:10.1007/s11214-008-9337-0.

Saito, M. H., Y. Miyashita, M. Fujimoto, I. Shinohara, Y. Saito, K. Liou, and T. Mukai (2008), Ballooning mode waves prior to substorm-associated dipolarizations: Geotail observations, *Geophys. Res. Lett.*, *35*(7), n/a???n/a, doi:10.1029/2008gl033269.

Saito, T. (1969), Geomagnetic pulsations, *Space Science Reviews*, *10*(3), 319–412, doi:10.1007/BF00203620.

Sakaguchi, K., K. Shiokawa, A. Ieda, R. Nomura, A. Nakajima, M. Greffen, E. Donovan, I. R. Mann, H. Kim, and M. Lessard (2009), Fine structures and dynamics in auroral initial brightening at substorm onsets, *Annales Geophysicae*, *27*(2), 623–630, doi:10.5194/angeo-27-623-2009.

Samara, M., R. G. Michell, and D. L. Hampton (2012), BG3 Glass Filter Effects on Quantifying Rapidly Pulsating Auroral Structures, *Advances in Remote Sensing*, *01*(03), 53–57, doi:10.4236/ars.2012.13005.

Samson, J. C., L. R. Lyons, P. T. Newell, F. Creutzberg, and B. Xu (1992a), Proton aurora and substorm intensifications, *Geophysical Research Letters*, *19*(21), 2167–2170, doi:10.1029/92GL02184.

Samson, J. C., B. G. Harrold, J. M. Ruohoniemi, R. A. Greenwald, and A. D. M. Walker (1992b), Field line resonances associated with mhd waveguides in the magnetosphere, *Geophysical Research Letters*, *19*(5), 441–444, doi:10.1029/92GL00116.

Samson, J. C., A. K. MacAulay, R. Rankin, P. Frycz, I. Vorinkov, and L. L. Cogger (1996), Substorm intensifications and resistive shear flow-ballooning instabilities in the near-earth magnetotail, in *International Conference on Substorms*, *ESA Special Publication*, vol. 389, edited by E. J. Rolfe and B. Kaldeich, p. 399.

Samson, J. C., R. Rankin, and V. T. Tikhonchuk (2003), Optical signatures of auroral arcs produced by field line resonances: comparison with satellite

observations and modeling, *Annales Geophysicae*, *21*(4), 933–945, doi:10.5194/angeo-21-933-2003.

Semeter, J., and E. M. Blixt (2006), Evidence for Alfvén wave dispersion identified in high-resolution auroral imagery, *Geophys. Res. Lett.,* , *33*, L13106, doi:10.1029/2006GL026274.

Sergeev, V. A., V. Angelopoulos, and R. Nakamura (2012), Recent advances in understanding substorm dynamics, *Geophys. Res. Lett.*, *39*(5), L05,101–.

Sergeev, V. A., D. A. Sormakov, and V. Angelopoulos (2014), A missing variable in solar wind-magnetosphere-ionosphere coupling studies, *Geophysical Research Letters*, *41*(23), 8215–8220, doi:10.1002/2014GL062271, 2014GL062271.

Shiokawa, K., K. Yumoto, Y. Tanaka, H. Osaki, M. Sato, T. Kato, Y. Kato, M. Sera, Y. Ikegami, S.-I. Akasofu, K. Hayashi, T. Oguti, and Y. Kiyama (1996), Auroral Observations Using Automatic Optical Instruments: Relations with Multiple Pi 2 Magnetic Pulsations, *Journal of geomagnetism and geoelectricity*, *48*(11), 1407–1419, doi:10.5636/jgg.48.1407.

Sibeck, D., and V. Angelopoulos (2008), Themis science objectives and mission phases, *Space Science Reviews*, *141*(1-4), 35–59, doi:10.1007/s11214-008-9393-5.

Solomon, S. C. (1989), Auroral excitation of the n2 2p(0,0) and vk(0,9) bands, *Journal of Geophysical Research: Space Physics*, *94*(A12), 17,215–17,222, doi:10.1029/JA094iA12p17215.

Solomon, S. C. (2001), Auroral particle transport using monte carlo and hybrid methods, *Journal of Geophysical Research: Space Physics*, *106*(A1), 107–116, doi:10.1029/2000JA002011.

Solomon, S. C., P. B. Hays, and V. J. Abreu (1988), The auroral 6300 emission: Observations and modeling, *Journal of Geophysical Research: Space Physics*, *93*(A9), 9867–9882, doi:10.1029/JA093iA09p09867.

Song, Y., and R. L. Lysak (2001), Towards a new paradigm: from a quasi-steady description to a dynamical description of the magnetosphere, *Space Sci. Rev.*, *95*, 273–292.

Strickland, D. J., R. E. Daniell, J. R. Jasperse, and B. Basu (1993), Transport-theoretic model for the electron-proton-hydrogen atom aurora: 2. model results, *Journal of Geophysical Research: Space Physics*, *98*(A12), 21,533–21,548, doi:10.1029/93JA01645.

Treumann, R. A., and W. Baumjohann (1997), *Advanced space plasma physics*, first ed., Imperial College Press.

Tsyganenko, N. (1989), A magnetospheric magnetic field model with a warped tail current sheet, *Planetary and Space Science*, *37*(1), 5 – 20, doi:http://dx.doi.org/10.1016/0032-0633(89)90066-4.

Tsyganenko, N. A. (1995), Modeling the earth's magnetospheric magnetic field confined within a realistic magnetopause, *Journal of Geophysical Research: Space Physics*, *100*(A4), 5599–5612, doi:10.1029/94JA03193.

Voronkov, I., R. Rankin, P. Frycz, V. T. Tikhonchuk, and J. C. Samson (1997), Coupling of shear flow and pressure gradient instabilities, *Journal of Geophysical Research*, *102*(A5), 9639, doi:10.1029/97ja00386.

Voronkov, I., E. F. Donovan, B. J. Jackel, and J. C. Samson (2000), Large-scale vortex dynamics in the evening and midnight auroral zone: Observations and simulations, *J. Geophys. Res.,* , *105*, 18,505–18,518, doi:10.1029/1999JA000442.

Walsh, A. P. (2009), New perspectives on magnetotail dynamic processes from combined cluster and double star observations, Ph.D. thesis, University College London.

Walsh, A. P., I. J. Rae, A. N. Fazakerley, K. R. Murphy, I. R. Mann, C. E. J. Watt, M. Volwerk, C. Forsyth, H. J. Singer, E. F. Donovan, and T. L. Zhang (2010), Comprehensive ground-based and in situ observations of substorm

expansion phase onset, *Journal of Geophysical Research: Space Physics*, *115*(A5), n/a–n/a, doi:10.1029/2010JA015748.

Walsh, A. P., A. N. Fazakerley, C. Forsyth, C. J. Owen, M. G. G. T. Taylor, and I. J. Rae (2013), Sources of electron pitch angle anisotropy in the magnetotail plasmasheet, *Journal of Geophysical Research: Space Physics*, *118*(10), 6042–6054, doi:10.1002/jgra.50553.

Whipple, F. L. (1966), *Smithsonian Astrophysical Observatory Star Catalog*, Washington: Smithsonian Institution Press.

Williams, D. J. (1980), *Ring Current Composition and Sources*, pp. 407–424, Springer Netherlands, Dordrecht, doi:10.1007/978-94-009-9519-2_21.

Yoon, P. H., A. T. Y. Lui, and C.-L. Chang (1994), Lower-hybrid-drift instability operative in the geomagnetic tail, *Physics of Plasmas*, *1*, 3033–3043, doi:10.1063/1.870496.

Yoon, P. H., J. F. Drake, and A. T. Y. Lui (1996), Theory and simulation of kelvin-helmholtz instability in the geomagnetic tail, *Journal of Geophysical Research: Space Physics*, *101*(A12), 27,327–27,339, doi:10.1029/96JA02752.

Zhu, P., A. Bhattacharjee, and Z. Ma (2004), Finite k y ballooning instability in the near-earth magnetotail, *Journal of Geophysical Research*, *109*(A11), doi:10.1029/2004ja010505.

Zhu, Z., and R. M. Winglee (1996), Tearing instability, flux ropes, and the kinetic current sheet kink instability in the earth's magnetotail: A three-dimensional perspective from particle simulations, *J. Geophys. Res.,* , *101*, 4885–4898, doi:10.1029/95JA03144.

Zombeck, M. V. (2006), *Handbook of Space Astronomy and Astrophysics*, Cambridge University Press.